DOCTOR OF PHILOSOPHY

Real time motion tracking in image guided focused ultrasound intervention

Xu Xiao

2014

University of Dundee

Real time motion tracking in image guided focused ultrasound intervention

by

Xu Xiao

A Thesis Submitted in Fulfilment of the Requirements of the University of Dundee for the Degree of Doctor of Philosophy (Ph.D.) in Mechanical Engineering

Jan 2014

Table of Contents

Declaration

I hereby declare that this thesis has been compiled by myself, that it is a record of work completed by myself and that it has not previously been accepted for a higher degree at this University or any other institution of learning. Where other sources of information have been used, they have been acknowledged.

_____

Xu Xiao

Certificate

This is to certify that Xu Xiao has done this research under my supervision and that he has fulfilled the conditions of Ordinance 39 of the University of Dundee, so that he is qualified to submit for the Degree of Doctor of Philosophy.

_____

Dr. Zhihong Huang

Copyright

List of Figures

List of Tables

List of Abbreviations

AP	anterior-posterior
BBB	Blood brain barrier
BNC	Bayonet-Neil-Concelman
CBS	conformal bone system
CCM	cross correlation map
CEM	Cumulative equivalent minutes
CI	confidence interval
CT	computed tomography
DOF	degree of freedom
EPI	Echo planar imaging
FOV	field of view
FUS	Focused Ultrasound Surgery
GVF	Gradient vector flow
GRE	Gradient echo
HIFU	High Intensity Focused Ultrasound
LR	left-right
MRgFUS	magnetic resonance imaging (MRI) guided FUS
MRI	Magnetic Resonance Imaging
MRT	Magnetic resonance tomography
PEI	Percutaneous ethanol injection
NMR	nuclear magnetic resonance
PRF	Proton Resonance Frequency
PRIDE	Projection-reconstruction imaging with echo-dephasing
PZT	lead zirconate titanate
RF	Radio frequency
RMS	root-mean-square
ROI	Region of Interest
SI	superior-inferior
SNE	Signal to noise elastograme contrast
SNR	Signal Noise Ratio
TE	Echo time
TR	Repetition time
US	Ultrasound
USgFUS	Ultrasound image guided FUS

Acknowledgement

There are innumerable people I would like to acknowledge through my post-graduate career. Due to the complexity of this project, this thesis would never be finished without their collaborations.

I would like to express my deepest gratitude to my supervisors, Dr. Zhihong Huang and Prof. Andreas Melzer for the continuous support towards the completion of my PhD project, and for their patience, motivation, enthusiasm, and immense knowledge that shape the outcomes of this project. I want to thank Dr. Zhihong Huang not only because of her supervision on my research work, but also for her warm heart suggestions on my career direction and moderately concern on my life in Dundee, where far from my homeland. Especially considering her busy various jobs with and within Department, her continuous supervision becomes more estimable and respectable.

I also would like to thank Prof. Sandy Cochran, for his efforts to a well-organized research environment and atmosphere in my first two years work in the ultrasound team. The routinely weekly meetings, although really tough, but actually helped me to construct an academic spirit and sense of time, which means a lot to me.

I would like sincerely acknowledge Mr. Alexander Volovick, application specialist from Insightec Ltd., for his great opinions on realizing using MR compatible robotic arm to guide ultrasound transducers. His training course on operation of ExAblate 2100 system serves throughout my whole thesis work.

I also acknowledge Mr. Vladimir Olsan, design consultant from IBS_{MM} Ltd., for his great support on developing and optimizing applications of robotic arm according to my requirements. He also corrected my paper draft and thesis with great earnest and rigorous although he is not my supervisor.

I want to thank to my fellow Mr. Martin Alexander Rube in MR team, as he had never refused to help me when I encounter technical obstacles relating to MR scanner operation and programming difficulties. He also gave me a lot of great ideas on my designed experiments which I found most of them were of great help.

I would also like to thank my fellow lab member Nhan Le in ultrasound team. I would never forget working with him on one experiment for over 13 hours a day. His help on ultrasound elastography and advanced operation of multi-phased ultrasound transducer made of indispensable parts in my thesis. Mr. Tingyi Jiang is another fellow lab member in ultrasound team I want to acknowledge for his great ideas on mechanical devices fabrication and experiments design. I would be grateful if I have more opportunities to work with these two fellows.

I want to extend my acknowledgement to other team members in MR and ultrasound teams, especially Miss. Zhen Qiu, Mr. Han Wang, and Mr. Keith Johnson for their helpful opinions on ultrasound transducer design and fabrication. I acknowledge Dr. Chunhui Li and Dr. Jing Gao for their kindness help when I just started my PhD study and continuous suggestions and discussions about my project. I want to thank Rui Cao, Cheng Wei, Yunwei Xu, for several months eating and playing together which made a lot of happy memories during the tough research work. I want to extend my thanks to Yongqiang Qiu, Yang Kuang, Guangying Shangguan, Shaozhen Song, Xiaochun Liao, Wei Xiao, Lin Gui, Sinan Li, Jiang You, Yi Cheng, Mengnan Li, Wenhao Zhao, Ioannis Karakitsios, Fabiola Fernandez and other graduate students for making this time at Dundee enjoyable.

I acknowledge Mr. Ben Cox, Ms Karen French and other staff members in MR team for their professional help on smoothing my work towards to my target. I also acknowledge the staff members in the workshop within Department for their help on fabricating mechanical devices and patiently modifying them according to my requirements.

I would like to thank the University of Dundee, the China Scholarship Council, and focused ultrasound surgery in moving organs (FUSIMO) project for offering me financial support to commence my PhD project in the first instance, to do the research work and to use the research data.

Lastly, I would like to share the immense gratefulness towards my family, my parents Jinyou Xiao and Fangru Liu, my sister Ying Xiao, as well as my girlfriend Na Wang, who have been incredibly supportive. I have also been blessed to have shared many wonderful memories with them throughout my study and life. Thank you.

Abstract

Focused ultrasound surgery (FUS) or high intensity focused ultrasound (HIFU), is a promising technique for less- or non-invasively destroying unhealthy tissue deep inside the body, without damage to the skin or surrounding tissues. The procedure has been performed under both diagnostic ultrasound and MRI guidance. Treating cancers and metastases in the liver that are unresectable is a potential application for FUS. However the respiratory motion hindered FUS treatment of liver to become a completely non-invasive technique. The method is currently limited to breath-hold treatments under general anaesthesia that is uncomfortable for patients.

The purpose of this study is to investigate key issues of US and MRI guided real-time target ablation when the target is in free breathing motion state which is similar to human liver motion.

For the ultrasound guided focused ultrasound (USgFUS), diagnostic ultrasound B-mode image was used to track a moving target. The possibility of using strain sonoelastography to assess FUS lesion formation was explored.

Multi-layered tissue mimicking phantoms were designed and fabricated to mimic the graphical features of tumours in human livers in diagnostic ultrasound images. The phantom was then fixed onto three motion setups: 1) controllable 1D reciprocal motion stage, 2) controllable 2D reciprocal motion stage, and 3) ventilator driven balloon to mimic breath motion. Active snake tracking was developed to follow the moving phantom to evaluate the tracking accuracy and speed. This method can achieve a speed of 5~6 frames/second with an error less than 1.0 mm.

Strain sonoelastography is selected to assess lesion formation for FUS. Through comparisons of the elastograms between pre- and post-FUS around the focal zone, useful information about the FUS-induced lesions could be extracted from the elastographic artefacts. The performance of elastography to assess FUS lesion in egg-white Polyacrylamide (PAA) phantoms and fresh sheep livers was tested. The FUS lesions in the experiment samples (PAA phantoms and fresh sheep livers) were recognizable under strain sonoelastography after image processing.

For MRI guided focused ultrasound (MRgFUS), a moving target with similar graphical features of tumours in human liver was tracked via analysing MRI scans. Then letting the ultrasound beam lock onto a moving target was realized via beam-steering by a phased-array HIFU transducer.

An MR compatible robotic arm-INNOMOTION was introduced. A fast localization method was developed to make the robotic arm guided HIFU transducer more efficiently. What is more, it becomes a controllable reciprocal moving setup for investigating the raised issues of MRgFUS for motion tracking in this study.

Two normal volunteers were scanned via MR scanner. The data was used to 1) design tissue mimicking phantoms with similar graphical features to the volunteer livers, 2) design respiratory motion simulator based on the estimated liver motion parameters, 3) and develop motion tracking algorithm based on the image features of the volunteer livers.

The tissue mimicking phantoms appeared to be similar to the structures of volunteer livers in the MR echo planar imaging (EPI) scans. An experiment setup, in which the tissue mimicking phantoms was controlled to move reciprocally, was designed. The off-line MATLAB algorithm based on cross correlation proved to have an acceptable error less than 1.0 mm.

A synchronization system between the target motion and beam-steering was built. Several key problems for motion tracking were studied including how to realize beam-steering with a phased-array transducer, how to map target location in the MR frame to the focus position in the transducer frame, and how to use a step-by-step local sonication series to approximate continuous beam-steering. The system's performance was tested with a series of sonications, in which temperature rises were compared between when the target was moving with and without tracking. A primary conclusion can be made that tracking could decrease the impact of target movement in focused ultrasound ablation. Tracking could be considered as a compensatory method to liver motion caused by respiration during MRgFUS treatment.

In conclusion, the thesis proposed a promising research direction to solve the issue of target motion in FUS treatment of human livers and other abdominal organs. The study achieved the target motion tracking both with diagnostic ultrasound and MRI guidance. The focus steering of HIFU transducer was realized accordingly in the MRgFUS, which can allow the focused ultrasound beam to follow a moving target. The strain sonoelastography had proved to become a potential method to assess FUS lesion formation. This study also brings more issues to be solved, e.g. the noise in diagnostic ultrasound during USgFUS tracking, real-time sonoelastography monitoring lesion formation, and new MRI thermometry that is less susceptible to target motion. The real-time image guided FUS would be more promising by overcoming these technical difficulties.

Chapter 1 Introduction

FUS, with its ability of enabling non-invasive heating and ablation within the tissues deep in the body, gained rapid clinical acceptance in the treatment of tumours in organs such as the prostate, uterus, breast, bone, liver, kidney and pancreas (Medel et al., 2012). The mechanism of focused ultrasound ablation is to apply a continuous or pulsed focal ultrasonic wave at a small treatment region, via a single-element ultrasound transducer or phased ultrasonic elements outside the body or in the rectum. Therefore a thermal coagulation necrosis or mechanical destruction is generated within the interested focal area, deep in the body while reducing the effects on the surrounding tissues and the tissues in the ultrasound propagating path to a minimum level.

The sonography modality and MRI technique are the two main guidance and monitoring tools for FUS, which help plan treatments for precise ablation and treatment monitor.

MRI offers an accurate planning of the tissue to be targeted due to its excellent anatomical resolution and high sensitivity for tumour detection (Cline et al., 1992). And MRI has the ability to visualize the thermally induced lesions reliably and thermal ablation progress can be monitored during FUS treatment. However, MRI still has several drawbacks, such as high cost for operation, unable to carry out real-time imaging and lower spatial resolution in some cases.

In comparison, ultrasonography is an inexpensive imaging modality which provides high temporal and spatial resolution (up to sub-millimetre spatial resolution in plane along the beam direction) (Auboiroux et al., 2012). However, one of the most important problems of US guided FUS ablation is the lack of reliable thermometry and lesion production monitoring.

With the adequate image guidance modalities, FUS appears to have advantages over other radiofrequency modalities especially other thermal treatment methods in terms of its low risk of producing complications. There are still several technical obstacles which limit the development of FUS in clinical applications. The most obvious difficulty is

that treating a large target tissue volume is considerably time consuming, because of size of focus of ultrasound is relatively small and the cooling period after each sonication is unavoidable (Wu et al., 2004b). Organs such as lung or bowl which are filled with gas are not to be treated since ultrasound has a very low propagation through air (Kennedy et al., 2003). Tissues in the upper abdomen and brains also hinder focused ultrasound treatment because the presence of rib cage and skull cranial bones intensively reflect and attenuate the ultrasonic energy through them. The possible solving method is by dedicating operation ultrasonic phased elements, only necessary ultrasonic beams propagate between ribs, which prevents overheating individual ribs (Gao, 2012). Phase adjustments of multi-elements transducer can, to some extent, compensate for irregular cranial thickness and bone density that prevents focusing at tumours in the brain (Hynynen et al., 2006). Blood perfused organs such as liver and kidney entangle the treatment to a more complex situation than homogeneous tissues because blood flow will decrease ultrasound energy deposition at targeted area. During a treatment, the operator should try to avoid ultrasound propagating through vessels area to reduce the influence of blood flow on ultrasound energy deposition. What is more, the abdominal organ motion caused by respiration during the delivery of focused ultrasound may compromise treatment efficacy or, more severely, lead to target mis-location and potential damage to surrounding healthy tissues.

Several techniques exist to handle abdominal organ motion. A straightforward approach is to use respiratory gating (Okada et al., 2006), which employs a respiratory belt to monitor the patient breath, this technique needs general or local anesthetization and normally requires a longer treatment time (Kopelman et al., 2006a). Compared to breath control, motion prediction drastically reduces the treatment time (de Senneville et al., 2007). The drawback is that it could not handle unexpected motion and intermittent non-rigid organ tissue deformation in a breathing cycle (von Siebenthal et al., 2007).

The adaptive method for compensation respiratory motion is based on image guidance (MRI or US), which could provide the real-time position of the target area thus guide the focused ultrasound beam to follow the target (de Oliveira et al., 2010).

The major advantage of the motion correction technique is the fact that the heat deposit at the focus is more efficient. Because in the whole breath cycle, the focused ultrasound beam does not need to be switched off, the acoustic energy could be optimally deposited on the target, ultrasound power as well as sonication time would be drastically decreased. The motion compensation is particularly necessary for the treatment of abdominal tumours where the respiratory induced motion is quite obvious. In theory, correcting motion is the best way to ensure the entire targeted volume has been fully treated non-invasively. To realize focal scanning for large tumours and target motion tracking, the focused ultrasound beam has to be steered either by a mechanical device for single-element FUS transducer or by electronically adjusting phases of multi-element FUS transducers (Auboiroux et al., 2011).

Further requirement for a complete FUS treatment is monitoring method, which accurately depict the ablation performance. These elements must be put together into a complete system that is designed for this purpose, with treatment plan, location verification, motion tracking, ultrasound beam-steering, and treatment monitoring. Image guided FUS remains in its infancy, hepatic ablation during respiratory motion is indescribably a new investigation area within a few clinical trials. Further technological and methodological refinements are necessary to address for FUS on hepatic motion tracking.

1.1 Project aims and objectives

This research focus on motion tracking issues arising in the extracorporeal focused ultrasound treatment of the liver. To achieve this, the key point is to let the high intensity ultrasound beam lock onto the shifting tumours area in order to deliver sufficient ultrasonic energy to generate coagulation necrosis. The whole process should be finished in as short as possible duration while avoiding damage to the surrounding healthy tissues.

The experimental work was mainly divided into two categories, the first part focus on developing a system of sonography guided FUS on motion targets, which includes fabrication of respiratory mimicking devices, image tracking algorithms development,

treatment monitoring methods and system building. The second part is related to MR guided FUS (MRgFUS) for motion tracking, which includes usage of a fully MR compatible mechanical robot, some development of a multi-phased-array HIFU transducer, and a preliminary system designed to integrate different setups for motion tracking.

1.2 Contents of the thesis

The thesis concentrates on basic issues related to liver motion tracking and its possible applications via US/MRI image modality guidance. Chapter 2 focuses on reviewing the basic knowledge of focused ultrasound treatment and introduces several key issues relating to organ motion tracking in focused ultrasound treatment. As shown in Figure 1.1, the contents of chapter 3 to chapter 6 will be structured in two paths, ultrasound image and MRI image guided motion tracking. Chapter 3 explains relevant principles of tracking algorithm and the experiments based on a specifically designed respiratory motion simulator; the focused ultrasound ablations monitoring methods have to be considered as well, chapter 4 mainly focuses on the potential of sonoelastography, which possibly could relate the changes of tissue elastic properties to its coagulation process; For MRgFUS, the focused ultrasound beam has to be steered to lock onto the tissue when it is in a state of motion, which means the system has to have a wide spatial range, a MR compatible robotic arm is taken as the tool to achieve that, chapter 5 makes an introduction of how to use the robotic arm to guide a single-element ultrasound transducer to do ablations in a wide scope; the robotic arm is utilized as a motion provider in chapter 6, beam-steering based on multi-element FUS transducer is realized to make the ultrasound beam to follow a motion target. Besides the principle part of the thesis, chapter 7 draws conclusions for the whole thesis and presents several future investigation directions.

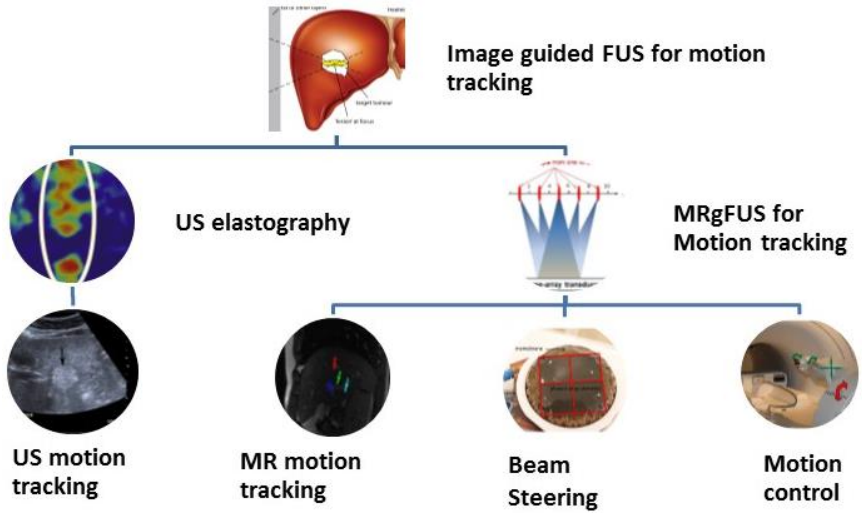

Figure 1.1 Structure of the main contents of this thesis

1.3 List of publications

Peer-reviewed Journal Articles

Xu Xiao, Zhihong Huang, Martin Rube, Andreas Melzer, Fast positioning method for robotic arm assisted MRgFUS (correcting according to the first revision)

Proceedings and Abstracts

1. X. Xiao, N. Le, G. Corner, G. Nabi, A. Melzer et al., Organ motion tracking in USgFUS - A feasibility study using sonoelastography, AIP Conf. Proc. 1503, 135 (2012).
2. Xu Xiao, Zhihong Huang, Alexander Volovick, and Andreas Melzer, Robotic active positioning for magnetic resonance-guided high-intensity focused ultrasound, AIP Conf. Proc. 1503, 217 (2012).
3. Xu Xiao ; Boda Ning ; Zhihong Huang ; Corner, G. ; Cochran, S. ;Melzer, A., Focused ultrasound ablation using real time ultrasound image guidance, The 4th International Congress on Image and Signal Processing & The 4th International Conference on BioMedical Engineering and Informatics (CISP'11~EMBI'11), Shanghai, China, 2011,pp.2335-2338.
4. Xu Xiao, Zhihong Huang, George Corner, Real time target tracking in a phantom using ultrosonic imaging, 40th Annual Symposium of the Ultrasonic Industry Association (UIA), Glasgow, UK, 2011.

Chapter 2 Literature review

The favourable physical interaction between focused ultrasound waves and biological tissues promises a very interesting and unique therapeutic approach, FUS, which is drawing more and more research and clinical interests. The rationale of this technique is to use an ultrasonic transducer to generate sharply converged ultrasound waves which focus on a tiny tissue area deep under the skin and other tissue layers. Sufficient ultrasonic energy can cause a local temperature rise which is high enough to cause local thermal necrosis (a 'lesion') at the focal area, but leaving the surrounding healthy tissues and tissues in the ultrasound path undamaged. In this thesis, the term "high intensity", as commonly found in "high intensity focused ultrasound", is not preferable because it is imprecise and vague in terminology (Goldberg et al., 2005).

The non-invasive property has pushed the research of focused ultrasound ablations to apply in clinical therapy. Diagnostic ultrasound imaging and MRI made a further investigation in precise treatment planning and real-time therapy monitoring. For the last ten years, around 18,000 patients have received FUS for prostate cancer, uterine fibroids, breast tumours, renal tumours, hepatocellular carcinoma, pancreas tumours, and bone malignancies worldwide in Europe, USA and Asia (Al-Bataineh et al., 2012). From a clinical point of view, the numbers of patients treated in controlled clinical studies is rather small. However, from a technical point of view, numerous clinical studies on various organs have proved the feasibility and safety of FUS for non-invasive ablations of deep seated tissue targets.

This chapter presents the history and basic knowledge of focused ultrasound therapy. Different methods of image guided focused ultrasound ablations are introduced in detail and comparisons are performed between them. Clinical FUS systems are summarized and different focused ultrasound transducers are introduced respectively. The technical obstacle, organ motion caused by human breath, which is hindering the further

development of focused ultrasound therapy will be reviewed and some ways to address this problem will be introduced.

2.1 Physical principles of FUS

2.1.1 Generating of focused ultrasound

Ultrasound, as a physical term, is a mechanical oscillating pressure wave with a frequency greater than the upper limit of the human audible range (approximately 20 kilohertz). Most ultrasound devices operate with frequencies from 20 kHz up to several gigahertz (Figure 2.1).

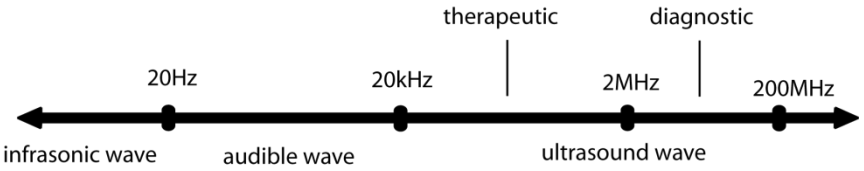

Figure 2.1 approximate frequency ranges of ultrasound

The development of ultrasound technology has resulted from the development of piezoelectricity and electronic technologies. The piezoelectric effect, that certain solid materials exhibit an internal electric field when they are under some external mechanical stress, was first discovered by Jacques and Pierre Curie in 1880 (Currie J, 1880). And the inverse piezoelectric effect, that a mechanical deformation of certain materials can appear when it is in an external electric field, was useful in fabricating transducers to generate ultrasonic waves in air and water. The first successful technological application of ultrasound was an attempt to detect submarines by Paul Langevin in 1917.

Many natural and synthetic materials exhibit piezoelectricity. Synthetic ceramics are widely used for medical ultrasound devices. Common piezoelectric ceramic materials, are lead zirconate titanate (PZT) and a solid solution of the $Pb(ZrTi)O_3$ type. Both materials are relatively versatile, easy and cost effective, and are used to fabricate complex shapes when required (M., 2006). For high power applications, the new PZ50 range of ceramics (ISO, 2007) offers improved high power performance, and allows

small volume elements to be used to generate high power output. The piezo-composite technique is to use a passive polymer to embed the piezoelectric material for improving acoustic performance, e.g. lower acoustic impedance, which offers better results in tissue or water coupled applications.

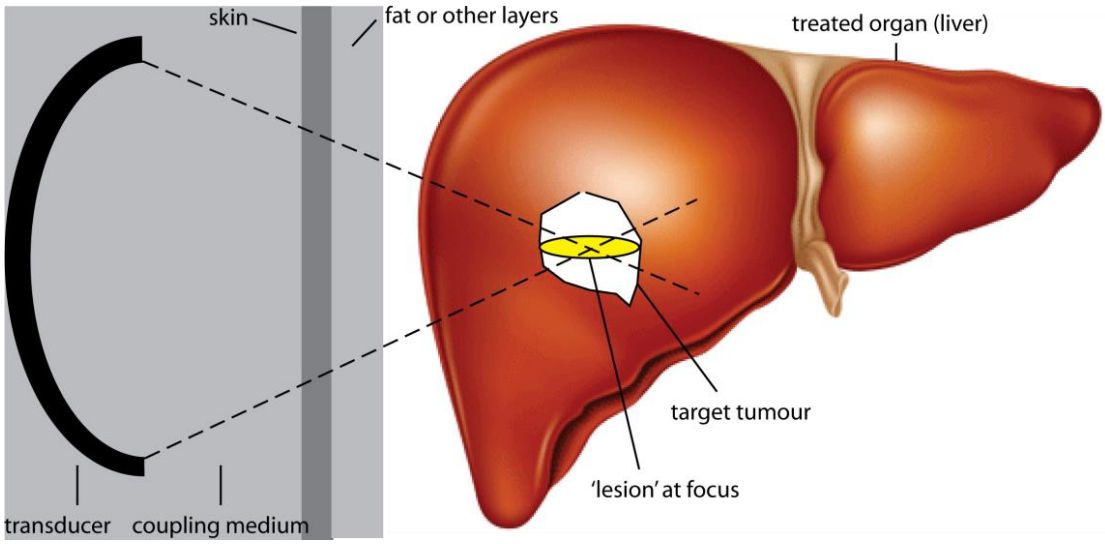

Figure 2.2 Diagram representing focused ultrasound lesion production

Therapeutic transducers are able to focus the ultrasound beam into a tight volume. As shown in Figure 2.2, a typical transducer is in the shape of curved bowl which is used to generate and focus ultrasound beams. Multi-element focused ultrasound array also focus ultrasound beam into a tight volume (Gelat et al., 2011), but with a different principle, wave physics of phasing. The phased-array transducer consists of many small elements, each of which can be pulsed separately. As shown in Figure 2.3, calculated time delays are applied to the elements from right to left to adjust a wave front, allowing the acoustic beam to be focused at a specified location with certain distance and angle. The beam can be dynamically steered in the order of magnitude of hundred milliseconds (e.g. Exablate 2100 system, Insightec Ltd., Tirat, Isreal).

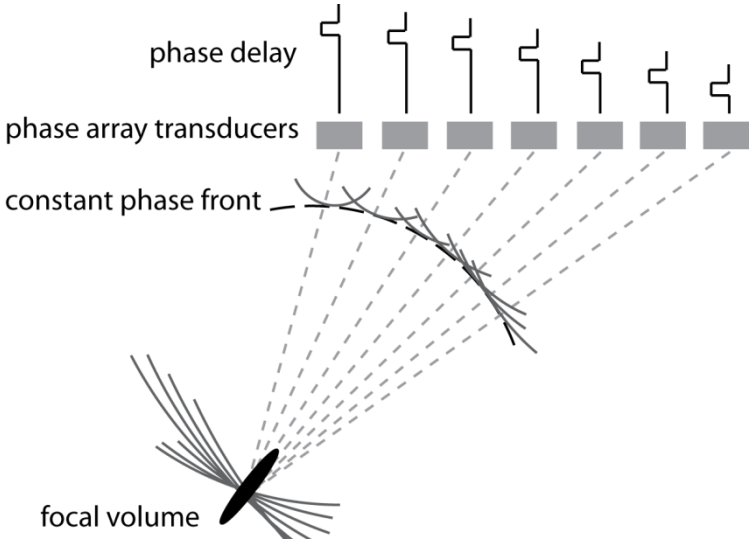

Figure 2.3 Principle of phased-arrays

2.1.2 Propagation of ultrasound in soft tissues

There are several terms used to depict ultrasound fields, e.t, frequency, acoustic pressure, power, sound intensity (Figure 2.4), etc. In an ultrasound wave, acoustic pressure, p (unit: Pa) can be measured via hydrophones. The sound power generated by ultrasonic equipment, Pac (in Watts), can be measured by using radiation force method. The sound intensity, is defined as the sound power per unit area (unit: W/m^2).

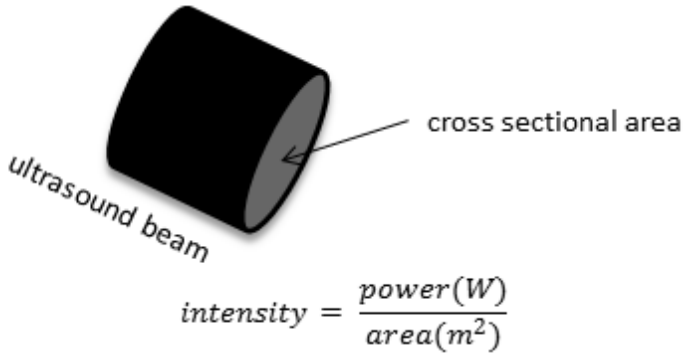

Figure 2.4 intensity of plane ultrasound beam

The intensity of an ultrasound wave decreases as it propagates in tissues. This phenomenon is known as attenuation. The attenuation is defined as ultrasound intensity decreasing with each unit centimetre the ultrasound wave travels. The deeper the

ultrasound wave travels into tissue the greater the attenuation. The measured intensity I of transmitted through a layer of material with thickness x is related to the incident intensity I_0 according to the inverse exponential power law, which can be described by

$$I = I_0 e^{-ax} \tag{2.1}$$

where I_0 is the incident ultrasound intensity at the origin when x equals 0, a is the attenuation coefficient (unit: dB/cm) and x is the distance to the origin.

In aqueous suspensions of cells or other particles, attenuation includes absorption process which converts acoustic energy into heat, and scattering process whereby the particles redirect some of acoustic energy to outside of the beam (Markisz, 2002). In water or dilute aqueous suspensions, the attenuation is often negligible. However, in tissues with dissolved air like lungs, the attenuation is remarkable thus the ultrasound intensity drops drastically (Figure 2.5).

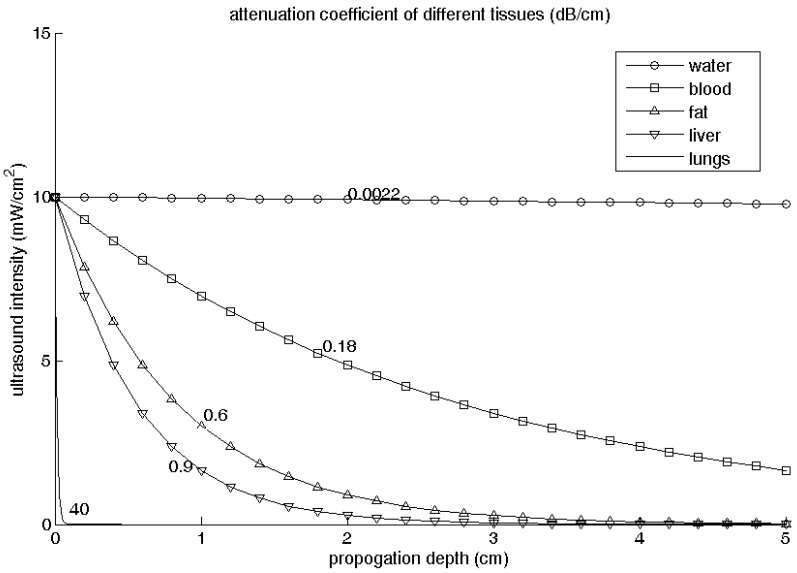

Figure 2.5 Typical values of attenuation in tissue, diagram was drawn in MATLAB assuming the frequency of ultrasound equals 1 MHz (Markisz, 2002).

Neglecting attenuation, linear acoustic waves will propagate through the medium until a change in acoustic impedance is encountered. The ratio of intensity of reflected and the transmitted ultrasound depends on the impedances of the two media at the boundary.

The acoustic impedance (unit: rayl, kg ·) is the product of the density of the medium and the velocity of ultrasound in the medium. In the simple case of perpendicular incidence (Figure 2.6), the amplitude of reflected waves can be calculated by

$$R_x = \left(\frac{Z_1 - Z_2}{Z_1 + Z_2}\right)^2 = \left(\frac{2}{\frac{Z_1}{Z_2} + 1} - 1\right)^2 \quad 2.2$$

where R_X represent the intensity or energy reflection coefficient when waves propagate through medium 1 and encounter medium 2 at a normal angle (Markisz, 2002). Thereby, strong reflections occur when there is a large difference between the acoustic impedances of the two media, e.g. bone or with soft tissues, R_X equals 0.4~0.6, resulting in nearly half of the incident energy reflected back. When an incident wave encounters the boundary at an oblique angle, there will be more power reflected by the boundary. The acoustic impedance in other materials are shown in Table 2-1.

Table 2-1 Approximate acoustic impedances of selected materials (Markisz, 2002)

Material	Acoustic impedance (rayl)
Air (standard situation)	0.0004
Water	1.5
Blood	1.61
Fat	1.38
Liver	1.65

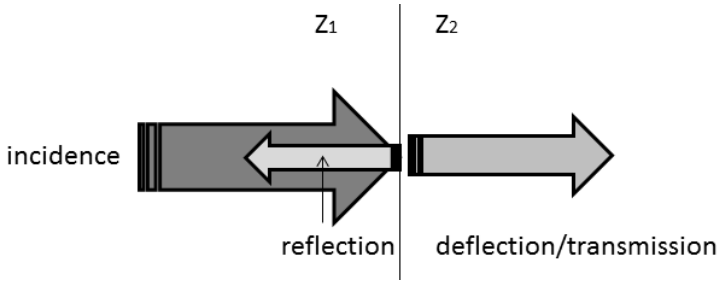

Figure 2.6 When ultrasound incidence perpendicularly to the medium, the strength of the reflected and transmitted ultrasound pulses are determined by the impedances of the two media at the boundary.

The behavior of acoustic wave travelling linearly is with the assumption of a small-signal wave propagating through a homogeneous medium, both are regular situations for focused ultrasound applications. When the amplitude of sound waves becomes large or if the medium is nonlinear, the wave propagation nonlinearity effect is not negligible. The nonlinearity of a propagation medium can be described by the term, B/A, where A and B are temperature dependent coefficients in the Taylor series expansion for wave propagation. The speed of ultrasound, *c*, with large amplitude in a medium is given by

$$c = c_0 + 0.5(B/A)u \qquad 2.3$$

where c_0 is the speed of sound with a small amplitude wave in the same medium, and u is the particle velocity in the medium (Haar and Coussios, 2007).

As a sine wave propagates through an inhomogeneous medium, the speed of sound is no longer uniform after propagation through a few wavelengths because the nonlinearity of the medium will change the wave speed at a local region. And the pure sine wave can be modified to become increasingly saw-tooth. The additional higher frequency harmonics increase the absorption and heating, typically in the focal region of a focused ultrasound transducer.

2.1.3 Heat generation and transfer in biological tissues

The rationale of focused ultrasound induced heating refers to the conversion of ultrasonic energy into thermal energy via absorption by the medium. When using an

external ultrasound applicator to heat a homogeneous medium, the absorbed ultrasound power density, Q_v, at location x, is proportional to the wave energy flux, which equals to the ultrasound intensity (Cochard et al., 2009).

$$Q_v = -\frac{dI(x)}{dx} = 2a_a(x) \cdot I(x) \quad 2.4$$

where $I(x)$ is the time averaged of the ultrasound intensity, and $a_a(x)$ is the ultrasonic absorption coefficient.

The heat source Q_v turns out to be complex as it depends on the nature of the focused ultrasound field. By initializing the temperature increase rate can simplify the calculation of Q_v, under the assumption that the conduction effect is negligible at the beginning of heating (Sun et al., 2008).

$$Q_v = \rho C_p \frac{\partial T}{\partial t}\Big|_{t=0^+} \quad 2.5$$

where C_p is the specific heat capacity of the medium at a constant pressure.

Regarding to the heat transfer, thermal processes in living tissues can be described using the Pennes' bio-heat transfer equation:

$$\rho_t C_t \frac{\partial T}{\partial t} = k_t \nabla^2 T - w_b C_b (T - T_a) + Q_m + Q_v \quad 2.6$$

where $k_t \nabla^2 T$ is the thermal conduction, $w_b C_b (T - T_a)$ represents the influence of blood perfusion, Q_m represent the volumetric metabolic heat, and Q_v is the heat source coming from absorbed ultrasound power (Shih et al., 2005). The parameters ρ_t, C_t, and k_t are the density, specific heat capacity, and thermal conductivity of the tissue, the subscript t means these parameters might vary during the heat transfer process because of temperature changing, although the changes are always neglected in calculation; w_b,

C_b, and T_a are respectively the blood perfusion rate in the heated region, specific heat capacity of blood, and temperature of arterial blood, from our experience, the temperature changes for the blood is neglected during focused ultrasound ablation. The short duration of sonication makes the variable Q_m very small (about 0.0001 cal/(cm^3 s)) as well. Thus the simplified bio-heat transfer equation is given as:

$$\rho_t C_t \frac{\partial T}{\partial t} = k_t \nabla^2 T + Q_v \qquad 2.7$$

which is still a practical approach for modelling the biological heat transfer processes.

2.1.4 Dosimetry for heat induced tissue necrosis

Sapareto and Dewey proposed a cumulative equivalent minutes (CEM) model to predict the thermal damage caused by focused ultrasound exposures (Sapareto and Dewey, 1984). It defines an equivalent relation between a known temperature time history at a given location and a time period of constant thermal exposure at 43 ℃, which is given by:

$$t_{43}(x,y,z) = \int_0^{t_{final}} R(T(t))^{43-T(t)} dt \qquad 2.8$$

where *T(t)* is the changing temperature regarding to time history, the function $R(T)$ is approximated as an empirical piecewise-constant:

$$R(T) = \begin{cases} 0.5 & if\ T > 43°C \\ 0.25 & if\ 37°C < T < 43°C \\ 0 & otherwise \end{cases} \qquad 2.9$$

A simplified discrete expression for equation 2.8 (Haar and Coussios, 2007) is as follows:

$$t_{43} = R^{(T-43)} \Delta t \qquad 2.10$$

where T is the average temperature over a time Δt. The threshold thermal dose value for tumour tissue coagulation was an equivalent duration of 240 minutes at $43°C$. Though

the thermal dose may vary within different tissues, this limit value provides an effective way to estimate the margin of necrotic tissue by locating the 240 minutes thermal dose contour around the focus (Damianou and Hynynen, 1994). In previous experience, the thermal injury could only occur when the temperature near the target area is over 55°C for a specific time period.

2.1.5 Cavitation

Except thermal effect of focused ultrasound, there is another phenomenon named as acoustic cavitation which is also important for focused ultrasound mechanism. Acoustic cavitation can be defined as the interaction of a focused ultrasound field with micro gas bubbles (Hynynen, 2007). Cavitation bubbles may form due to boiling of fluid or by the growth of cavitation nuclei within the propagation medium. After formation, the micro bubbles oscillate in two forms, stable cavitation which refers to bubble oscillating steadily in an ultrasound field and inertial oscillation which means these bubbles are going to collapse under high intensity ultrasound field (as shown in Figure 2.7). The likelihood of cavitation occurring during a given ultrasound exposure increases as the ultrasonic frequency decreases.

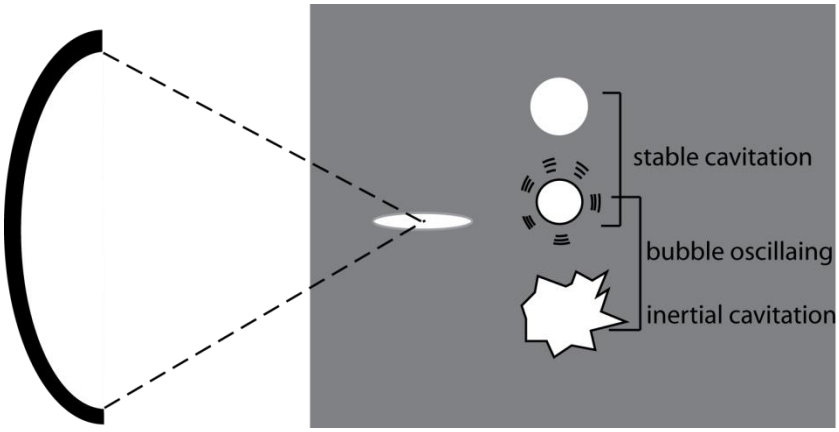

Figure 2.7 Schematic illustration of the cavitation effect of focused ultrasound

The stable cavitation intercepts and radiates energy to the surrounding tissues, which highly localize shear stress, thus causes cell damage. And the collapse of bubbles in inertial cavitation results in localized high acoustic pressure of several thousand atmospheres, which causes damage of the exposed tissues. The effects of inertial

cavitation present safety concerns for human, and are more significant than stable cavitation in clinical therapy.

2.2 FUS transducers and FUS treatment process

2.2.1 Focused ultrasound transducers

FUS devices for present clinical use are mainly divided to three categories: extracorporeal, trans-rectal and interstitial (Zhou, 2011).

Extracorporeal transducers are used for targeting organs that are readily accessible through skin. The trans-rectal devices used for the treatment of the prostate have been developed for the treatment of benign and malignant prostate diseases and can be inserted per rectum (Figure 2.8). Interstitial probe is miniaturized linear arrays of ultrasound transducers which are integrated into a probe with a coupling balloon and piercing tip.

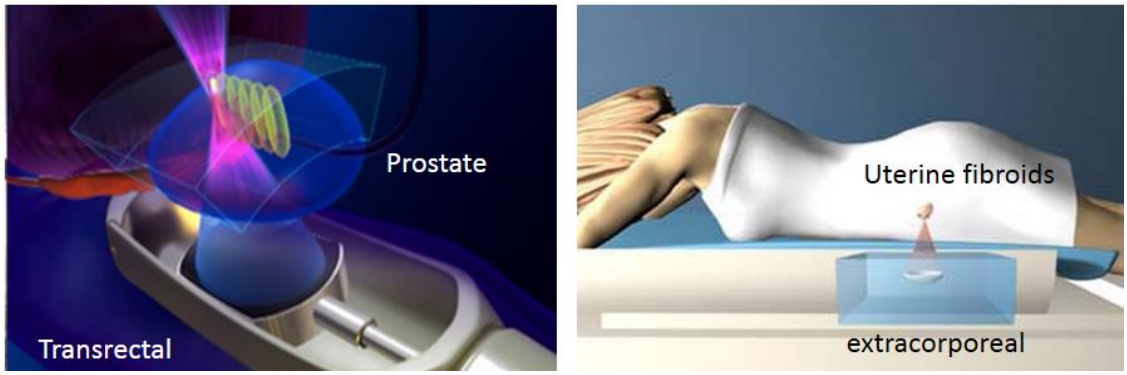

Figure 2.8 Different FUS devices. Left is a trans-rectal probe for treating prostate tumour (EDAP-Technomed, Lyon, France), right is an extracorporeal probe for treating uterine fibroids (Exablate 2000, Haifa, Isreal).

A summary of most popular HIFU system for clinical use (Zhou, 2011) is shown in

Table 2-2. Their specific clinical applications are introduced in the next section of this chapter.

Table 2-2: Summary of popular HIFU systems for clinical use

Model	Category	Focusing method	Imaging guidance	Clinical applications
FEP-BY02	Extracorporeal	251 elements	ultrasound	liver, kidney, breast, pancreatic, bone
Sonatherm1	interstitial	acoustic lens	ultrasound	kidney
HIFUNIT9000	extracorporeal	6 elements	ultrasound	uterine fibroid, pancreatic, liver, bone
Model-JC	extracorporeal	acoustic lens	ultrasound	liver, kidney, breast and uterine fibroid
ExAblate2000/2100/3000/4000	extracorporeal	multi-element	1.5/3.0T MR	uterine fibroids, breast, liver, bone, neurosurgery
SuperSonic	extracorporeal	multi-element	1.5/3.0T MR	neurosurgery
Sonablate 500	Trans-rectal	2 elements back-to-back	ultrasound	prostate cancer
Ablatherm	Trans-rectal	Single concave element	ultrasound	prostate cancer

2.2.2 Typical therapy course of FUS treatment

There are different therapy courses of FUS, which depend on the treated organs and therapy modalities which were mentioned in section 2.2.1. Generally speaking, it starts

with the positioning of the patient on a cradle within the range of imaging modalities and the coupling of the ultrasound device to the patient using degassed water or ultrasound gel. Depending on the treated organ, for example prostate tumour ablation, FUS is performed under general or local anaesthesia. For breast tumour or uterine fibroids, sedation might not be necessary. For treatment planning, MR or ultrasound images of the intended treatment region as well as the focused ultrasound pathway are needed. With this information, a therapy plan can be calculated by determining the positioning of the single-element ultrasound source or the delayed time of each element in a phased-array ultrasound transducer. The therapist defines all additional parameters necessary for the ablation of the entire targeted structure such as acoustic power, ablation duration, and position of image plane to monitor sonication, etc. In the next step the target tissue is ablated under image guidance. Once the ablation process is completed, contrast enhanced imaging, e.g. with MRI, allows a first evaluation of the therapy result.

2.3 Applications for FUS

Thermal ablation of tissue with FUS has gained increasing clinical interest. Today, a rapid and ongoing technical development and clinical research on FUS is visible. So far, clinical studies have been performed to treat tumours of different organs. A total number of more than 20,000 patients were treated using FUS in the previous 15 years and they are approximately distributed as Figure 2.9 shown (Al-Bataineh et al., 2012). In this section an overview of actual clinical activities in these fields was given.

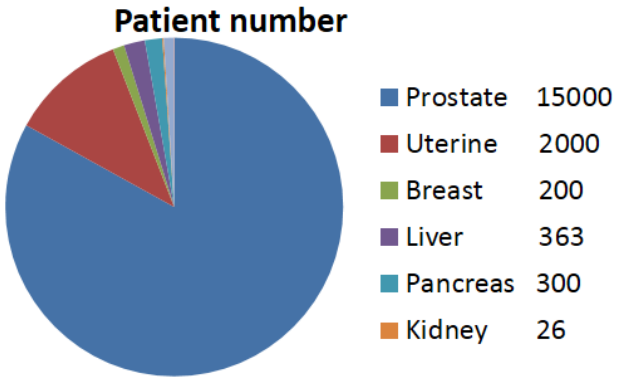

Figure 2.9 Pie chart of clinical trials of FUS treatment from last 15 years according to (Al-Bataineh et al., 2012).

2.3.1 Prostate cancer

Prostate cancer is one of the most pervasive types of cancers for men. And the ablation of prostate tumours is the most commonly clinical application of focused ultrasound. Up to date, more than 20,000 patients with prostate cancer have been treated by FUS around the world (Europe, Asia and North America without USA) (Jenne et al., 2012). Two therapy systems are commercially available: The Ablatherm® (EDAP-Technomed, Lyon, France) and the Sonablate® (Focus Surgery, Indianapolis, IN, USA) working with trans-rectal ultrasound. The first focused ultrasound treatment series of primary prostate cancer in UK was reported with a 92% disease-free rate (Ahmed et al., 2009). Serious effects of FUS are infections of the urinary tract, prolonged urinary retention, stress incontinence, erectile dysfunctions, impotence, infravesical obstruction and typical skin burn, thermal injury to adjacent vital structures. Nevertheless, many promising results (Ahmed et al., 2009, Blana et al., 2004, Beerlage et al., 1999, Uchida et al., 2002, Gelet et al., 1999, Azzouz and de la Rosette, 2006, Poissonnier et al., 2007, Blana et al., 2008) offer the potential that FUS may become a well-accepted treatment option due to technical developments and improved treatment protocols.

2.3.2 Uterine fibroid

Uterine fibroids are the most common benign pelvic tumours in females that originate from smooth muscle layer of the uterus. There are normally found in women's middle and later reproductive years with an occurrence of 25% for white and 50% for black women (Wise et al., 2005). Besides the non-invasiveness and organ preservation capability, the cost effectiveness of image guided FUS has been found to be reasonable and comparable to alternative treatment methods (O'Sullivan et al., 2009), such as surgery, radiofrequency ablation, endometrial ablation, etc. More than 2000 patients were enrolled in clinical FUS studies from 2007-2010. Most of these trials were achieved using ExAblate 2000 systems (InSightec Ltd., Tirat Carmel, Israel) (Al-Bataineh et al., 2012), Haifu JM therapeutic system (JM2.5C, Chongqing Haifu Technology Co., Ltd., China) (Zhang et al., 2010), and HIFUNIT 9000 tumour therapy system (Shanghai Aishen Technology, Shanghai, China) (Meng et al., 2010). Occasional complications were reported as urinary infection, temporary nerve irritation,

skin redness and others. However, all these complications can be avoided by accurate and careful treatment planning and monitoring.

2.3.3 Bone metastasis

Bone metastasis is a class of cancer metastases that results from primary tumour invasion to bone. It is a generally metastatic disease from cancer originating elsewhere in the body, including prostate (Guise, 2010), breast (Lacroix, 2006), and lung cancers (Hirano et al., 2005). The main symptom of bone metastasis is severe pain which degrades the quality of life for patients (Coleman, 2006). Focused ultrasound could rapidly heat the targeted bone cortex and adjacent tumour tissue because bones have a higher absorption coefficient for ultrasound than soft tissues. And the lower thermal conductivity of bones leads to a localized effect within the targeted focused ultrasound beam (Jenne et al., 2012). After combined with image guidance, focused ultrasound ablation may offer advantages of no radiation, easy repetition for pain control, and precise targeting over traditional treatments such as radiotherapy and chemotherapy. Focused ultrasound has CE approval for palliative care for bone metastasis. A multicentre study to evaluate the safety and effectiveness of the ExAblate 2100 conformal bone system (InSightec Ltd., Tirat Carmel, Israel) in the treatment of pain resulting from metastatic bone tumours is currently under way. Seventy-two percent of patients reported a significant pain reduction and all patients were able to reduce their medication 3 months after the focused ultrasound ablation (Liberman et al., 2009). The FUS for bone palliation has shown to be entirely side-effect free, however further large scale, long-term randomized studies need to be performed. Of particular importance, attention should be paid to avoiding thermal damage to adjacent organs, nerves, bowl wall, or affecting bone breaking.

2.3.4 Breast cancer

Breast cancer accounts for 22.9% of all cancers in women worldwide . Conventional treatment methods for patients with breast cancer include surgery followed by adjuvant therapy (chemotherapy, radiation, or both). While the image guided FUS technique, as discussed above, can offer a distinct advantages of decreased complication risks (bleeding, infection, seroma formation, chronic incisional pain, etc) and cosmetic

outcome (avoiding surgical removal). Most clinical trials were delivered using Model-JC system (Haifu Tech. Co. Ltd., Chongqing, China) and ExAblate 2000 system (InSightec Ltd., Tirat Carmel, Israel). Wu et al. found a margin approximately 1.5-2.0cm around the visible tumour after focused ultrasound ablation in breast tissue (Wu, 2006, Wu et al., 2003a, Wu et al., 2007). The average tumour size reduced 90% compared to the initial tumour volume, and the recurrence free survival rates was more than ninety percent for 5 years follow-up period (Wu, 2006).

2.3.5 Trans-cranial FUS for neurosurgery in the brain

Brain cancer comprises 1.4 % of all cancer types and 2.4 % of all cancer deaths. In the UK, in 2008, there were 3,674 deaths as a result of brain and other central nervous system cancers (data from Cancer Research UK). Treatment of the brain through the intact skull is probably the most innovative trend in clinical FUS because no invasive trajectory to the target is necessary in ideal conception. Hemispherical phased-array transducers were designed to surround the brain with a large scale to deliver enough energy through bones as well as prevent harm to the skull. A complete computed tomography (CT) scan is required to perform for the correction of phase aberrations caused by inhomogeneous structure of the cranium. The ExAblate 3000/4000 system (InSightec Ltd., Tirat Carmel, Israel) and the SuperSonic brain therapy system (SuperSonic Imagine, France) were developed for delivering clinical trials. Some clinical results have shown that for neuropathic pain, there is a mean pain relief of 68% after the treatments (Martin et al., 2009). Considering the small number of patients in controlled clinical studies, more clinical trials are needed to prove and optimize this technique, such as deciding the maximum induced temperature or modifying the device for future better results (McDannold et al., 2010). For brain tumour ablation, facet rhizotomy and movement disorders, the clinical trials are not enough to generally conclude a therapeutic effect (Medel et al., 2012).

With image guidance, the FUS is being investigated for numerous promising applications, including targeted drug delivery and sonothrombolysis. Targeted drug delivery is mainly based on two mechanisms, one is focused ultrasound with the systemic administration of micro bubbles, this can induce a transient local opening of

the blood brain barrier (BBB) (McDannold et al., 2005, Mesiwala et al., 2002, Sheikov et al., 2004, Choi et al., 2007, Rapoport et al., 2007), the other is destruction of micro bubbles that produce shock waves which disrupt liposomes and cause delivery of its contents (Schroeder et al., 2009, Meijering et al., 2009). Although the feasibility of targeted drug delivery using image guided FUS was demonstrated, the clinical efficacy of this approach remains unclear. Patients with hemorrhagic and ischemic stroke may benefit from sonothrombolysis (FUS for clot clysis) compared with current use of thrombolytic drugs such as the tissue plasminogen activator (tPA) (Daffertshofer and Hennerici, 2003). Sonothrombolysis within the main brain arteries might be possible while potentially minimizing the hemorrhagic complications associated with the use of thrombolytics (Alexandrov et al., 2004b, Alexandrov et al., 2004a). The main constraint on the application of sonothrombolysis is the time limitation associated with ischemic stroke.

2.3.6 Kidney cancer

Surgery is the gold standard treatment solution for kidney cancers, but it is accepted that a non-invasive way like FUS is becoming preferred, considering the risks of surgery in elderly patients. Few clinical studies were performed to ablate local renal tumours or metastatic kidney tumours using focused ultrasound (Klingler et al., 2008, Illing et al., 2005, Wu et al., 2003b). The treatments were delivered using Model-JC tumour therapy system (Haifu Tech. Co., China) and Laparoscopic HIFU system Sonatherm1 (Misonix Inc, Farmingdale, NY, USA). To control the respiratory shift of targeted kidney, general or epidural anethesia were performed for patients. Klingler et al. found homogeneous thermal damage within the targeted renal (Klingler et al., 2008). Illing et al. showed that 67% of tumours were ablated consistently (Illing et al., 2005). For metastatic and advanced kidney cancers, Wu et al. proved that 90% of patients felt pain relieved after FUS treatment (Wu et al., 2003b). Extracorporeal renal FUS might be effective in specially selected body regions, since ablation of tumours lying close to the ribs runs the risk of overheating (Kohrmann et al., 2002).

2.3.7 Pancreas cancer

No effective treatment offers survival benefits for patients with pancreatic cancers due to the difficulty in early detection of small pancreatic tumours. The five year survival rate is the lowest among other cancer types, as only 2 %. FUS may play a prominent role in future as a result of its non-invasiveness, conformal capabilities of ablating large tumours, and pain relief (Zaitsev et al, 1996; Ganaha et al., 2005). More than 300 patients were enrolled in FUS therapy, or FUS with chemotherapy, to treat localized advanced pancreatic cancers (Jung et al., 2011, Wu et al., 2004b, Wu et al., 2005b, Xiong et al., 2009). These treatments were delivered using three FUS systems from China, extracorporeal ultrasound guided Model-JC system (Haifu, Chongqing, China), tumour therapy equipment HIFUNIT-9000 (Shanghai A&S Sci-Tech Co., Ltd., Shanghai, China), and FEP-BY system (Yuande Biomedical Engineering limited Corporation, Beijing, China). Previous results showed that the average tumour reduction rate was 50% after treatment with FUS alone (Wu et al., 2005b), with occasional minor complications (mainly second or third degree skin burns) were detected after the pancreatic FUS therapy (Wu et al., 2004b). Randomized controlled trials are now needed to evaluate the effectiveness of FUS for pancreatic tumours.

2.3.8 Liver cancer

Because of tumour multifocality, portal vein invasion and underlying advanced cirrhosis, many patients with liver tumours are not good candidates for surgical resection (Wu et al., 2005a). Some of them are not suitable for radio frequency ablation (RFA) or percutaneous ethanol injection (PEI) due to the size and location of the tumours (Zhu et al., 2009, Zhang et al., 2009). With the advent of modern imaging techniques, the practical applications of extracorporeal FUS for the treatment of liver tumours are becoming possible. Clinical trials are mainly based on extracorporeal Model-JC tumour therapy system (Haifu Technology Company, Chongqing, China) which is with ultrasound image guidance and ExAblate 2000 device which is with MRI image guidance. All patients were under general or epidural anaesthesia to prevent mobilization during the treatment and relevant pains. The assessment methods includes contrast enhanced MRI (Leslie et al., 2008), dynamic contrast enhanced CT imaging

(Zhang et al., 2009) and Dopller ultrasound. Two main parameters are the absence or obvious reduction in the tumour vascularity and the shrinkage of the treated lesions (Wu et al., 2004a). Previous results showed that complete tumour necrosis were achieved in 69.6% (Zhu et al., 2009) and 50% (Zhang et al., 2009) of lesions after the first FUS treatment. With the second FUS treatment all the tumours achieved complete necrosis with the absence of tumour blood supply and shrinkage (Zhang et al., 2009, Zhu et al., 2009). In a study performed by Wu et al. FUS combining with chemo-embolization offered more benefits in reducing the size of large volume tumours and thus a better survival rates for the patients (Wu et al., 2005a, Jin et al., 2011). The complications for FUS on liver tumours include skin redness and burns, necrosis of the ribs and vertebral body, pain and skin numbness, biliary obstruction, symptomatic pleural effusions, and fistula formation (Jung et al., 2011, Li et al., 2009).

The challenge for image guidance FUS are the effects of the liver's motion and the rib cage. In the most serious situation, both the rib cage and the HIFU transducer move with the respiratory motion. One way to overcome organ motion during FUS is through respiratory gating which uses controlled apnea on anesthetized subjects (Kopelman et al., 2006b) or through repeated breath-holds using training and feedback (Okada et al., 2006) to ensure that the liver repeatedly returns to the same location. For the rib cage presence, partial rib cage removal is the general method to produce an enough acoustic window for the focused ultrasound to propagate to the focal region. To achieve a complete non-invasive method, larger transducers are used to reduce the distributed energy in the ultrasound beam path over ribs or special phased-arrays transducer is used which focus the ultrasound beam between the ribs (Botros et al., 1997, Civale et al., 2006, Gao, 2012).

2.4 Motion compensate in FUS

2.4.1 Exist techniques to handle organ motion

Several techniques exist to handle abdominal organ motion. A straightforward approach is to use respiratory gating (Okada et al., 2006), which employs a respiratory belt to monitor patient breathing. As shown in Figure 2.10, in the FUS treatment, the patients need to hold their breath for a short period and the focus of the FUS transducer is fixed

at one position. Only when the target tissue is in the treated area of the ultrasound beam in a respiratory cycle, the focused ultrasound is switched on to deliver energy, at the rest of the respiratory cycle, the focused ultrasound is switched off to avoid ablating surrounding healthy tissue. As respiratory gating generally increases treatment time, controlled apnea with general or local anesthetization is used (Kopelman et al., 2006a) to lengthen the static period of the motion organ.

Motion prediction is getting closer to real motion tracking. A system that generates a map of motion fields during an initial learning phase based on MR GRE data (de Senneville et al., 2007). The motion field of the most similar image in the map is then used to correct the target position. The estimation for the focal area position for the next cycle is under the hypothesis of periodic motion. Compared to breath control, this method drastically reduced the treatment time. The drawback is that it could not handle unexpected motion in a breathing cycle. Moreover, it only calculates liver displacements periodically and is not able to solve intermittent non-rigid organ tissue deformations (von Siebenthal et al., 2007).

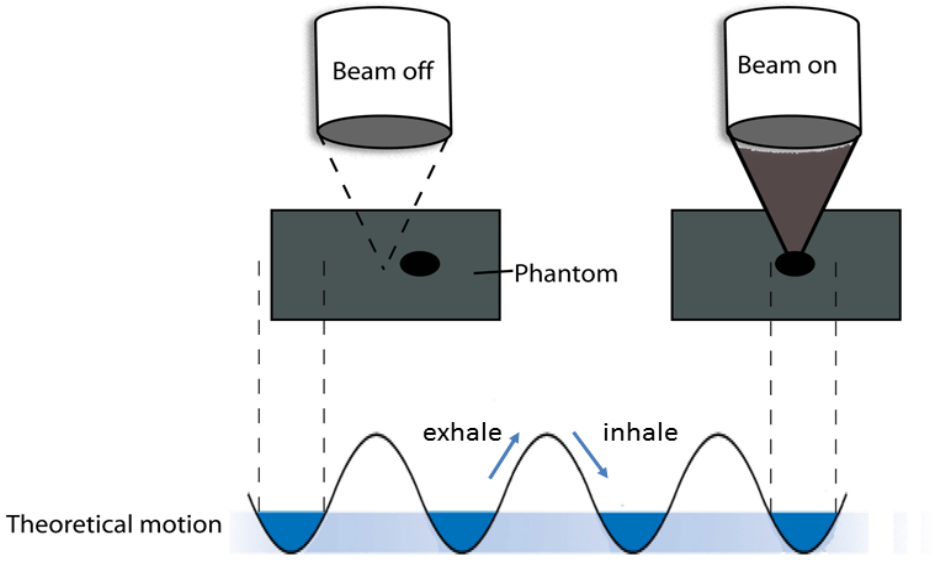

Figure 2.10 Respiratory gating method to handle respiratory motion

The adaptive method for compensation respiratory motion is based on MR or US scans which could provide the real-time position of the target area thus guide the focused ultrasound beam to follow the target.

Motion tracking based on MR scan normally has to sacrifice image spatial resolution to achieve a near real-time imaging speed. Moreover, it might also need a trade-off between high time resolution and low precision of the MR thermometry (Ries et al., 2010).

US-based motion tracking was firstly reported in phantoms undergoing 1D periodic and rigid motion of small amplitude (de Oliveira et al., 2010). The drawback for US image guided motion tracking is that it lacks a good assessment method for lesion formation.

Integration of US and MR imaging is also an option for guiding FUS in the respiratory situation, in which the real-time US image captures the target motion and the MRI scan provides the thermometry. Image fusion from the two modalities (Tang et al., 2008) or markers on the US probe are needed to locate the US image plane in the MRI coordinate system. The MR compatibility of the US imaging probe has to be considered as well (Feinberg et al., 2010, Viallon et al., 2010, Auboiroux et al., 2012).

The major advantage of the motion correction technique is the fact that heat deposit at the focus is more efficient. When acoustic energy is optimally deposited on the target, ultrasound power as well as sonication time would be drastically decreased. The motion compensation is particularly necessary for the treatment of abdominal tumours where the respiratory induced motion is quite obvious. In theory, correcting motion is the best way to ensure that the entirety of the targeted volume has been properly and totally treated invasively and rapidly. To realize focal scanning for large tumours and target motion tracking, the focused ultrasound beam has to be steered either by mechanical device for single-element FUS transducer (Figure 2.2) or by electronically adjusting phases of multi-element FUS transducers (Figure 2.3). The advantage of multi-element FUS transducer are its programmable channels which allow fast beam-steering and the ability to follow a complex trajectory (Auboiroux et al., 2011).

2.4.2 Image guidance for FUS

The crucial impetus for FUS was the development of modern radiological imaging modalities as diagnostic ultrasound or MRI which allow non-invasive therapy guidance.

The development of MRI guided FUS treatment was first proposed by Cline et al (Cline et al., 1992). MRI offers an accurate planning of the tissue to be targeted due to its excellent anatomical resolution and high sensitivity for tumour detection. The temperature-sensitive MRI provides the ability of closed-loop control of energy deposition, with temperature accuracy of 1 ℃, spatial resolution of 1mm, and temporal resolution of 1s. Therefore, MRI has the ability to visualize the thermally induced lesions reliably and thermal ablation progress can be monitored during FUS treatment.

However, MRI still has several drawbacks, such as high cost for operation, unable to carry out real-time imaging and lower spatial resolution in some cases. Khokhloca et al. (Khokhlova et al., 2009) held the view that the temporal and spatial averaging effect of MRI thermometry greatly underestimates the temperature rise by continuous FUS exposure. Moreover, it has been reported that MRI is less incapable of visualizing FUS-induced lesions in Thiel-embalmed tissue (Karakitsios et al., 2014), which provides a lifelike flexibility of body parts. Thiel-emblamed technique (Thiel, 1992) which relies on a mixture of salt compounds and very low amounts of volatile formaldehyde and formalin to effect fixation of tissue with a number of unique properties. Thiel-emblamed tissues have excellent colour preservation of muscle, viscera, and vasculature. The visualization of FUS-induced lesions in Thiel-emblamed tissues using MRI is still under study.

In comparison, ultrasonography is the most inexpensive imaging modality and it provides high temporal and spatial resolution (up to sub-millimetre spatial resolution in plane along the beam direction) (Auboiroux et al., 2012). However, one of the most important problems of US guided FUS ablation is the lack of reliable thermometry and lesion production monitoring. In other words, there is little contrast between normal tissue and FUS ablated tissue in an ultrasound image. The thermally ablated region is not visible on standard B-mode images unless gas bubbles have been induced. But several techniques including sonographic thermometry, ultrasound elastography and backscattered ultrasound are under investigation to address this problem.

Fast imaging for motion targets tracking

One of the limitations for abdominal FUS treatment is patient respiratory, this limitation is well known and has led to an increased number of research studies which have been carried out. For FUS therapy systems, movements are obstacle because they directly affect the precision and efficiency of the treatment. Significant movements are causing mismatch, in this situation, the acoustic beam could be targeting at healthy tissues and damaging them. Moreover, the overall dose delivered to tumorous tissues can be insufficient to cause thermal necrosis. Abdominal organs can move up to 20 mm within a breathing cycle with a speed up to 15 mm/s (Davies et al., 1994, Bryan et al., 1984, Ross et al., 1990).

To address issues caused by motion target in FUS ablation, first of all, the respiratory movements are to be analysed, if possible, its movement is to be tracked during the FUS therapy. In order to realize that, finding proper imaging modalities with fast frame rate for capturing motion target is of importance.

Medical ultrasonography is the most inexpensive imaging modality, which is for visualizing subcutaneous body structures including tendons, muscles, joints, vessels and internal organs. Many different types of images can be formed using ultrasound, the most well known type is 2D cross-section B-mode image, which is largely free of geometrical distortions and provides high spatial resolution (up to sub-millimetre spatial resolution inplane along the beam direction). It provides images in real-time, rather than after an acquisition or processing delay. Although it is relatively dependent on a skilled operator, by carefully choosing probes and setting its field of view, the range of an abdominal motion target could be covered by an ultrasound imaging system. Thus, ultrasonography is the first option for visualizing abdominal respiratory motion and guiding FUS therapy. Considering the graphical properties of tumours in human organs, a proper target segmentation method should be developed to lock onto tumours with irregular shapes. Active snake becomes as the option since it is an energy minimizing deformable curve, which theoretically can lock onto any graphical shapes (Kass et al., 1988).

The drawback of ultrasonography is that it produces in general little contrast between tissue and FUS-induced lesion and to date, ultrasound-based temperature monitoring has not been validated under a clinical scenario.

MRI, nuclear MRI (NMRI), or magnetic resonance tomography (MRT) is a medical imaging technique used in radiology to visualize the internal structures of the human body to investigate both anatomy and function in health and disease.

Since the first days of human MR imaging from the late 1970's (Mansfield et al., 1978, Damadian et al., 1977, Pykett and Mansfield, 1978), scanning time has presented a series of practical limitations. The practical reality of ordinary structural imaging is that normal subjects are willing to tolerate perhaps an hour of lying inside of the imaging magnet, and are able to stay still for more than 15 minutes. Both NMR contrast and signal to noise ratio (SNR), however, are time-dependent phenomena. As a consequence, scanning speed and image quality have been at odds for all types of MRI.

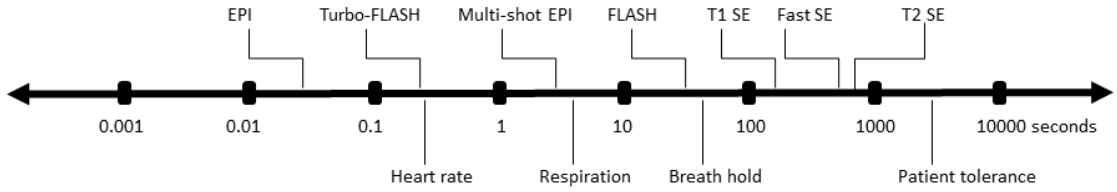

Figure 2.11 Physiological processes and imaging speeds of general MRI methods.

As shown in Figure 2.11, to avoid image artefacts, scan times must not be longer than the duration of motion. To study the dynamics of these processes, the imaging times must be substantially shorter. A respiration cycle is in the range of 1-10 seconds, and the instantaneous velocity of motion organ (liver) might exceed 15mm per second. It is perhaps the fastest and most practical imaging method available, EPI, the only way which meets the needs for investigating breathing motion.

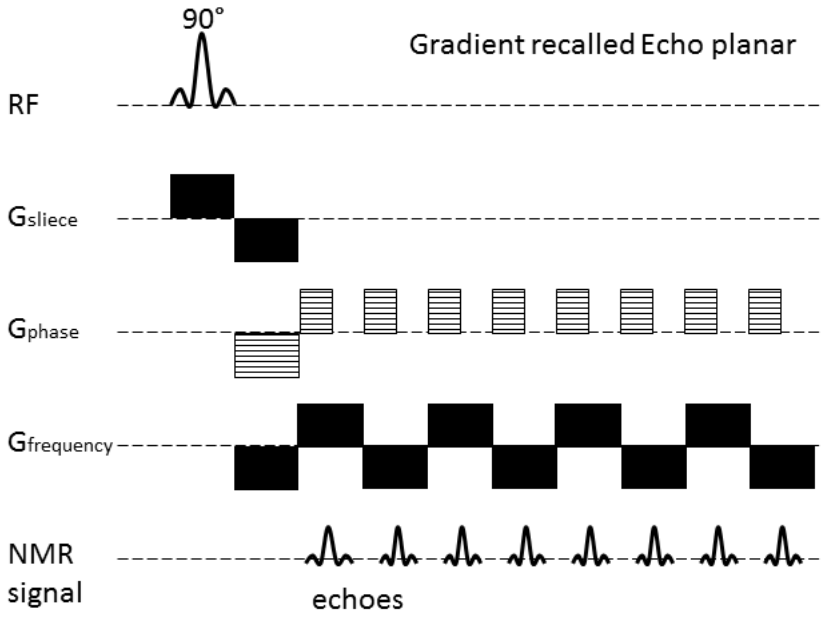

Figure 2.12 Gradient recalled echo planar pulse sequence

Figure 2.12 is a typical gradient recalled echo planar pulse sequence (Ordidge et al., 1988, Ordidge et al., 1989). It is initiated by a slice-selective radiofrequency (RF) excitation, and a rephrasing and dephasing gradient are following the RF. The frequency-encoding gradient is continuously inverted, at the same time, the phase encoding gradient is switched on and off. NMR signal sampling is performed simultaneously to acquire the multiple echos. From the pulse sequence, we know that in a TR (repetition time) cycle, the entire image is acquired, which only takes several or tens milliseconds, as long as the gradient coils can support rapid switching rates and higher gradient magnitudes (2-3 G/cm). The gradient EPI method is sensitive to chemical shift artefact and magnetic field inhomogeneities because there is not a rephrasing 180 ° RF. In the situation of severe magnetic inhomogeneties, spin EPI is more preferable than gradient recalled EPI. What is more, a trade-off between high images acquiring speed and low SNR with low spatial resolution (typically 128 ×128 or 128 ×100) of echo planar images has to be made.

Visualization of FUS-induced lesions

For MRgFUS, the MR proton resonance frequency (PRF) thermometry is a suitable method for detecting temperature rise during the focused ultrasound ablation.

For USgFUS, it is also important to monitor the ablation process to guarantee the target is completely ablated with minimal damage to surrounding healthy tissues (Cline et al., 1993). Furthermore, it is known that protein denaturation due to hyperthermia causes irreversible elasticity changes in soft tissues (Lepetit and Culioli, 1994).

Elastography assessment for FUS, which can estimate the elasticity changes inside the tissues, is a relatively new concept in comparison to other modalities such as B-mode ultrasound and MRI.

The ultrasound elastography techniques based on the same principle. A stress is generated in the tissue and then an imaging technique is used to map the tissue response to this stress in every point of the image. There are two categories of ultrasound elastography techniques, one is strain elastography and the other is shear wave elastography.

Strain elastography was initially introduced by Hitachi, and later on Siemens, in the early 2000s. The basic principle used is the one proposed by Ophir's group in the early 1990s (Ophir et al., 1991). The tissue compression (stress) is induced manually by the user. Then multiple images are recorded using conventional imaging at standard frame rates. The relative deformation (strain) is estimated using Tissue Doppler techniques. The elasticity formula is

$$E = \frac{stress}{strain}\ (kPa)$$

Since the stress is difficult to estimate at each point of the image, so the derived results are displayed as a qualitative elastic image.

Shear wave elastography is implemented in SuperSonic (SuperSonic Imagine, France). Focused ultrasound is transmitted at multiple points along a line of interest. Then an individual shear wave is generated and starts propagating around each focal point. The superposition of the individual shear waves creates a shear wave front similar to the Super Sonic Match Cone. The local elasticity can be calculated by

$$E = 3\,\rho\,c_s^2\ (kPa)$$

where ρ is the tissue density (kg/L), c_s is the speed of a shear wave propagating through the medium. Thus a quantitative elastography could be achieved (Bercoff et al., 2004).

Strain elastography has been adopted by many manufactures due to its technical maturity and ease of implementation. But it could only provide a qualitative elasticity map and the result is usually user dependent. Shear wave elastography is developed in order to fully quantify the elasticity map and get rid of user-dependence. But its utilization needs ultrafast hardware and more calculation load. So there is still a long way to go regarding elastography equipment improvements.

No known commercial product has integrated ultrasound elastography into imaging guided FUS system. Although the use of ultrasound elastography for FUS lesions has been recognized since the late 1990s (Kallel et al., 1999), only a few literatures have characterized FUS-induced lesions quantitatively using ultrasound elastography with robust image processing approach (Souchon et al., 2003, Bercoff et al., 2004). Therefore, the potential of ultrasound elastography as FUS guidance is still unclear.

Artefacts in elastography include algorithm-induced artefacts, target hardening, as well as strain concentration, which may impede the interpretation of elastograms. Threshold segmentation in ultrasound image is therefore considered to be inadequate as an estimation method for the boundary of the lesions of interest (Liu et al., 2006). Visualization of FUS-induced lesions using ultrasound elastography was later demonstrated in a preliminary study in rabbit paraspinal muscles (Righetti et al., 1999).

Quantitative comparisons between ultrasound elastography and MRI were later carried out to visualize in vivo 3D-HIFU-induced lesions (Souchon et al., 2003, Curiel et al., 2005). The study involved more than twenty patients and the results showed a correlation between ultrasound elastography and MRI, with elastogram of focused ultrasound induced lesions could be eliminated by artefacts from the mask elastography images.

There are several other ultrasound-based methods such as acoustic radiation force impulse (Fahey et al., 2005, Fahey et al., 2004) and localized harmonic motion imaging (Curiel and Hynynen, 2011) which were demonstrated to estimate the thermally induced lesions accurately but will not be discussed further in this thesis.

All these listed literatures have (either one, two or both) three large impediments in common; those are (1) the lack of assessment and discussion of important mechanical elastographic parameters such as strain rate and pre-compressive strain, (2) the lack of systematic and scientific approaches in image processing and (3) in-depth investigation of the detection of FUS-induced lesions in PAA phantom and in real tissues with respects to time and power.

2.5 Summary

This chapter starts with presenting the history and basic knowledge of focused ultrasound therapy including the generating and propagation of ultrasound, generation, transfer and dose of heat and cavitation. Section 2.2 introduces HIFU devices and typical clinical therapy courses of image guided FUS. Section 2.3 lists several key clinical applications of FUS.

Following that, the technical obstacles hindering further developments of focused ultrasound therapy for abdominal motion organs are reviewed, especially the key ingredients-image guidance (US/MRI). Some ways to address these problems are introduced, among which, the adaptive method allowing the focused ultrasound beam to follow moving tissues in abdominal organs is favourable and become the key point for this thesis.

Chapter 3 USgFUS for target motion tracking

3.1 Introduction

This chapter is mainly investigating how to use a stream of ultrasound images to track a moving target. The image processing algorithm and construction of organ motion mimicking system are the main topics in this chapter. Beginning with phantom fabrication to mimic conventional view of tumours in human liver in B-mode ultrasound, several different setups which can provide reciprocal target motion will be introduced. Based on the captured B-mode ultrasound video of the moving phantom target, a tracking algorithm was developed and tested. Next chapter will introduce the assessment of the lesion formation.

Figure 3.1 is a typical US scanning result of human liver with a hyper echoic lesion. The features in the image are different from what they look like in MR images (Figure 6 1). In MR scans, the cross-section view of blood vessels appears to be brighter than the surrounding area. These areas can be landmarks to be tracked. However, in the ultrasound B-mode scans, the cross-section view of the tumour area has a clear difference from its surrounding healthy tissues, which is usually with round shapes. The tumour is chosen to be tracked in the image processing algorithm. How to produce a similar ultrasound graphical property should be considered in the design and fabrication of the tissue mimicking phantom. It will be good if the acoustic and thermal property of the phantom is similar to the human tissue.

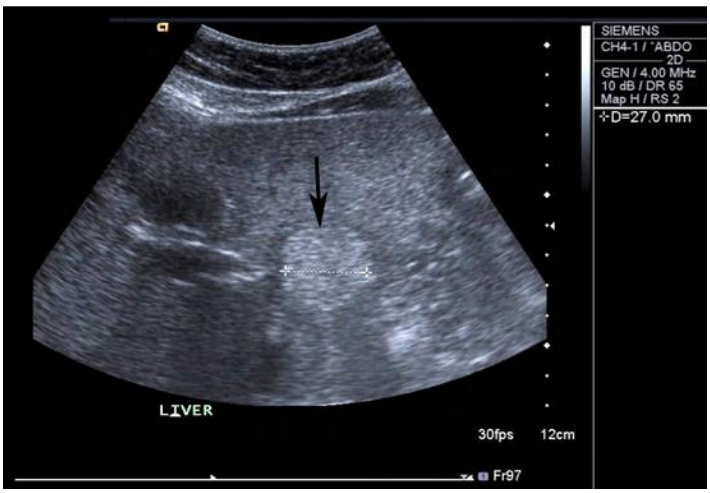

Figure 3.1 A typical human liver with tumour in US B-mode image (Meeran Naji, 2013)

3.1.1 Phantom to mimic sonographic appearance of tissue

The phantom used in this work mainly consists of these two materials, agar and PAA. The agar material is chosen to mimic the target area which will be tracked in the ultrasound images. The PAA material is chosen to be ablated by FUS ablation.

Agar phantom itself is transparent in ultrasound B-mode scans (Chmarra et al., 2013). Various additives are used to mix with agar to induce enough acoustic scattering (Cook et al., 2011). Here aluminium powder is used to be added to the agar to improve backscattering of ultrasound. The mixed solution was used to mimic the sonographic tumour inside human tissue.

Two percent agar with water mixture was stirred thoroughly until the solution appears to be homogenous and transparent in colour and consistency at about 90℃. Then the aluminium powder (0.5% w/v) was added to the solution. The solution was then cooled down and solidified for 2-3 hours in a cylindrical mold with diameter of 15mm (as shown in Figure 3.2).

Figure 3.2 Agar with aluminium powder phantom fabrication

The egg-white PAA phantom was fabricated with an optimal egg-white concentration of 30% (v/v) for visualization of HIFU exposure (Gao et al., 2012). The volume of PAA phantom was calculated according to Table 3-1.

Table 3-1: Concentration of ingredients in PAA phantom (Gao et al., 2012)

Ingredients	Concentration in phantom (v/v)
Degassed water	44.5%
Fresh egg-white	30%
PAA (40% w/v acrylamide with 2% w/v N,N-Methylene-bis-Acrylamide)	24.80%
10% w/v APS	0.50%
TEMED	0.20%

Bury the agar phantom into the mixture and then allow the PAA solution to polymerize for 10-20 minutes. As shown in Figure 3.3, in the B-mode ultrasound image (SonaSite180, FUJIFILM SonoSite, Inc., 7.5MHz ultrasound probe), the structural phantom produced a similar appearance (Figure 3.1). What is more, the material surrounding the agar area could be exposed to focused ultrasound if necessary as the colour of egg-white PAA material changes from transparent to white after exposure to FUS. This phantom model is going to be used for future tracking algorithm test.

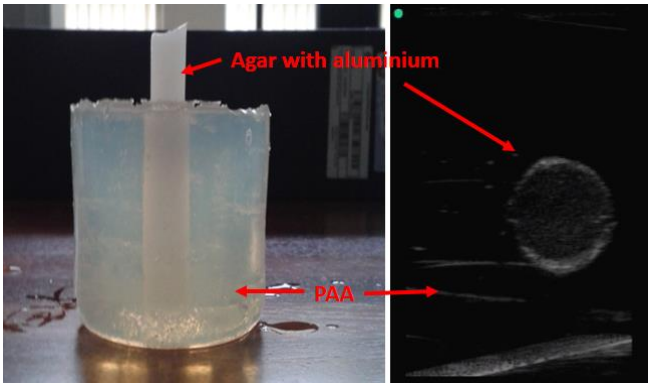

Figure 3.3 Cylindrical agar was merged into a volume of PAA phantom

3.1.2 Image processing for tracking a target in ultrasound image

The ‘tumour’ area is selected to be tracked via the image processing algorithm. The pixel intensity of the target area was not higher than all the other areas in the US image, so segmentation is not going to extract the target easily. In this study, target recognition algorithm based on contour method is favourable.

The image processing programme identifies the surrogate structure in real-time. There are two issues to be considered when developing the real-time contour extracting software.

First, in the treatment plan, the operator will select a target area roughly, then the algorithm should be able to converge to the interested area precisely. Active snake becomes the option since it theoretically can lock onto any graphical shapes from a rough contour. Kass firstly introduced this recursive process. (Kass et al., 1988). After Xu (Xu and Prince, 1998) proposed the gradient vector flow (GVF), which provides an energy field for active snakes to shrink, the active snake can converge to boundary concavities and not leak from discontinuous boundary. What is more, the GVF has made the active snake not sensitive to the contour initialization and become more robust.

Besides, fast computing speed is another requirement for tracking purpose. High computing load is a drawback of most recursive algorithms. The active snake contour is not an exception. For the ultrasound images used in this thesis, the size is 720×576 pixels, the computing time to extract the contour using GVF is over 25s, which is not acceptable for real-time application.

Fortunately, several ways have been developed to reduce the computing load of active snakes (Han et al., 2007). Multigrid-GVF (MGVF) [8] is among the most efficient methods to speed up GVF. Xu alternated the GVF with a multi-grid method, partly addressed the computing load limitation of GVF..

Via the MGVF method, the speed up performance is shown in Table 3-2. For the image with size of 720×576 pixels, the computing speed can decrease by 42 times. In this

work, the processed duration for one frame is averaged about 1.5 s. Although the performance is as good as claimed by Xu (Xu and Prince, 1998), the duration of 1.5 second is still not acceptable for real-time usage.

Table 3-2 Test for the performance of two algorithms: GVF and MGVF

Image size	Original GVF iterations	$\|\rho\|$	Computing Time (s)	MGVF iterations	$\|\rho\|$	Computing Time(s)	Speed gain
720×576	320	5.0×10^{-4}	63.20	2	4.8×10^{-5}	1.5	42

$|\rho|$: residual of two successive recursive computing, reflecting computing precision

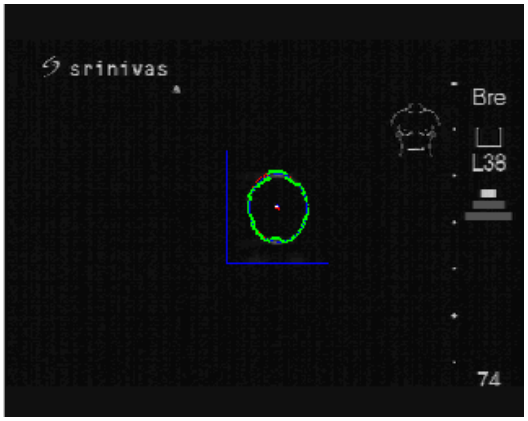

Figure 3.4 A small Region of Interest (ROI) (blue rectangle) is applied around the target area to reduce the computing load. The ultrasound image system is SonaSite180 with a 7.5MHz image probe (Sonasite, FUJIFILM SonaSite, Inc.).

Modifications have been made to decrease the computing time further. Because the computing load is highly determined by the image size and the number of iterations, reducing the image size and number of iterations can decrease the algorithm load. The displacement of the targets between two successive frames is usually smaller than four or five pixels. To reduce the number of pixels to be processed, a small ROI window which is four or five pixels larger than the target area, is selected around the current target position where the calculation is conducted (blue rectangle in Figure 3.4). This ROI window has to be guaranteed to cover the next position of the target. Using this improved algorithm, the time needed for processing one frame decreased to 0.2-0.3s,

which is about one tenth the amount of computing burden compared with MGVF method.

For the above reasons, the active snake model based on MGVF is chosen for the tracking algorithm. The whole image processing procedure is shown in Figure 3.5. The target is roughly selected at the first frame, then the algorithm can help to lock onto the target at the later frames in a video stream. The resulting contour from the current frame is used as the initialization position for the tracking recursive algorithm in the next frame. The tracked position of the target could be used to guide a medical device (HIFU) transducer to follow a moving target.

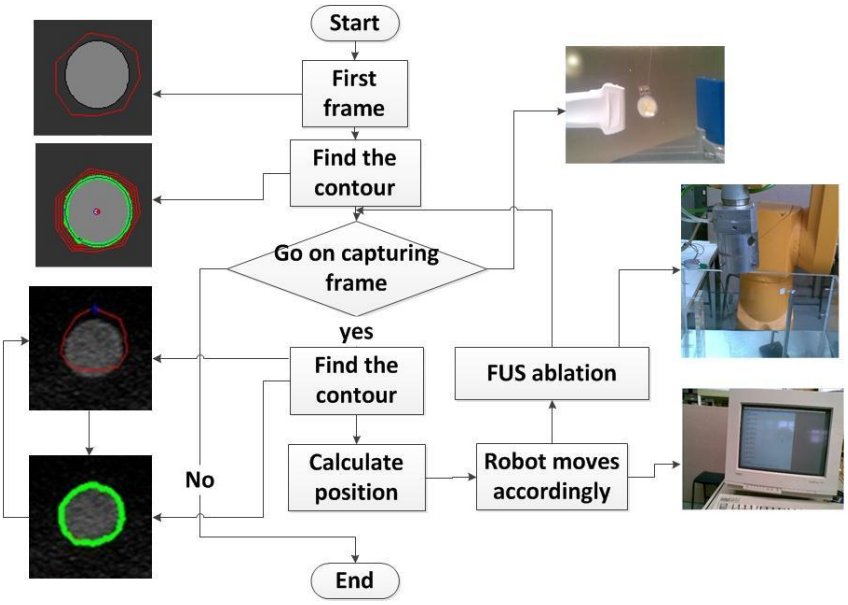

Figure 3.5 diagram of target motion tracking algorithm under ultrasound guidance

3.2 Setups to provide moving targets

The idea of setup for USgFUS is as shown in Figure 3.6. A device moves the target phantom back and forth. An ultrasound image probe captures the graphical view of the moving target. Then the target position is sent to a mechanical or electrical device which guides the HIFU transducer to let the ultrasound beam follow the moving target. In this chapter, the real sonication is not to be discussed.

In this section, several different setups which can provide a target to move back and forth will be introduced. The first one can produce a simple and slow motion along one dimension; the second one can produce a relatively complex motion along two dimensions, but still under precise control; the last one produces a similar motion trajectory which mimics the liver situation when a human is breathing freely.

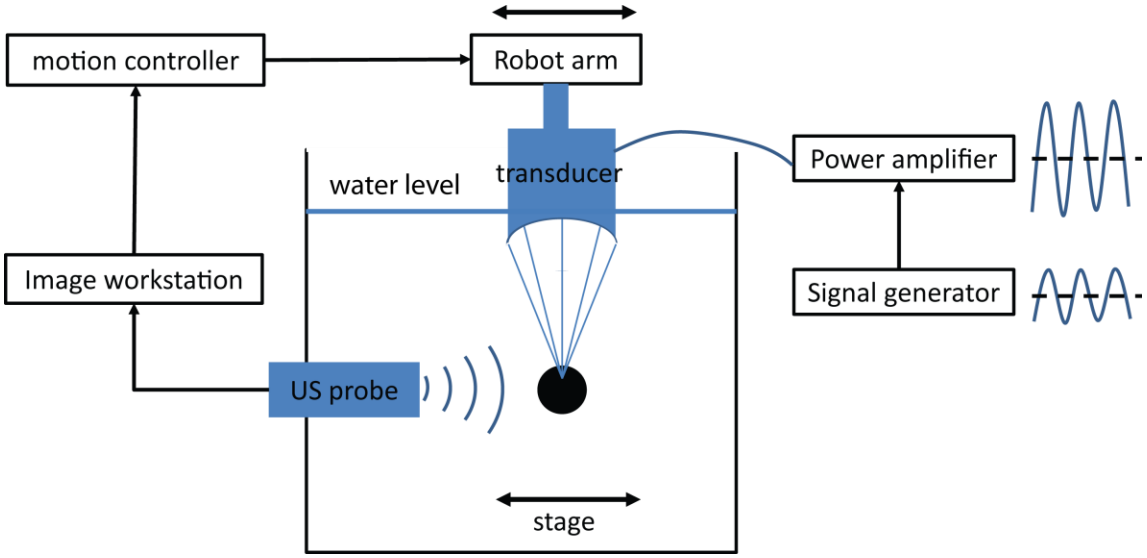

Figure 3.6 Setup of ultrasound image guided focused ultrasound ablation for motion tracking

3.2.1 One dimension slow motion, cylindrical phantom target, simple US image quality

The movement of the target is controlled by a 1D stage. As shown in the diagram (Figure 3.7), the stage can move along one axis parallel to the water plane with a speed of about 1 mm/second. This motion target is a cylindrical egg-white phantom with a diameter of 15mm. An ultrasound image machine (SonoSite 180, 7.5MHz probe) is used to capture the movement target. The image acquisition and process could be implemented in real-time or off-line. The axis of the cylindrical target is perpendicular to the US scanning plane. The cylindrical egg-white phantom and the US image probe are kept in degassed water.

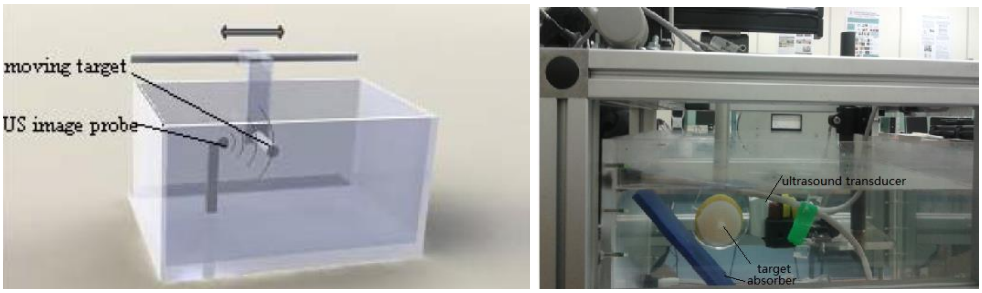

Figure 3.7 Diagram and photo of ultrasound image guided motion tracking

3.2.2 Two dimensions motion

Since the target motion caused by human breathing is in two dimensions, in order to test the tracking algorithm in 2D, a two-dimensional movement stage was designed, which is shown in Figure 3.8. The stage consists of two gear guides and two gears. A linear motor drives the bottom gear to move along one direction. This motion will be converted to a back and forward direction through a wheel gear and another gear guide. The phantom, which is mounted at the end of the second gear, can be moved simultaneously in a rotational and translational direction. The rotational movement of the phantom is restricted within ±30 ºrange.

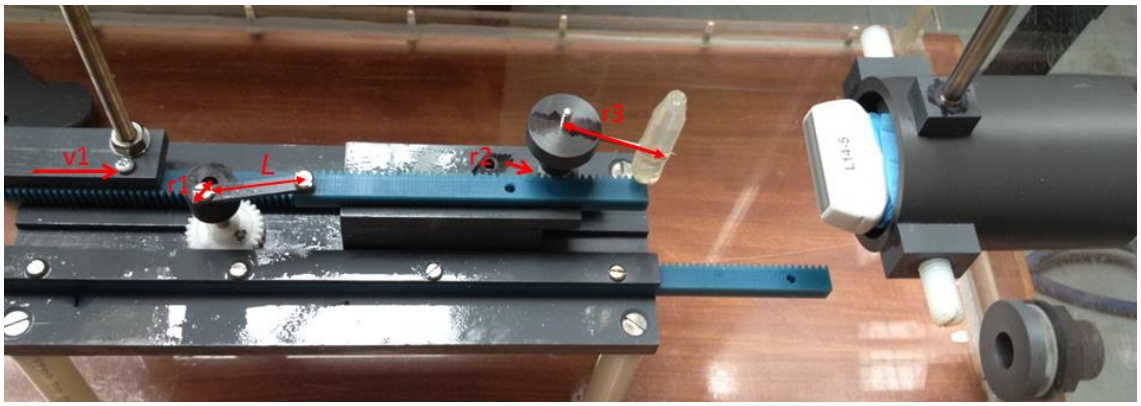

Figure 3.8 Schemetic of the 2D motion stage, the ultrasound image probe captures a cross-section of the target phantom.

As shown in Figure 3.9, the positions of target in x and y directions are as follow:

$$\begin{cases} x = S_1 + r_3 \cdot \cos((L + r_1 - r_1 \cdot \cos(S_1/r_1) - \sqrt{L^2 - (r_1 \cdot \sin(S_1/r_1))^2})/r_2) \\ y = r_3 \cdot \sin((L + r_1 - r_1 \cdot \cos(S_1/r_1) - \sqrt{L^2 - (r_1 \cdot \sin(S_1/r_1))^2})/r_2) \end{cases}$$

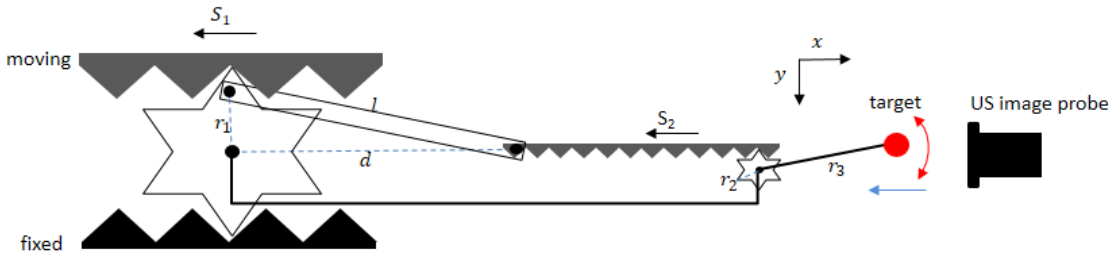

Figure 3.9 Photo of the 2D motion stage, the ultrasound image probe captures a cross-section of the target phantom.

In the design, with the dimension of r_1 (6 mm), r_2 (6 mm), r_3 (30 mm), L (38 mm), and R (6mm), a trajectory in theory was shown in the following diagram (Figure 3.10).

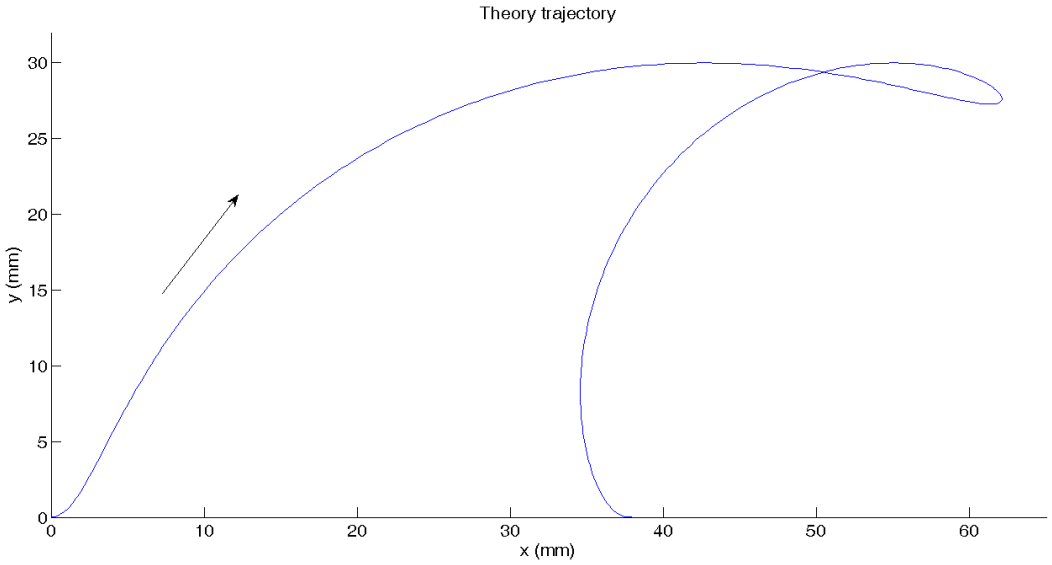

Figure 3.10 Theory trajectory of 2D motion stage. The target would repeat its motion following the diagram.

3.2.3 Breathing motion simulator

A liver motion simulator is developed to mimic respiratory motion. It can be fabricated at low cost and is also possible to be used under CT and magnetic resonance circumstances. Firstly, the principle of the simulator is illustrated in detail. Then comparisons are made between the movement generated by simulator and the motion of real human liver. There are several key features which have been considered:

1. Phantom with target inside representing the liver with tumour. A two layers phantom has been fabricated to represent human liver with tumours regarding its sonographic properties (Figure 3.3).

2. A balloon driven by the ventilator to imitate the respiratory actuator.

3. Tissue equivalent gel (water, 1.23g/L NaCl, 10g/L polyacrilic acid partial sodium salt (Sigma-Aldrich Corp., Saint Louis, Missouri, USA)) was used to mimic the fluid environment inside human body. Plexiglas® is selected as basic material because of its transparency, but other synthetic material would also be adequate.

4. A leak-proof box containing the individual components.

As Figure 3.11 shown, simulation of the respiratory motion was achieved through an inflating/deflating balloon driven by a mechanical ventilator (Julian Anaesthetic Workstation, Germany) which could control the breathing pattern. The balloon was restricted by five faces, when air was blown into the balloon, it would expand in the direction of the missing sixth face, which towards to the structural phantom. Subsequently, the balloon was in contact with the phantom and pushed the phantom forward. When the balloon deflated, the backflow of liquid would bring the phantom back, as well as the target inside. In this way, the phantom was able to move forward and backward periodically. The contact surface between the driving balloon and the phantom was not flat, so the direction of pushing force would not stay the same. Therefore, the movement of the phantom as well as the target inside were possibly moving in two directions, one main reciprocally direction and the other direction perpendicular to the first with a small displacement. The large displacement direction is considered as the superior-inferior direction. The small displacement direction is taken as the left-right direction.

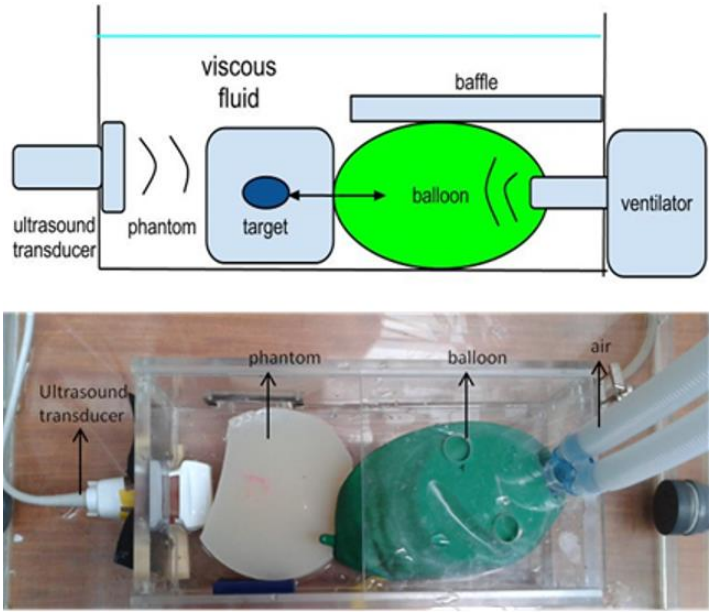

Figure 3.11 Illustration and photo of respiratory liver motion simulator

3.3 Experiment list

The experiments in this section are to evaluate the performance of the tracking algorithm including its precision and real-time feasibility. The experiment A and B is used to test the tracking accuracy in 1D and 2D respectively. Experiment C is used to characterize the breathing simulator firstly and to test the real-time performance of the tracking algorithm. In all the experiments, the ultrasound imaging system used to track the movement of the target is from SonaSite (FUJIFILM SonaSite 180PLUS®, 7.5MHz).

Experiment A: Tracking precision when the target moves in 1D

Using the setup mentioned in section 3.3.1, the target phantom was moving back and forth and its position was recorded and compared to the image tracking result. In this design, the stage did not move fast. Instead, the stage would stay still until the image processing algorithm calculated the coordinates of the target in the ultrasound image. Therefore, the precision of the tracking algorithm was tested regardless to its real-time performance. Figure 3.12 is the typical view of the same target in different positions and

how the target looks like in the ultrasound B-mode image when it moved from one position to the other.

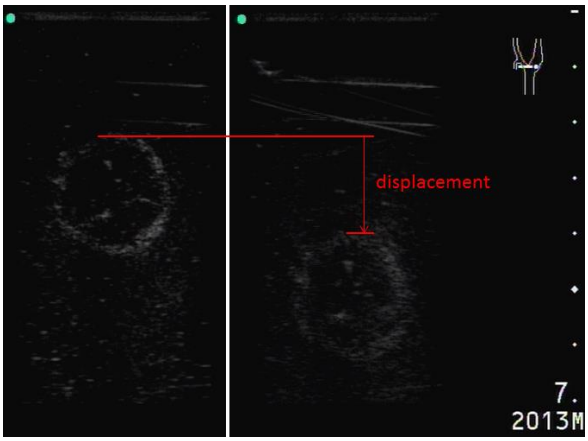

Figure 3.12 How the moved target phantom looks like in the B-mode ultrasound image

Experiment B: Tracking precision when the target moves in 2D

Using the setup mentioned in section 3.3.2, the target phantom was moving in 2D but in a controlled trajectory, its position was recorded and compared to the image tracking result. The position of the target was kept moving while the tracking programme based on image processing algorithm was running. So the dynamic performance of the image processing algorithm could be tested in this experiment.

Experiment C: Characterization of the breathing simulator and real-time performance of the tracking algorithm

The breathing simulator was characterized using the setup as shown in Figure 3.13. The phantom was driven by the balloon to move to its maximum positions (red arrow shows the main moving direction) and the ventilator would hold this position for a short period. Meanwhile, the position of the target was calculated by the tracking algorithm and a 2D stage was guided to move a laser pointer to a position above of the target. The laser pointer position was adjusted if it did not exact coincide with the position of the phantom and its position was recorded. The recorded information was an illustration of the performance of the respiratory mimicking machine.

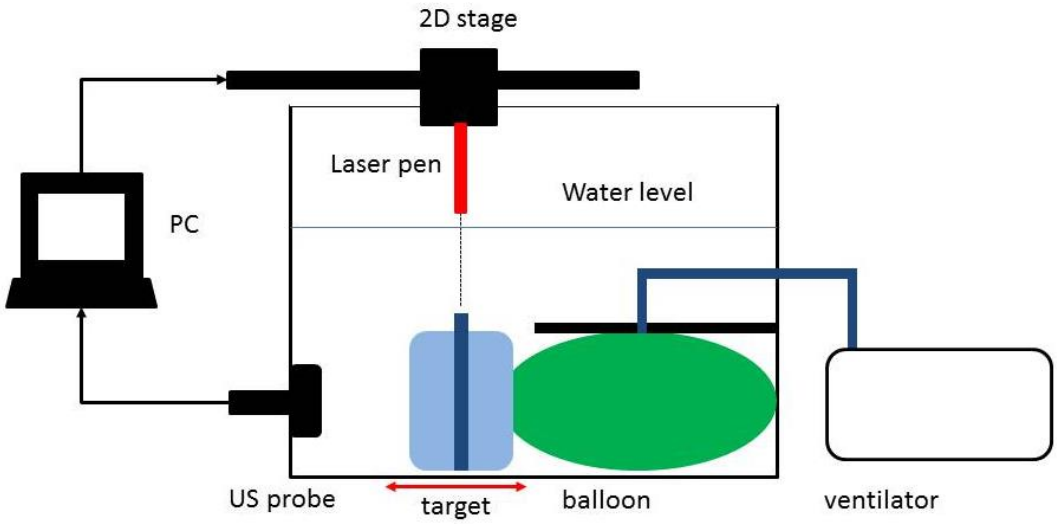

Figure 3.13 Setup for the characterization of the respiratory motion simulator. Red arrow indicates the target phantom (blue block) moves mainly at superior-inferior direction. The target phantom also has slightly displacement in left-right direction (in and out of paper).

A tracking experiment was designed based on the respiratory simulator. Since the exact position could not be controlled and recorded, only the robustness and repeatability of the tracking algorithm were evaluated.

3.4 Results and discussion

3.4.1 Tracking precision when the target moves in 1D

Based on the first setup, the precision of active tracking method was investigated without regarding its real-time performance. In Figure 3.14, the measured positions from the active tracking algorithm were compared to the corresponding recorded positions from the stage. As the figure shown, the error between them did not exceed 2 mm.

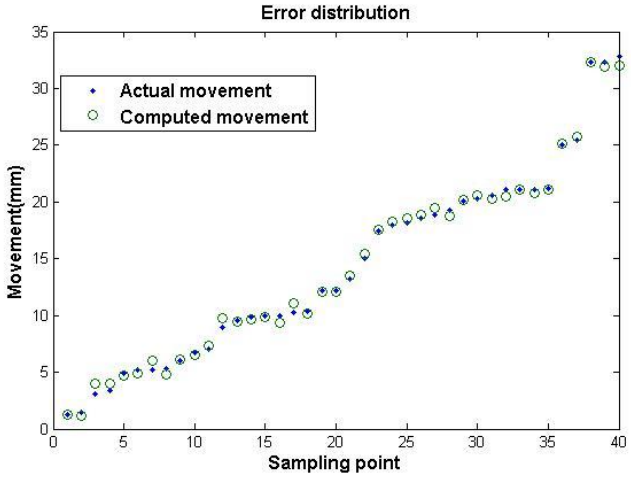

Figure 3.14 Precision of active tracking of static situation

In the repetition test, the target phantom stays still at one position, but the tracking programme was executed for 170 times. As shown in Figure 3.15a, all the repetition tracking results of the same position were distributed in a narrow area of about 0.35 mm by 0.35mm. Their distances from the averaged value (marked '+' in Figure 3.15a) were shown in the histogram (Figure 3.15b). Most of the distance errors were smaller than 0.15mm.

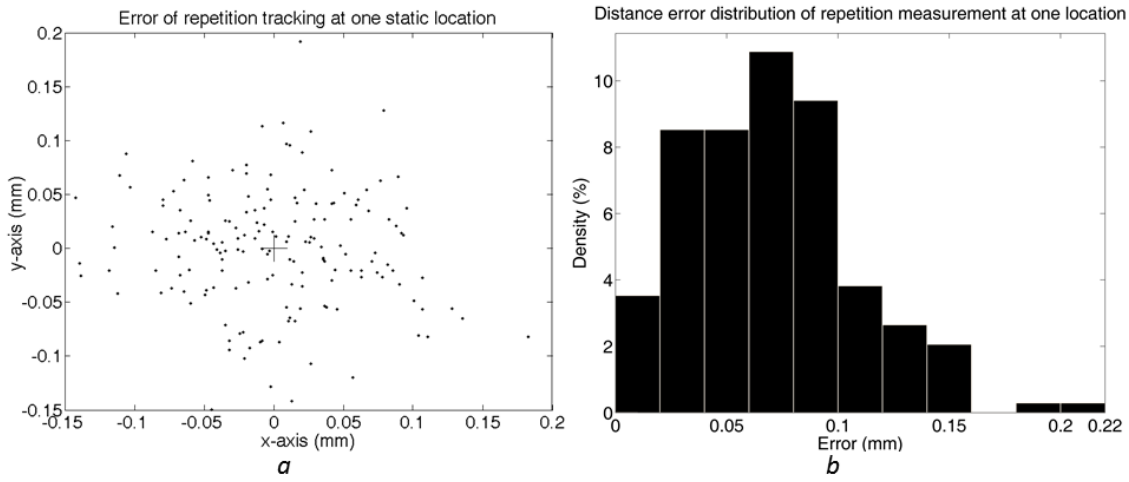

Figure 3.15 Repetition of tracking result at a static position (a) Error distribution in x and y dimensions, their average value was marked '+' in the image (b) Distance error distribution histogram of the repetition tracking.

Therefore, the performance of the image processing algorithm for displacement measurement of slow motion speed or no motion was with a precision of less than 2 mm, and its computation robustness is within the range of 0.22 mm. Compared to the size of the section plane of the target phantom (15 mm), the accuracy and repetition were acceptable. The relatively large precision error (2 mm) might come from the misalignment of the target motion trajectory and the ultrasound image plane, which means, there was a bit of out-of-plane motion during the tracking programme execution. Since ultrasound scanning is a user dependent modality, this systematic error is unavoidable.

3.4.2 Tracking precision in 2D

Based on the second setup, the target phantom was driven to move in a relatively complex 2D trajectory. An example trajectory of two cycle motion was shown as in Figure 3.16.

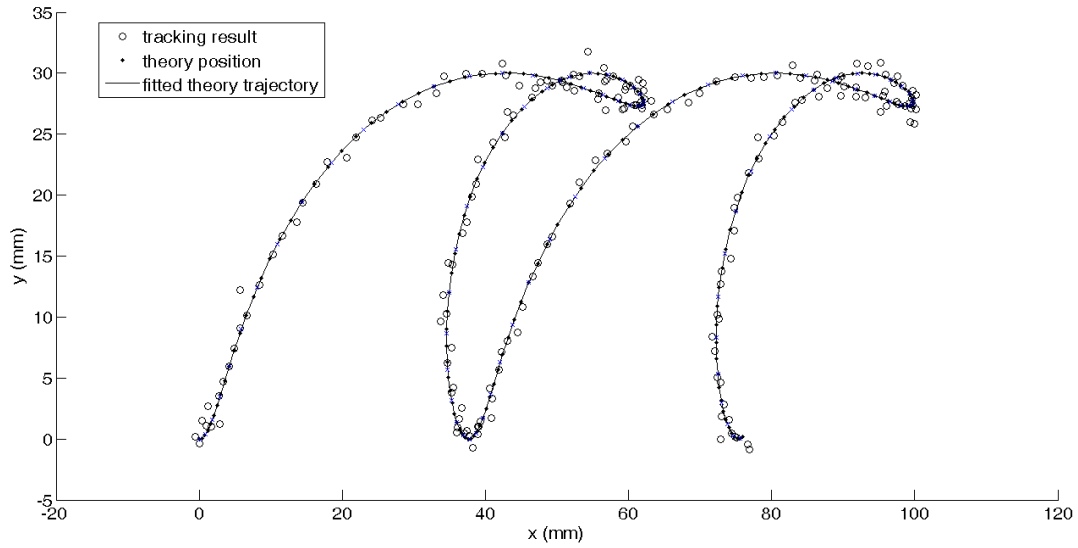

Figure 3.16 2D controlled target phantom motion trajectory and tracking result

The tracking accuracy at each measured point was determined by comparing the tracked positions $\vec{r}_m$ with the theoretical positions $\vec{r}_r$ provided by the stage on a point-by-point basis as $|\vec{\epsilon}_i| = |\vec{r}_{r_i} - \vec{r}_{m_i}|$ (Andrew et al., 2004). The distance error distribution for tracked target phantom was plotted as a frequency histogram (Figure 3.17).

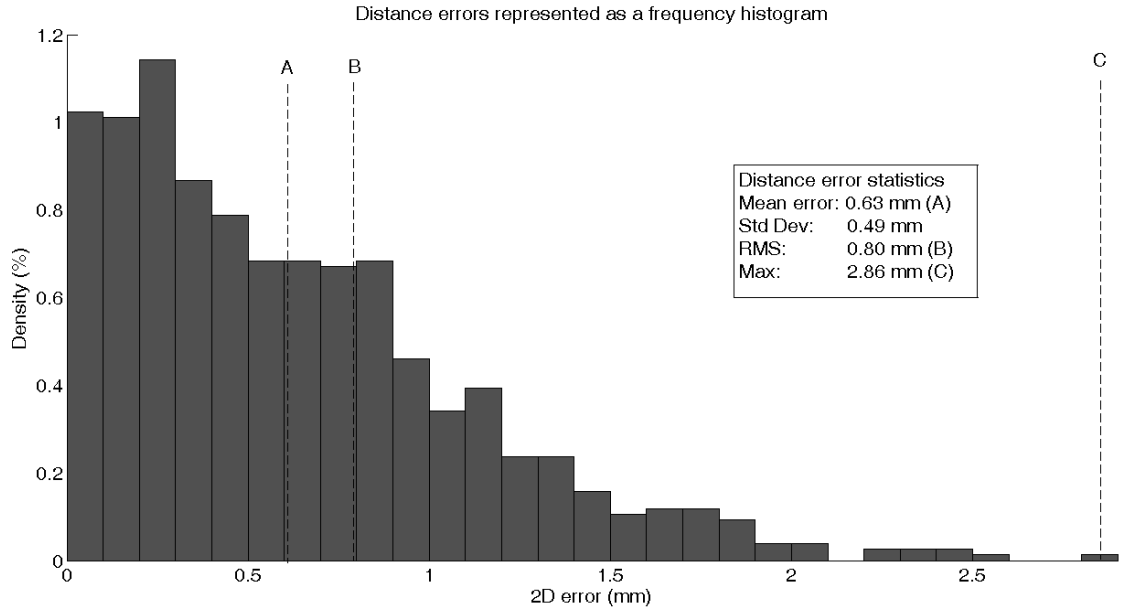

Figure 3.17 2D distance tracking errors represented as a frequency histogram. The error statistics was labelled in the histogram.

In the measurement range, the overall RMS (root-mean-square) 2D distance error is 0.80 mm (labelled B in Figure 3.17). Most of the errors lie within twice the actual RMS, with the maximum error (labelled D) being an order of magnitude greater than the RMS. The mean error and standard deviation are computed as well (labelled A). However they are not preferable for the data interpretation since all the errors were positive so the distribution is clearly not normal which skewed heavily to higher errors.

The maximum error (2.8 mm) and the algorithm robustness (RMS, 0.80 mm) in 2D are both larger than the ones (2.0 mm and 0.22 mm) in 1D because the 2D motion might involve more systematic errors such as the system complexity. Considering the 2D motion system is much more complex than the 1D motion stage, especially the theoretical position of the target is computed through such a complex relation (Figure 3.20), the tracking precision is acceptable.

3.4.3 Respiratory device performance and the tracking repetition

Performance of the liver motion simulator

As shown in Figure 3.18, the motion range of a target phantom was roughly restricted in a rectangle area, Table 3-3 summarized the comparison between the movement generated by simulator and the motion of human liver.

Figure 3.18 Diagram of a target motion range driven by the respiratory mimicking machine

At the superior-inferior (SI) direction, the simulator could provide enough motion range like real human liver, at the left-right (LR) direction, the range provided is also comparable to the real situation. Since there is no space allowable at the anterior-posterior (AP) direction for the simulator, the motion range at this direction have not been measured . The motion cycles and the motion speed of the simulator are controllable so the simulator can mimic different liver motion speed caused by breath under different patient situations. And this device is reusable for future experiments which need a simulated motion tissue mimicking phantom.

Table 3-3: Comparison between the motion of simulator and liver (Park et al., 2012), SI, LR: left-right, AP: anterior-posterior

	SI (mm)	LR (mm)	AP (mm)	Cycle (second)
Human Liver	17.9±5.1	3.0±2.0	5.1±3.1	3.9±0.7
Simulator	Up to 20	2	unknown	3 to 7

Tracking experiment

In the ultrasound image series, the target was tracked when it was driven to move by the respiratory setup. As shown in Figure 3.19, in each frame, the target was locked by a contour (green), and its weighted centre was computed according to a fitted ellipse (blue).

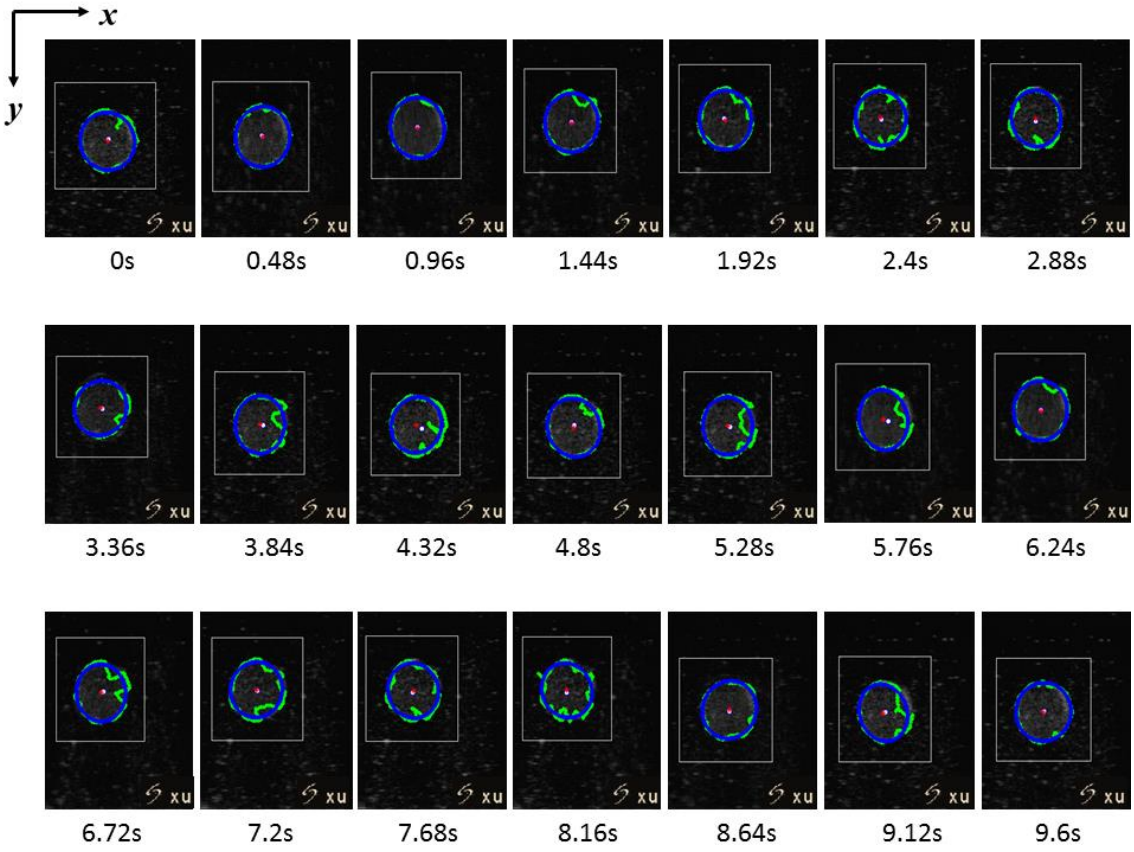

Figure 3.19: Demonstration of the performance of the target tracking programme on a series of video of real-time moving target driven by respiratory machine. Results with obvious displacements between two frames are shown. The green line represents the calculated contours surrounding the target; the blue ellipse is fitted from the contour points; the rectangle window restricted a ROI for each frame to reduce the computation load.

The tracked position of the targets in two perpendicular directions for the series was recorded (Figure 3.20). As mentioned in the previous characterization of the respiratory setup, the displacement of the target was mainly along one direction (about 5 mm in y

axis for this frame set), leaving the other direction subtle fluctuations (about 1 mm in x axis). If the displacement in y direction increased, which means the 'inhale' gas volume was improved via adjusting the ventilating machine, the displacement in x direction would increase, as well. As shown in the figure, the recorded motion is more like a cycle motion.

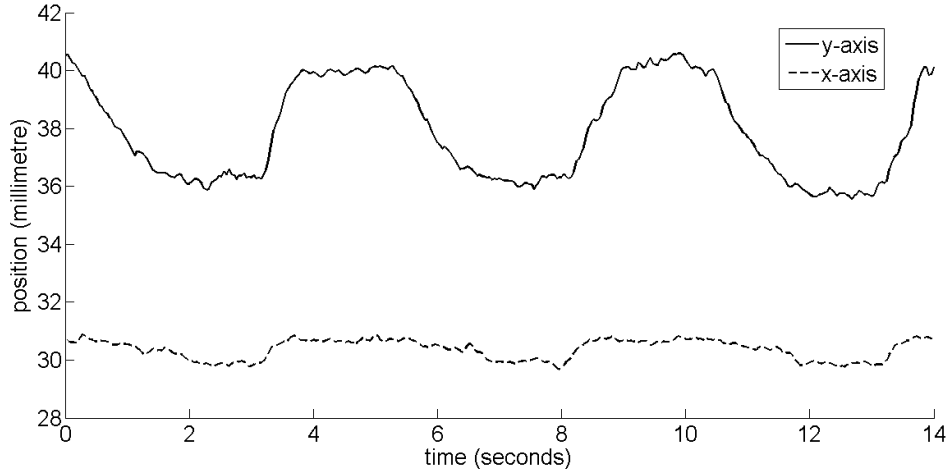

Figure 3.20 Tracking result of target motion triggered by respiratory machine

Tracking performance

However, unlike the previous two experimental setups, there was not a reference measuring method to assess the tracking precision when using the respiratory machine to drive the target to move. Therefore, only the repeatability of the tracking results were evaluated, which was used as an indirect pointer of the performance of the tracking programme. The displacements in y direction were adjusted to close to 18 mm and 5 mm respectively. These values are similar to the human liver displacements (Park et al., 2012) in SI and AP directions mentioned in Table 3-3. The cycles of the target motion were also adjusted via the ventilating machine.

Two parameters were used to evaluate the repetition of the tracking programme in this experiment. The first one is the correlation coefficients ρ between the displacements in two cycles. The correlation coefficients value is between -1 and 1, 0 means two data series are not related to each other at all, ±1 means two data series are highly dependent on each other.

Assuming the tracked position series in the first cycle is ($D_x(t)$, $D_y(t)$), $0 \leq t < T$, the series in the second cycle is ($S_x(t)$, $S_y(t)$), $T \leq t < 2T$, x and y represents x and y displacement directions. The correlation coefficients ρ in the x and y directions are expressed as

$$\rho(D_x, S_x) = \frac{cov\big(D_x(t), S_x(t)\big)}{\sigma_{D_x}\sigma_{S_x}} = \frac{E\big[\big(D_x(t) - \mu_{D_x}\big)\big(S_x(t) - \mu_{S_x}\big)\big]}{\sigma_{D_x}\sigma_{S_x}}$$

$$\rho(D_y, S_y) = \frac{cov(D_y(t), S_y(t))}{\sigma_{D_y}\sigma_{S_y}} = \frac{E[(D_y(t) - \mu_{D_y})(S_y(t) - \mu_{S_y})]}{\sigma_{D_y}\sigma_{S_y}}$$

where *cov* is the covariance, E is the expected value operator, μ is the expected value of respective data series, σ is the standard deviation of respective data series.

The correlation coefficients ρ with an absolute value close to one in this work represents the data in two cycles are with highly similarity to each other. That means the displacement in the respective direction happens at similar time point in a cycle. If the correlation coefficients with an absolute value which is much less than 1, the data in two cycles tend to be mismatched to each other in time series. Since the ventilation machine was providing a stable motion, theoretically displacements between two cycles should be of high similarity. Two example data series were shown in Figure 3.21, they are compared in one diagram, the correlation coefficients between the two data series is about 0.83, which indicates that the two series seem to have different time cycle.

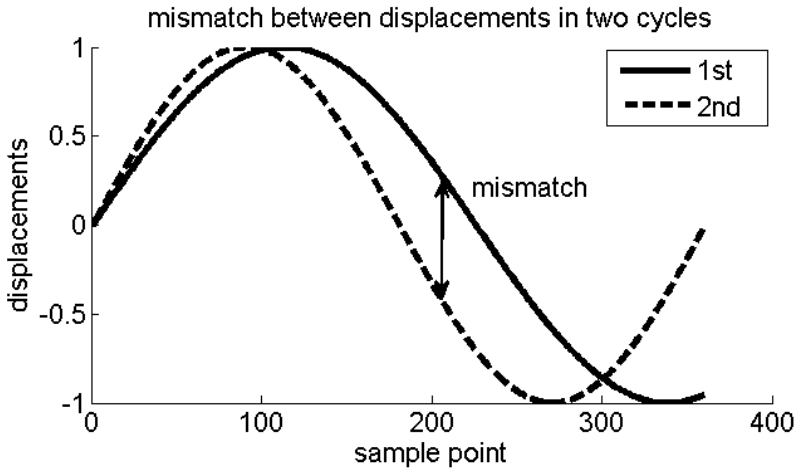

Figure 3.21 Diagram of mismatch between displacements in two example cycles. The correlation coefficient between the two series is about 0.83. The smaller value is because the two series seem to have different time period.

Another parameter which is the residence between the displacements series in two cycles, are expressed as

$$Res_x = sqrt(\sum_{t=0}^{T}(D_x(t) - S_x(t))^2)$$

$$Res_y = sqrt(\sum_{t=0}^{T}(D_y(t) - S_y(t))^2)$$

in which, Res_x and Res_y are the sum of the squares of the differences between pairs of points at the same time in two different time periods. $D_x(t)$, $S_x(t)$, $D_y(t)$, $S_y(t)$ are the displacements series in two directions in two time periods, $D_x(t)$-$S_x(t)$ and $D_y(t)$-$S_y(t)$ are the mismatches indicated in Figure 3.21. This parameter is an indicator of the absolute differences between two cycles.

The two parameters were tested within two different displacement ranges, 5 cm and 10 cm. The target was moved back and forth for at least three cycles in each range. The correlation coefficients and the $Res_{x,y}$ were calculated between any two successive time periods. Table 3-4 summarized the results. Firstly, the correlation coefficients in *y* direction were larger than in *x* direction, which was because that the target movements in *y* direction was under the control of a ventilation machine and the movements in *x* direction was unpredictable. Secondly, the Res_x was smaller than Res_y , which is because that the displacement range in *y* direction were larger than in the displacement range in *x* direction, which resulted in a larger fluctuations between two periods. And the correlation coefficients in both directions decreased a little as the displacement ranges increasing, while the $Res_{x,y}$ increased as the displacement ranges increasing.

Because we assumed that the breathing machine guided the target motion in a highly repetition mode, the large correlation coefficients between two time periods and small $Res_{x,y}$ indicated indirectly that the tracking algorithms had a highly repetition property, which means the algorithms is with a good computation robust and could be used to monitor target movements with long time periods.

Table 3-4 Repetition results when target was moved in a range of 5 cm and 18 cm. $\rho(D_{x,y}, S_{x,y})$ was the maximum correlation coefficient between two successive time periods, $Res_{x,y}$ was the maximum displacements residents between two successive time periods. The target was tracked by the programme for at least three movement cycles.

Displacement range (cm) in y direction	$\rho(D_x, S_x)$	$\rho(D_y, S_y)$	Res_x (cm)	Res_y (cm)
5 cm	78%	96%	2.5	5.2
18 cm	75%	95%	3.5	6.0

3.5 Summary

This chapter used stream of ultrasound B-mode images to track moving targets. For realizing that, moving phantoms were fabricated and a target tracking algorithm was developed.

A two-layered tissue mimicking phantom was fabricated with agar and PAA material which, in ultrasound B-mode scan, had similar graphic view to human liver with tumours. The agar material looks like a spherical tumour and the PAA material looks like normal tissue in ultrasound B-mode scan. Besides that, the PAA material could also react to HIFU exposure.

Based on the phantom, three different setups were built to produce various movement which were used later to test tracking algorithm. The first two setups can move the

target phantom in highly controlled modes. The first setup provides a linear movement and the second provides a 2D cycling movement. The third setup is a respiratory simulator which mimics the motion pattern of human livers when the patient is freely breathing. Its performance was characterized. The motion range, speed and cycle at SI and LR directions of the phantom in the device were found to be comparable to human livers.

An active snake contour tracking method was realized to segment the featured target in ultrasound B-mode frame stream. This method theoretically can cope with various target shapes yet not tested in this chapter. With this tracking algorithm, the spherical target in ultrasound B-mode images could be tracked with a frame rate higher than five frames per second. Extracted coordinates were used to analyse the regular moving pattern of the target in the experiments, in which the phantom was moved in different paths with the above setups. The RMS error of the tracking was smaller than 0.80 mm, which indicated that the tracking algorithm can provide an accuracy of sub-millimetre.

This tracking algorithm together with the simulation setup of respiratory motion could be used as an *ex vivo* test of USgFUS for motion tracking before *in vivo* experiment.

In this chapter, the issue of motion tracking in 2D with ultrasound B-mode has been solved. The HIFU sonication on the tissue has not been conducted in this chapter mainly because of highly interference of focused ultrasound on the diagnostic ultrasound image quality. This problem could be solved in an interleaved method in which the diagnostic ultrasound and therapy ultrasound are switched on in different time. The FUS lesion formation assessment is another issue to be considered. The next chapter will discuss the possibility of using strain sonoelastography to detect and assess lesions formation in both phantoms and fresh tissues.

Chapter 4 Lesion monitoring and assessment during USgFUS

The objectives of this part of work are (1) to derive a method using ultrasound elastography that can detect and characterize FUS-induced lesions, (2) to assess how FUS-induced lesions differ from different samples, power and duration of FUS sonication under ultrasound elastography.

4.1 Materials and methods

The experiment setup, studied samples, and image processing methods are described in this section, all server to achieve the goal of capturing the FUS-induced lesions within the ultrasound elastography image.

4.1.1 Experiment setup

The ultrasound image system used is a SonixTABLET (Ultrasonix, British Columbia, Canada) which has a 128 linear element transducer and a research licenced software. Operating frequency at 10 MHz was chosen for the elastography acquisition.

Elastograms acquired from the SonixTABLET were saved in ".png" file extension. The images are saved in a pseudo-colour format (Figure 4.1), which is based on a fluid-jet simulation by National Centre for Supercomputer Application. The soft regions are represented by a blue colour, then to green, cyan and red represents stiff regions.

Figure 4.1 Blue colour represents soft regions and red colour represents hard regions in the elastogram images from SonixTABLET.

A single-element HIFU physiotherapy transducer (Precision Acoustics, Drochester, UK) is used with a diameter of 60 mm and a central frequency of 1 MHz (Figure 4.2). This transducer is operated in continuous mode at a 1.6 W/cm^2 spatial average temporal peak intensity. Total acoustic output power was measured using a radiation force balance-

fitted with an absorbing acoustic target and with a 60 mm water path between the transducer face and the surface of the target. The peak negative acoustic pressure was measured at a distance of 65 mm (focal length of the transducer) from the face of the transducer using needle hydrophone. The values measured were as follows: peak-peak input voltage 5 V, peak negative acoustic pressure at 65 mm from the transducer was 0.63 MPa (ter Haar et al., 2011).

In the experiments, the FUS transducer is set to operate with electrical power output from 30W to 70 W. The attenuation is negligible and that the -6 dB beam dimension is ~2 mm (Cline et al., 1993).

The challenge in experiments is to keep a relative positioning of FUS transducer and ultrasound imaging probe. Ultrasound image probe is aligned such that its imaging plane coincides with the direction of the FUS beam axis. So the focus of the HIFU transducer is covered in the image plane to guarantee the lesion is observable. Figure 4.2 illustrates the proposals and how alignment is done.

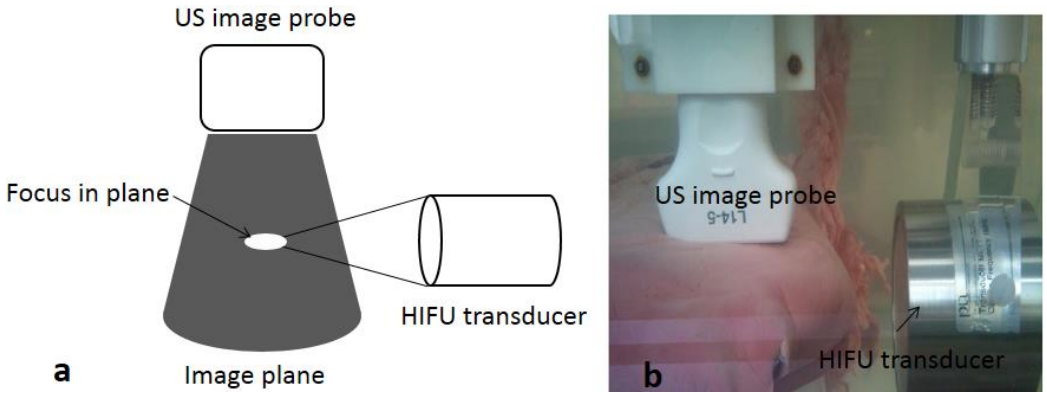

Figure 4.2 Diagram and photo of the mounting units of the ultrasound image probe and the HIFU transducer, the HIFU transducer mounting unit is facing perpendicular to the imaging plane of the ultrasound scanner. a) diagram of the alignment of the image probe and HIFU transducer; b) photo of the alignment of the image probe and HIFU transducer regarding to observing lesions in sheep liver

4.1.2 Samples

There are two types of samples used in this study, for a feasibility study of the use of ultrasound elastography in assessing FUS-induced lesions:

Egg-white PAA phantom

Egg-white PAA phantom is one of the most widely used HIFU phantom. Although FUS-induced lesions within egg-white PAA phantom can be detected under naked eyes, this approach was observed to be unreliable when exposed to FUS at therapeutic power. The induced lesions are highly probabilistic, which means that there is a chance for the egg-white within the PAA phantom to be fully denatured, but not shown under naked eyes. Using elastography to assess the lesions in PAA phantoms is worth to test.

Fresh sheep liver

Liver is a representative organ in the abdominal. In this work, fresh sheep livers are chosen for investigation. The biological tissues are often opaque and usually do not show differences in ultrasound B-mode scan after exposed to the FUS. The disadvantages of this method are relatively less accurate and inflexible which means careful planning is required. So the elastography method is worth a try to detect the lesions in the fresh animal tissues.

4.1.3 Segmentation algorithm

This section describes the procedures developed to segment a lesion area from sonoelastography images. Figure 4.3 shows the flow chart of the segmentation algorithm (MATLAB2012, MathWorks), where elastography images obtained from 50 samples of homogeneous PAA phantom was studied together to find an acceptable threshold level to identify the lesion. All samples here were exposed to focused ultrasound with electric power of 30W for 40 seconds. Firstly the sample images were to convert to 8-bit grey intensity from colour intensity. After that, a statistical analysis of all the sample images between the lesion area and the background area was done to find a general threshold level for segmentation. Based on the threshold level, the

expected interested lesion area was selected. Then in the original images, the interested area were differentiated into several sub-levels via pixel intensity (low intensity-soft, high intensity-hard).

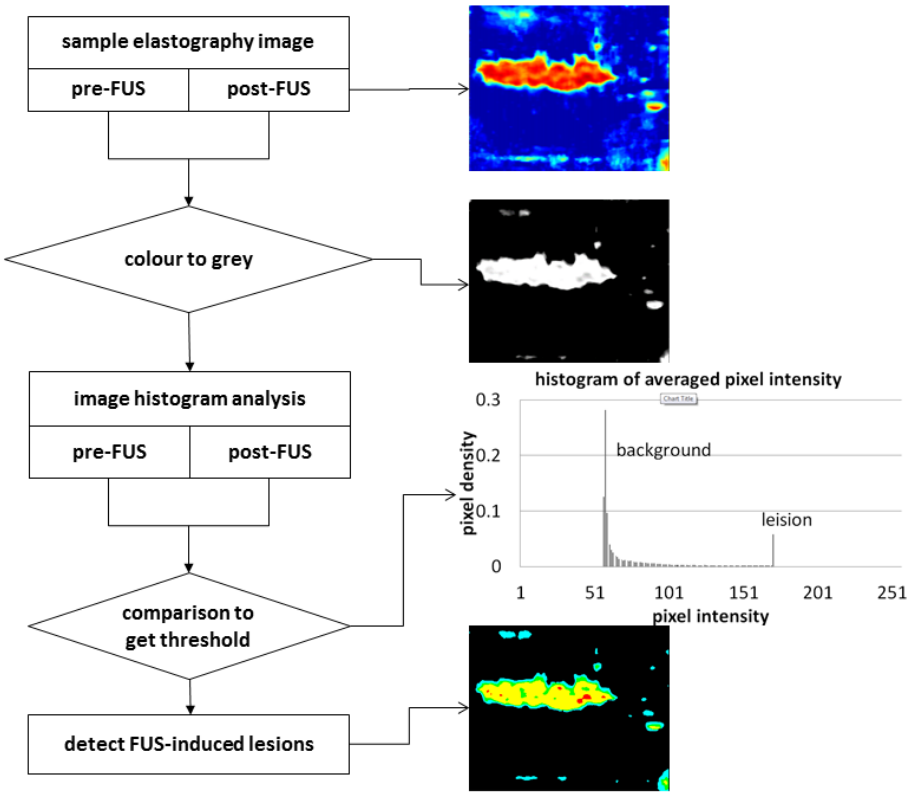

Figure 4.3 Flow chart of the threshold segmentation for FUS lesion detection in strain sonoelastography images.

To convert images from a pseudo-colour scale to a grey scale, a correlated colour map was selected based on colour intensity relationship as shown in Figure 4.4. As the cold colours (blue, purple) represent more to soft region in the images, they contribute more to a dark area after converted. The warm colours (yellow, red) contribute more to the bright area after converted. In the converted grey scale image, high intensity pixels (bright) represent hard area and low intensity pixels (dark) represent soft area.

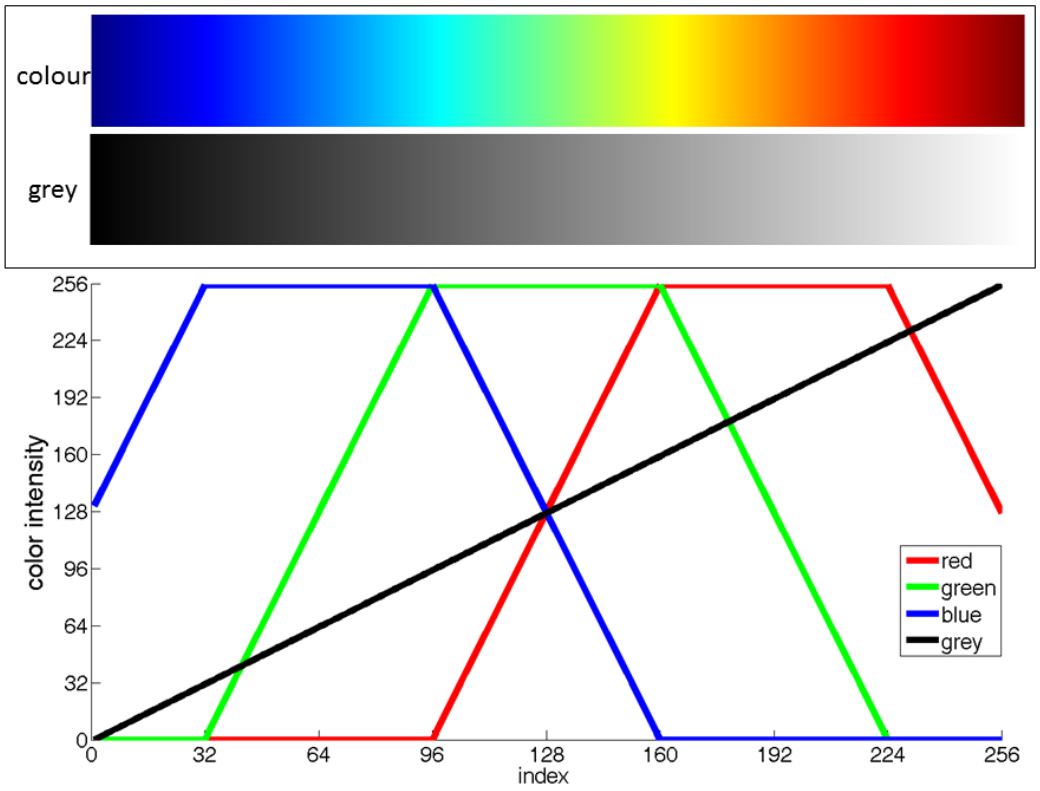

Figure 4.4 Pseudo-colour (red, green, and blue) and Grey (8-bit) colour map and the conversion between them, the strain elastography was shown in colour map (red-hard, blue-soft), the stiffness represented by different colours was converted to a linear grey representation (bright-hard, dark-soft).

Based on a statistical analysis, the threshold level of 168 was selected for this series of elastography images. After removing the background from the elastography images based on the threshold level selected, the interested lesion area in the original image was separated to several different colours, green, yellow and red, representing different stiffness from soft to hard respectively.

Because the elastography scan in fresh animal liver is similar to PAA phantom, the histogram and statistical analysis could be extended to be used to identify FUS lesions in fresh animal liver tissues. The only difference for different materials is different threshold level.

4.2 Verifying elastography for lesions detection

In this section, the results are categorised in three main studies. The first study is about image processing, 3D-reconstruction and volume measurement of pre-heated egg-white PAA lesions. The second study investigates FUS-induced lesions and its characteristics with respect to ultrasound power and duration in egg-white PAA phantom. The findings of the second study will enable the comparisons with the findings in *ex vivo* animal sheep liver regarding FUS-induced lesions. In the third study, elastograms of FUS-induced lesions will be studied for the possibility of using threshold-based segmentation to distinguish lesions at different FUS power and duration.

4.2.1 Experiment list

Egg-white PAA phantoms are able to keep up with biological soft tissues in FUS experiments because they are easy to handle and sterilise, and that they offer studies to be performed in a highly controlled fashion. In addition, they have similar acoustic properties such as attenuation and thermal diffusivity to soft tissues(Takegami et al., 2004). The following first three experiments are all conducted on egg-white PAA phantoms.

Cubic pre-heated egg-white PAA lesion

In confirming the elasticity changes and the effects of pre-compressive strain at therapeutic FUS power, egg-white PAA phantom was sliced into small cube with volume of 0.14 cm3. These cubes were immersed in a heated bath at 60 ℃ for 5 minutes and then embedded into another egg-white PAA phantom (Figure 4.5a). Twenty-five slides of elastograms with step (lateral distance between slides) of 0.25 mm were acquired. Ultrasound elastography was set to operate at 10 MHz, strain rate of 1 mm/s. Each elastography acquisition was repeated three times for each sample, and three samples were scanned in total. All the elastograms were then processed using image conversion, histogram and statistical analysis as discussed previously. Threshold value for image segmentation was then determined.

3D-reconstruction was employed to visualize the segmented lesions and to evaluate their volumes. Different pre-compressive strains were also investigated for the effect on 3D-reconstruction. The pre-compressive strains were chosen to be around 7-14% (Ophir, Alam et al. 1999) as the optimum range for elastographic signal to noise ratio (SNRe).

Spherical pre-heated egg-white PAA lesion

The second experiment involved lesions of spherical pre-heated egg-white PAA phantom (5 mm in radius). The procedures for this experiment were identical to the first experiment with cubic pre-heated egg-white PAA lesions. Immersion in heated bath at 60 ℃, 0.2 mm scanning slide step, 5% pre-compressive strain and 1 mm/s strain rate were carried out (Figure 4.5b).

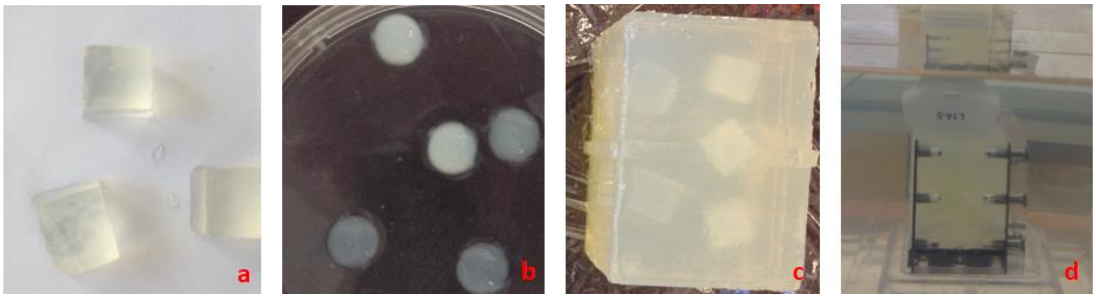

Figure 4.5 Pre-heated egg-white PAA lesion (a) cubic lesion (b) spherical lesion, white phantom lesion were taken out from hot water bath, transparent ones were not processed by hot water (c) cubic shaped small pieces target in PAA phantom (d) elastography scan on the phantom which contains small pieces target

FUS-induced lesions in egg-white PAA phantom under ultrasound elastography

Once the segmentation method had been proposed and verified, FUS-induced lesions in egg-white PAA phantom were investigated with FUS at 70 W electrical powers for 15 to 40 seconds. Cross-section area of the FUS-induced lesions (N = 10 for each duration of ultrasound exposure) under ultrasound elastography were captured and segmented. Quantitative analyses were performed to verify the hypothesis that ultrasound elastography can detect FUS-induced lesions before visual coagulation (white coagulation of egg-white PAA phantom in naked eyes and white bubble area in B-mode

ultrasound image) start to occur. The process of lesion formation under strain sonoelastography has also studied.

Elastography of FUS-induced lesions in fresh sheep liver

The process of FUS-inducing lesions on real tissue is often complex and conventional acoustic parameters rarely succeed in predicting and explaining the outcomes.

In studying the elastographic changes of the pre- and post-HIFU on fresh tissues, a method for detection of FUS-induced lesions was derived based on fresh sheep livers. The effects of ultrasound power and duration on elastographic lesions were also investigated (Figure 4.2b). Acquired data set from fresh sheep liver was then compared with data set from egg-white PAA phantom to investigate the possibility of replacing soft tissues by egg-white PAA phantom, regarding elastography guided FUS study.

4.2.2 Results and discussions

4.2.2.1 Elastography of pre-heated egg-white PAA phantom

Cubic pre-heated egg-white PAA phantom

Threshold in 8-bit greyscale intensity for this experiment was chosen as following: red from 228 to 255, yellow 200 to 228, green 180 to 200 and cyan from 160 to 180. The segmented image was followed by morphological opening to remove noise based on cumulative pixel density (not mentioned in the image processing flow chart, Figure 4.6).

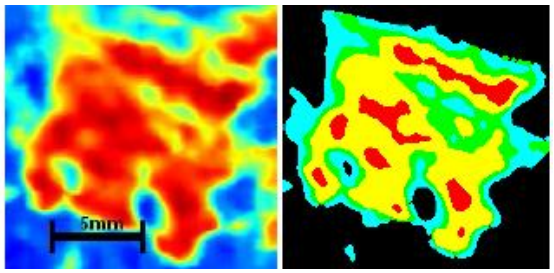

Figure 4.6 Elastography image of the cubic pre-heated lesion (left) and its segmented image (right)

Twenty slides of elastograms with slide step of 0.25 mm were processed in different pre-axial compressive strains followed by 3D-reconstruction. An example of 3D-reconstruction for the 0.14 cm^3 pre-heated egg-white phantoms after segmentation is shown in Figure 4.7. The minimum and maximum values in 3D-reconstruction and volume measurement were obtained from repeated measurements. Table 4-1summarises the results of volume measurement of the 0.14 cm^3 pre-heated egg-white PAA phantom in different pre-axial compressive strains.

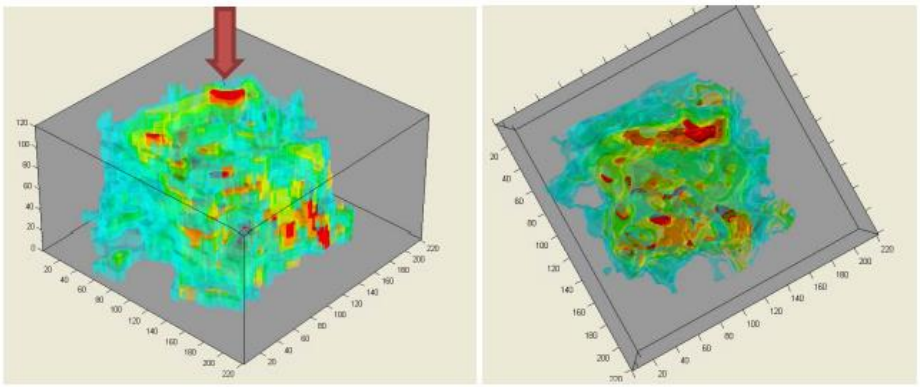

Figure 4.7 Visualization of pre-heated egg-white PAA cubic lesion from series of parallel segmented elastogram. Notice how the 3D-reconstruction of the lesion resembles a cube as in side view (left with red arrow showing the direction of the scanning step) and top view (right)

Table 4-1 Volume of pre-heated egg-white PAA cubic lesions reconstructed from segmented elastograms in different pre-compressive strains

Pre-axial compressive strain	3D reconstruction volume (cm^3)		
	Max	Min	Mean
10%	0.147	0.138	0.143±0.006
12%	0.132	0.101	0.117±0.022
14%	0.176	0.086	0.131±0.063

16%	0.151	0.141	0.146±0.007

Statistically, the 3D reconstruction volumes are close to the actual volume of the pre-heated cubic lesions. The effects of pre-compressive strain on image segmentation and 3D-reconstruction are not statistically significant. Therefore, the effects from pre-compressive axial strain will be largely assumed to be insensitive to the volume measurement results in this. In the following experiments, pre-compressive strain was chosen to be 10% as larger deformation would lead to misinterpretation of the actual object.

Spherical pre-heated egg-white PAA phantom

Similar to the previous experiment, 42 slides of lesion's elastograms with slide step of 0.2 mm were captured. The lesion was simulated by using a pre-heated egg-white PAA phantom with a spherical shape (heated bath at 60℃) embedded in an egg-white PAA phantom. Ultrasound elastography was set to operate at frequency of 10 MHz, dynamic range 80dB. Results from the preceding experiment have shown that several parameters could be used for this experiment including threshold value of 208 for segmentation, 10% pre-compressive strain and 1.0 mm/s strain rate. Figure 4.8 shows forty-two elastogram slides of the pre-heated lesion in this experiment.

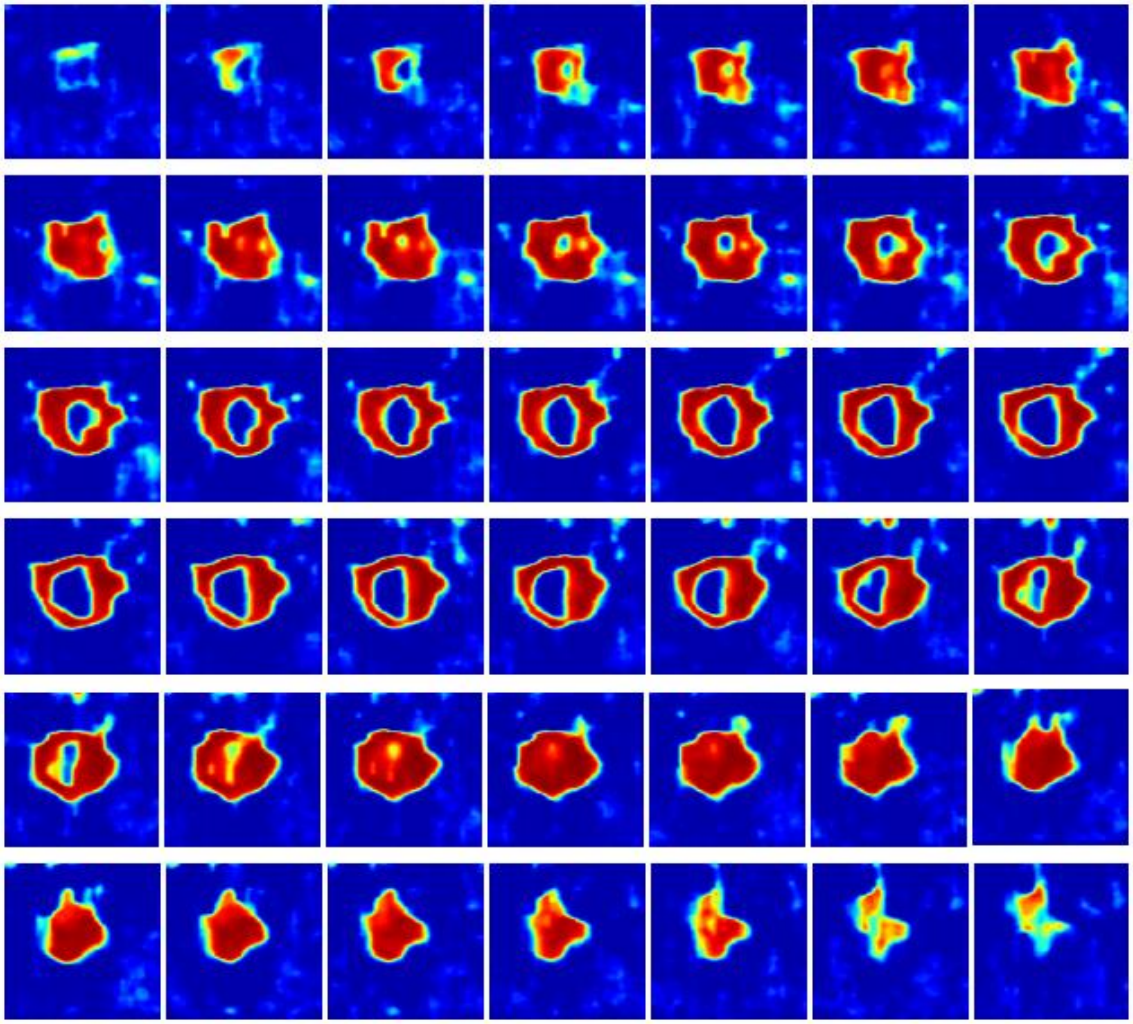

Figure 4.8 Set of parallel elastogram slides with slice step 0.2 mm in visualizing spherical pre-heated egg-white PAA lesion (ultrasound frequency 10 MHz, pre-compressive strain 10% and strain rate 1 mm/s)

The volume of the lesion from threshold segmentation approach was found to be 1.87 ± 0.3 cm^3 (Figure 4.9), compared with the actual volume 0.78 ± 0.5 cm^3. The volume of pre-heated spherical lesions was found to be overestimated. It is because that the boundary of spherical lesion is not as sharp as the boundary of cubic lesion. However, this agrees with historical experience (Chuang et al., 2010) that it gives extreme overestimation in visualizing the lesions.

The geometry of the sphere was also observed after the 3D-reconstruction. The hemisphere of the lesion which faces the applying load (from the ultrasound scanner mounted to the 3D-stage) appears to be more oblate (flattened) semi-spheroid. Figure 4-

10 illustrates how the applying load affects the geometry of the spherical lesion. The blue arrow indicates the direction in which the mechanical compression was applied.

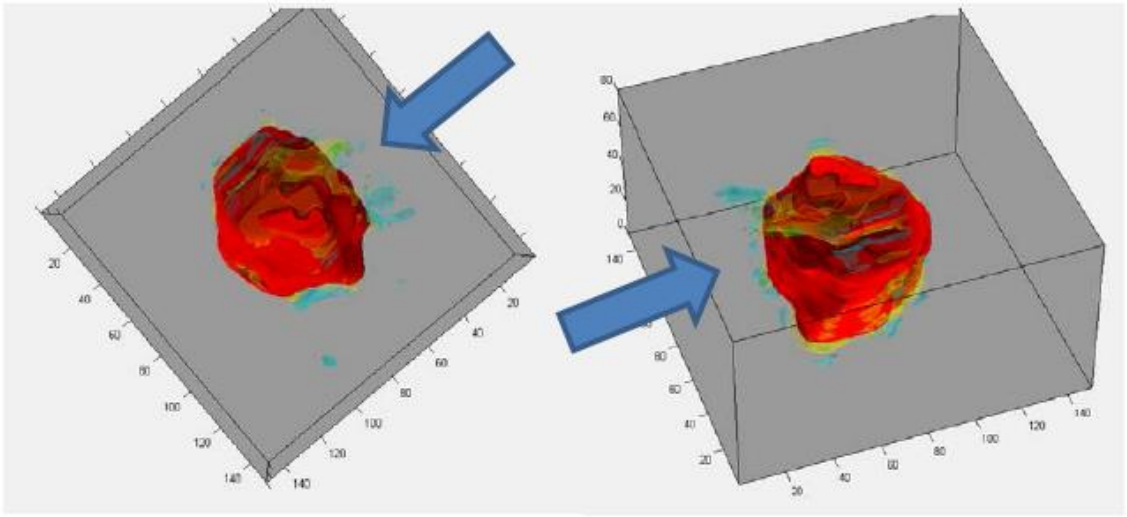

Figure 4.9 3D-reconstruction of a spherical pre-heated egg-white (40%) PAA phantom showing how the geometry of the sphere is affected under applying loads (blue arrow indicates the direction of the applying load).

4.2.2.2 Elastography of FUS-induced lesions in egg-white PAA phantom

In order to obtain the threshold power for elastographic occurrence of FUS-induced lesions, ultrasound powers at 50 W, 60 W, 70 W and 80 W were used to ablate the egg-white PAA phantoms. For each ultrasound power, ten samples (N = 10) were exposed to focused ultrasound for a fixed time of 60 seconds. The chance of occurrence for FUS-induced lesions at each HIFU power with 60 seconds duration was recorded in Table 4-2.

Above 80 W, FUS-induced lesions become visible under naked eyes after 60 seconds with a chance of occurrence of 0.8 but fall rapidly below the threshold power. At FUS power of 70 W, the occurrence probability under naked eyes of the HIFU-induced lesion falls to zero (N=10). Therefore, 70 W ultrasound power was chosen for the observation of FUS-induced lesions under ultrasound elastography.

Table 4-2 Occurrence probability of the FUS-induced lesions in egg-white PAA phantom under ultrasound elastography with respect to different power for a fixed time of 60 seconds

ultrasound power	50W	60W	70W	80W
Chance of lesion occurrence (under elastography)	0.4	0.9	1	1
Chance of lesion occurrence (under naked eyes)	0	0	0	0.8

The lesion appearances in PAA egg-white phantoms under B-mode ultrasound and strain sonoelastography have also been studied. When the lesions were clearly visual in strain sonoelastography, they could probably be observed in B-mode ultrasound scan as well. However, due to the influence of cavitation in the FUS process, the relationship between graphical views of two different ultrasound scans was unpredictable. As shown in Figure 4.10, the lesions in left and right figures formed under the same FUS does (electrical power: 50W for 10 seconds). The FUS lesions were clearly visual in strain sonoelastography scans, but the lesion was not apparent in the left figure. We could conclude that it is more easily to visualize FUS lesions in PAA egg-white phantoms using strain sonoelastography than using B-mode ultrasound scan.

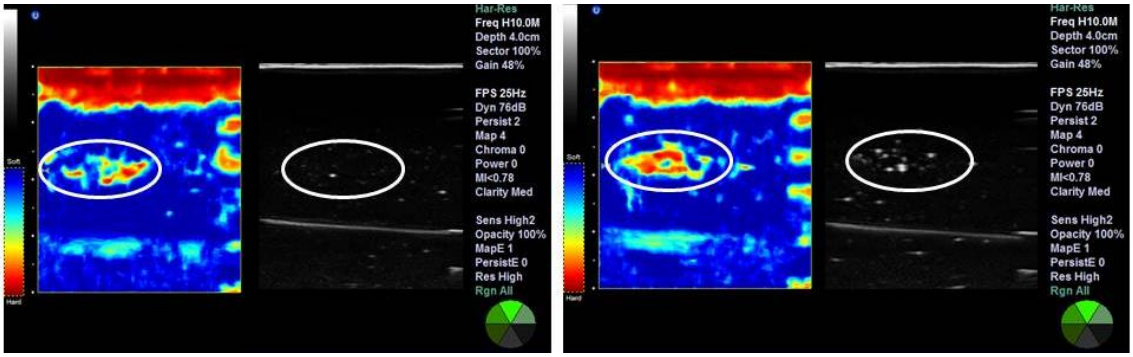

Figure 4.10 Different graphical views of FUS lesions in strain sonoelastography and B-mode ultrasound scans. The two scans were got under the same FUS dose (50 electrical Watt for 10 seconds) in PAA egg-white phantoms. In the left figure, the lesion was not clear in the B-mode ultrasound scan.

The second experiment investigates the effect of the duration of focused ultrasound (at 70 W) on the size of the FUS-induced lesions and their occurrence probability. The duration of the focused ultrasound sonication varies from 15 seconds to a maximum of 30 seconds since the observation of FUS-induced lesions under ultrasound elastography reaches 100% at 30 seconds. Table 4-3 summarises the growth of FUS-induced lesions and the chance of this being detected under ultrasound elastography with respect to the duration of focused ultrasound exposure. In 15 seconds of exposure time, the FUS-induced lesions (if any) tend to occur randomly and discretely. For example, when egg-white PAA phantom were exposed to FUS of 70 W for 15 seconds, FUS-induced lesions occur as separated and small lesions (Figure 4.11).

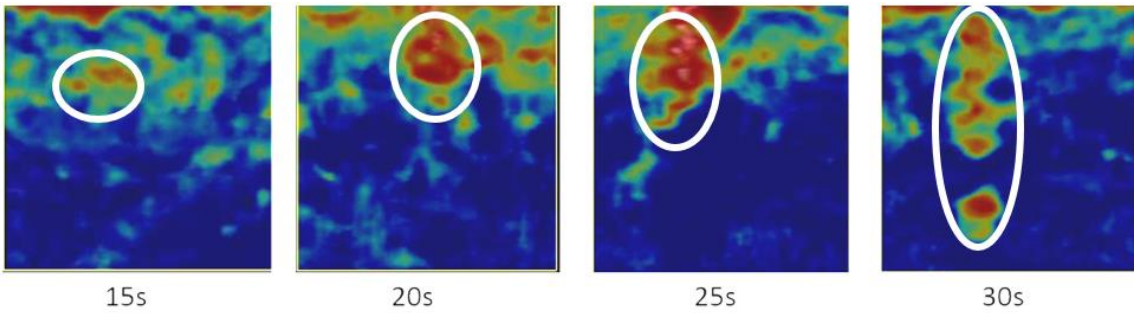

Figure 4.11 Lesion formation in homogeneous PAA phantom

Table 4-3 Mean cross-section area and occurrence probability of the FUS-induced lesions in egg-white PAA phantom under focused ultrasound exposure at 70W

Time (seconds)	15	20	25	30
Cross-section area (mm^2)	9.1±5.6	11.3±6.4	13.1±9.6	24.1±16.8
Chance of lesion occurrence	0.4	0.6	0.9	1

For longer durations, the lesions did not increase in the number but the size that suggests the duration of ultrasound ablation is independent of the driving force in lesion's formation.

Another important finding was that the original condition also affects the size and number of FUS-induced lesions. For 30 seconds of FUS sonication (70 W) in inhomogeneous egg-white PAA phantom, both the number and size of the FUS-induced lesions increase significantly. An example, in which FUS sonication site was chosen with several artefacts (inhomogeneity) as an initial condition, is shown in Figure 4.12. FUS-induced lesions (70 W) under elastography (pair of left-hand-side columns) with different duration of FUS sonication subjected to their initial conditions (homogeneous/inhomogeneous); and their corresponding segmented elastograms (pair of right-hand-side columns). Apparently, the size and number of FUS-induced lesions in inhomogeneous PAA phantom significantly differ from the ones with homogeneous initial condition.

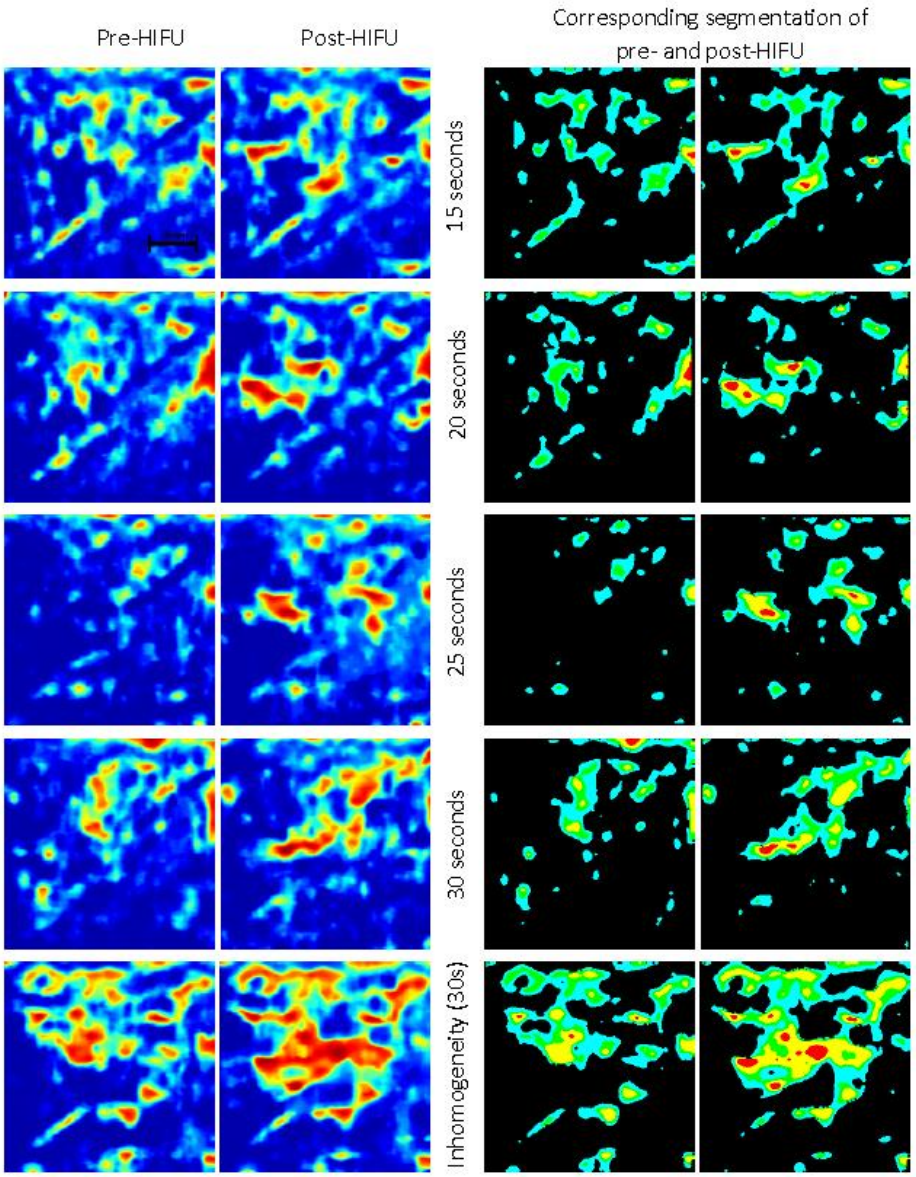

Figure 4.12 FUS-induced lesions (70W) under elastography (left) with different duration of HIFU exposure subject to their initial conditions (inhomogenity) and their corresponding segmented elastograms (right)

The onset of FUS-induced lesions seems to be random and independent of the time of focused ultrasound exposure in the timescales longer than 15 seconds. Once the FUS-induced lesions are formed, a longer exposure to FUS affects mainly the size of the lesions rather than their population. Although lesions are induced randomly by FUS, they usually cover the focal region with an average (yet to be investigated) distances. Lastly, inhomogeneity present in the sample (egg-white PAA phantom in this experiment) seems to facilitate the induction of FUS lesions in both size and number.

These conclusions were drawn based on assumption that ultrasound elastography reflects correctly the changes in physical properties of the samples.

4.2.2.3 Elastography of FUS-induced lesions in fresh sheep liver

Data for constructing pixel density were gathered from ten pair of elastograms (N=10 from each pre- and post-FUS). Therefore, the optimum threshold value for segmentation the marker was chosen to be 224 (labelled as red colour in the segmented image).

Another segmentation level was chosen to be 192 (labelled as yellow colour in the segmented image). Below this threshold level, the area of ablation in pre-FUS elastograms is not statistical different from the one in post-FUS elastograms. This region within this segmentation level serves as a boundary between the core of the FUS lesion and the surrounding-unaffected tissue. These regions are considered to be stiffer than most of the surrounding tissues but cannot be distinguished from artefacts.

Threshold level at 160 (Green) and 128 (Cyan) was also investigated to confirm the prediction that was drawn from cumulative pixel density. If the prediction is accurate, these thresholds can distinguish between FUS-induced lesions and the surrounding tissues.

Three different case studies were performed to characterize FUS-induced lesions, at different powers and durations of sonication, under ultrasound elastography. The acquired elastograms and their segmented images are shown in Figure 4.13.

In case 1 (40W-40s), the average FUS-induced lesions are the largest with regards to the cross-section area along the major axis. Statistical analysis has shown that the cross-section area of the lesions in case 1, case 2 and case 3 are 1.88 ± 0.41 cm2, 0.55 ± 0.03 cm2 and 0.73 ± 0.07 cm2 respectively.

Case 1 (40W-40s) has both higher ultrasound power and longer duration of sonication than the other two cases. Lesions in case 2 (40W-30s) appear to be larger than the ones in case 3 (30W-40s). The lesions in case two were observed from the elastograms and their segmented images to be more prolated than in case 3 (higher major axis-diameter

of equatorial ratio). This is possibly due to lower power and longer HIFU sonication. Prolonged HIFU-sonication would allow longer heat diffusion to take place and subsequently, the protein-denatured region would resemble a sphere.

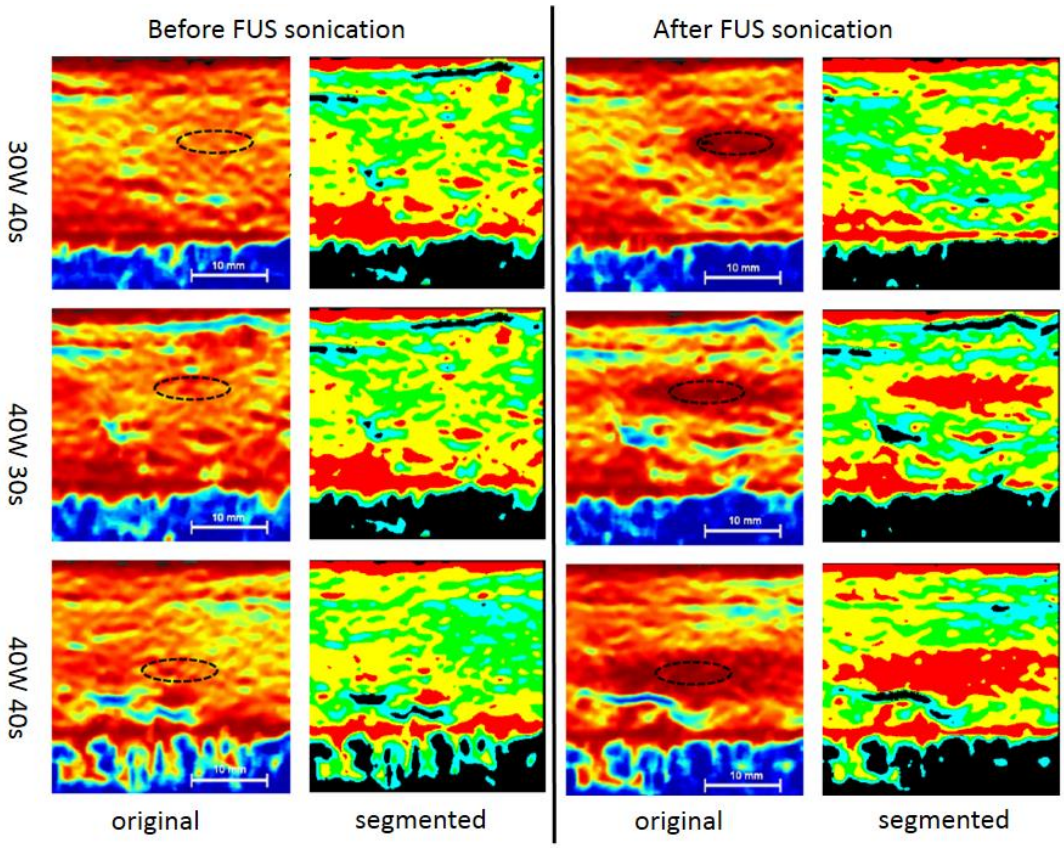

Figure 4.13 Images before and after segmented processing of pre- and post-FUS sonication under ultrasound elastography regarding to different FUS power and duration in fresh sheep livers (dotted ellipse indicates focal zone)

A study has been done to compare the appearance of lesions in fresh sheep livers under strain sonoelastography and B-mode ultrasound scan. Similar results to what happened in PAA egg-white phantoms were got. As shown in

Figure 4.14, the lesions in left and right figures formed under the same FUS does (electrical power: 40W for 30 seconds). The FUS lesions were clearly visual in strain sonoelastography scans, but the lesion was not apparent in the left figure. We could conclude that it is more easily to visualize FUS lesions in ex vivo sheep livers using strain sonoelastography than using B-mode ultrasound scan.

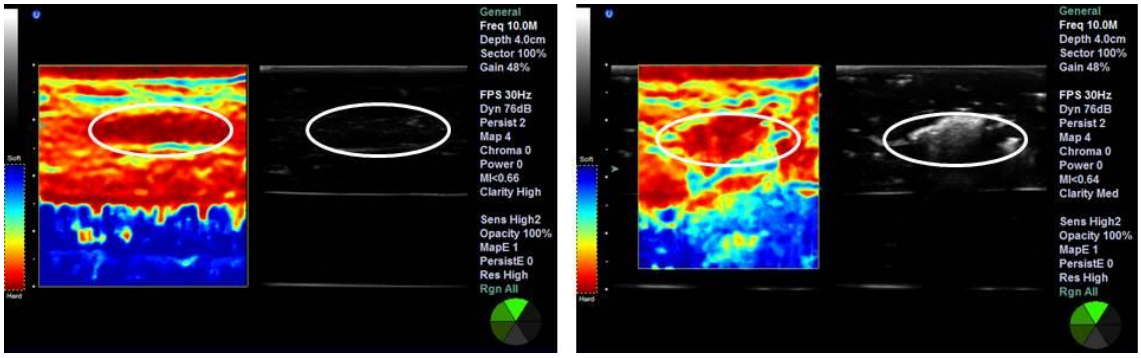

Figure 4.14 Different graphical views of FUS lesions in strain sonoelastography and B-mode ultrasound scans. The two scans were got under the same FUS dose (40 electrical Watt for 30 seconds) in fresh sheep livers. In the left figure, the lesion was not clear in the B-mode ultrasound scan.

In conclusion, ultrasound elastography has the potential to monitor the focused ultrasound induced lesions through indirect tissues elasticity measurement. Through appropriate segmentation method, protein-denatured region can be quantitatively assessed for the detection of lesions in *ex vivo* liver tissues. Either higher ultrasound power or longer duration would yield a larger protein-denatured region. Lesions in prolonged FUS sonication generally appear to be less prolated but further investigations are required to draw the final conclusion.

4.3 Summary

In this chapter, a method using strain ultrasound elastography was derived that can identify FUS-induced lesions in PAA egg-white phantom and animal tissues (fresh sheep livers). The method to differentiate FUS-induced lesions in different samples was characterized under different powers as well, with different power and duration of FUS sonication under ultrasound strain elastography.

Firstly an experimental setup was built to fix diagnostic ultrasound probe and a bowl shaped HIFU transducer. The axis of the diagnostic ultrasound probe is perpendicular to the axis of the HIFU ultrasound transducer. The axis of the HIFU ultrasound transducer

is kept within the ultrasound imaging plane so the lesion area will be observed easily in diagnostic ultrasound images.

There are two types of samples used in this study, Egg-white PAA phantom and fresh sheep liver, for a feasibility study of the use of ultrasound elastography in assessing FUS-induced lesions. The PAA egg-white phantom is a representative tissue mimicking material for HIFU research and the liver tissue is a representative organ in the abdominal.

Three studies were conducted to assess the performance of ultrasound elastography to detect and characterize FUS lesions.

In the first study, pre-heated cubic and spherical lesions were embedded into an egg-white PAA phantom. 3D-reconstruction was employed to visualize the segmented lesions and to evaluate their volumes. Because the volume of the lesion was known in advance, this method could assess the accuracy of the image processing of ultrasound strain elastography. Different pre-compressive strains were also investigated for the effect on 3D-reconstruction. Results showed that the precision image processing method was in an acceptable level. The image processing and 3D reconstruction had higher precision on cubic shaped lesions than spherical shaped lesions. In this study, pre-compressive axial strain was chosen to be 10% after comparing the influence of different pre-compressive strains on the 3D reconstruction precision.

The second study investigates FUS-induced lesions and its characteristics with respect to ultrasound power and duration in egg-white PAA phantom. The threshold level of electrical power of focused ultrasound for the ultrasound strain elastography to detect was found to be around 80W. The findings of the second study enabled the comparisons with the findings in ex vivo fresh sheep liver regarding FUS-induced lesions. In this study, the conclusion was made that either higher ultrasound electrical power or longer ultrasound duration would result in larger and clearer lesions in ultrasound strain elastography, which indicated a potential for using this method to detect or monitor the lesions formation in fresh tissues for FUS.

In both PAA phantoms and fresh sheep livers, the FUS lesions are more easily to visualize using strain sonoelastography than using B-mode ultrasound scan. In PAA egg-white phantoms, strain sonoelastographpy could visualize FUS lesions more easily than naked eyes.

To conclude, useful information (area, stiffness) of the FUS-induced lesions could be extracted from the ultrasound strain elastographic features. Although being lack of quantitatively measuring the Young's modulus of materials, strain ultrasound elastography has been proven to be useful in assessing the protein-denatured regions of FUS sonication in egg-white PAA phantom and fresh sheep liver.

Chapter 5 Robotic arm asssited MRgFUS

5.1 Introduction

Complete FUS intervention requires a series of sonications and focus repositioning. Such a focal spot scanning technique can be realized mechanically via robotic actuators or via electronically phased-element transducers. However, robotic actuators allow a wider spatial range and a more versatile treatment access than via electronically phased-element transducers especially in MRgFUS when the MR scanner restricted the operational range of the HIFU transducer.

The work in this chapter mainly focused on using a MR compatible robotic arm (Melzer et al., 2008) to guide a custom made fixed focused transducer for FUS treatment.

The registration methods for medical devices within the MR scanner coordinate system can mainly be divided into two categories. The first is based on passive contrast (Patil et al., 2009) markers and the second is based on semi-automatic resonance radiofrequency (RF) coils (Flask et al., 2001, Thormer et al., 2012). These passive markers are flexible for localization and especially safe for endorectal prostate biopsy (de Oliveira et al., 2008) or other catheter interventions since they do not involve any connecting wires and related tissue heating risks (Konings et al., 2000) during MRI. However the localization usually employ a more complex analysis of the image data (Rea et al., 2009) which makes this passive tracking approach relative time consuming and susceptible to the SNR of MR scans. The original registration method for our robotic arm is using passive contrast agent (Gadolinium doped solution with a volume ration of 1:100) filled markers. Another tracking method is based on active markers which are resonant pick-up RF coils whose position can be measured by a dedicated non-imaging MR pulse sequence that uses one dimensional projections (Dumoulin et al., 1993). Active tracking markers benefit medical devices for its high accuracy and fast position updates although their applications are restricted by the number of MR receiver channels and potential safety hazards due to the long conducting wires that connect the coil and the receiver of the MRI scanner. Considering that the ultimate purpose of the present work was to

optimize the combined robotic MRgFUS system, which is supposed to be non-invasive, active tracking was chosen as the method for guiding the robotic arm.

The purpose of this part of study was to investigate if active tracking would allow a wide spatial range for repositioning the FUS transducer fast and accurately. The original registration method for the robotic arm is described and compared to the proposed method. The basic rationale of active tracking as well as the novel integration of active tracking and the calibration method for the robotic system is presented. This work serves as a feasibility study of MRI guided FUS treatments with robotic assistance and was demonstrated on a clinical 1.5T MRI scanner by means of phantom ablation experiments.

Furthermore in the next chapter, the robotic arm with the new localization method will be used in a setup which provides a back and forth movement for a phantom. With this setup, the idea of MRgFUS for moving target is going to be investigated.

5.2 Materials and methods

5.2.1 Robotic arm with passive tracking

The MR compatible robotic arm is a pneumatically driven system with 5 degrees of freedom (DOF), which can be controlled to move at a translational range of ±50cm, while at a rotation of $\pm 40°$ in transverse and $-23° / +70°$ in the sagittal direction (Figure 5.1). The accessible space range could almost cover the whole field of view (FOV) of the clinical 1.5T MRI scanner (Signa HDxt, GE Medical Systems, Waukesha, WI, USA). A previous study demonstrated that the robotic system can achieve an overall positioning accuracy of ±1 mm in translational direction and $\pm 1°$ in angular direction respectively, which correlates to the specifications of the manufacturer (Melzer et al., 2008, Cleary et al., 2006).

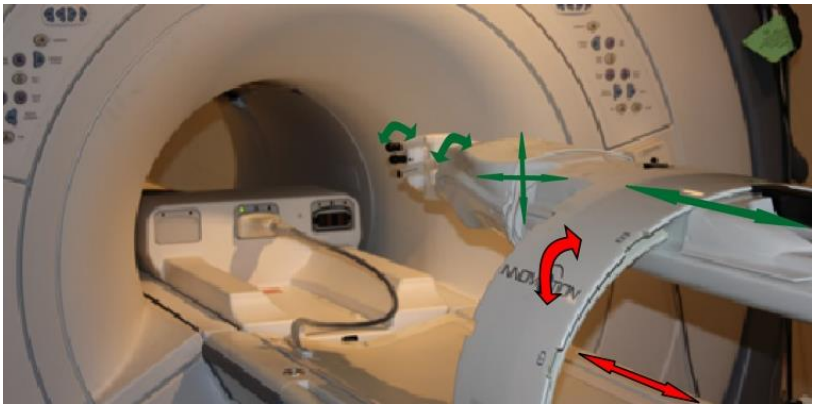

Figure 5.1 Front view of the robotic arm in front of a 1.5T MRI scanner,5 degrees of freedom of the INNOMOTION robot (green arrows) and two manual DOF (red arrows);

The original position registration method of the robotic arm system is based on passive markers. Four spherical passive markers (Figure 5.2a) are attached to the application module of the robot. The registration requires three MRI images, one in the transverse plane and two coronal planes. The transverse scan has to contain all the four markers and each of two coronal or oblique scans two markers at the same height (Figure 5.2b). The coordinates of the four markers are then computed using a centre-of-mass imaging processing approach (Figure 5.2c, d, e), and then the position of the robotic arm is determined accordingly. Besides a long time required, this approach also requires a priori knowledge of rough position information of the markers in order to select the appropriate scan planes and to detect the markers.

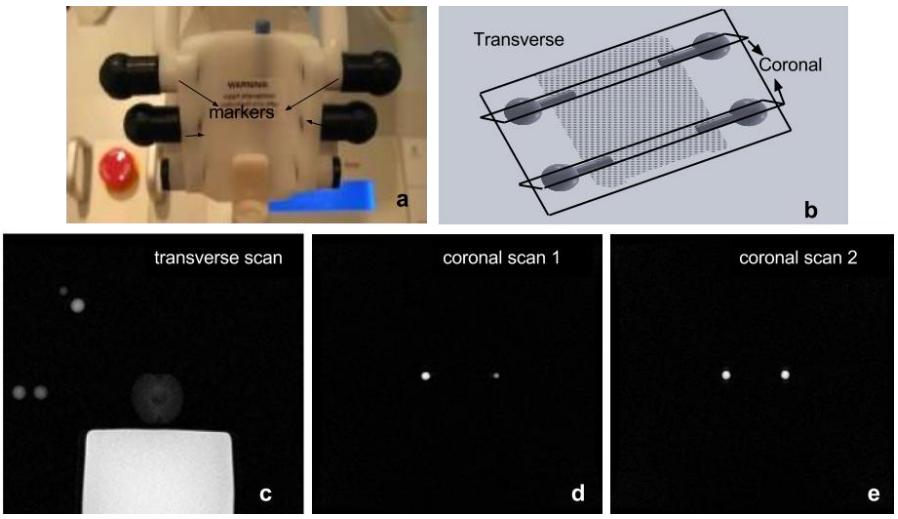

Figure 5.2 Passive method of confirming the position of robotic arm. (a) The four ball-shaped markers are filled with a Gadolinium based contrast agent; (b) The MR scan orientation of the robot markers for its position registration in the MR frame reference frame; (c), (d), (e) MR images of the four markers, the transverse scan plane has to contain all four markers, and each of the coronal scan planes has to contain two of them at the same height.

5.2.2 Active tracking of the robotic system

To speed up the registration of the robotic arm in the MR frame reference, micro-coils (Dumoulin et al., 1993) are used to replace the passive markers on the application module. Four micro-coils, which are 2 mm in diameter and 5 mm in length are fixed on a round PVC board with a diameter of 200mm (Figure 5.3a). Every micro-coil is a solenoid coil with 7-8 loops winding and includes a small volume of 100:1 aqueous Gadolinium contrast agent solution (Figure 5.3b, c). A coaxial cable connects the four micro-coils, each to a MRI receiver channel for the scanner to acquire MR data from the micro-coils respectively.

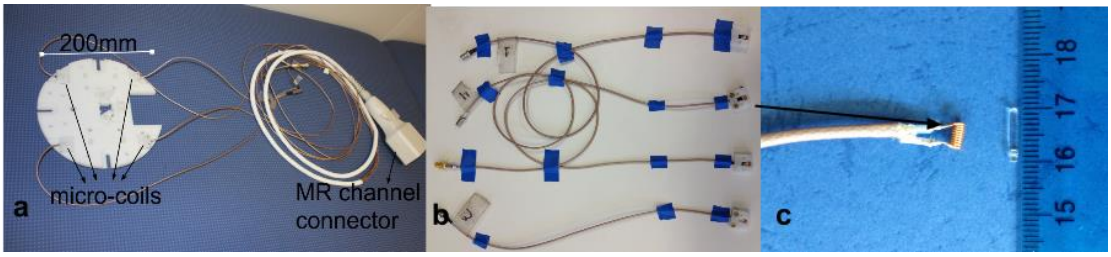

Figure 5.3 Active tracking hardware (a) Round tracking plate with four active micro-coils, the connector channel is used to connect the micro-coils to the MR receiver; (b) Micro-coils with coaxial cable and Bayonet-Neil-Concelman (BNC) connector (c) Dimension of the micro-coils and the container with the Gadolinium contrast solution.

The NMR signals from these micro-coils are generated with a non-imaging pulse sequence (Figure 5.4a) that employs a non-selective radiofrequency (RF) pulse (Dumoulin et al., 2010), which excites all the spins within the FOV of the excitation coil. MR signal detection by the micro-coils occurs in the presence of a frequency-encoding gradient, and then the pulse sequence is applied four times in a Hadamard

multiplexed readout scheme to reveal the location of the micro-coils and to compensate for off-resonance effects (Dumoulin et al., 1993). Sharp peaks (Figure 5.4b, c) will be observed in the power spectrum whose frequency is indicative of the location of the micro-coil along respective dimensions. The Hadamard encoding method is then employed to determine the X, Y, and Z positions (Dumoulin et al., 1993) of the micro-coils from the acquired projections. A phase-field dithering method is integrated to improve the SNR (Dumoulin et al., 2010).

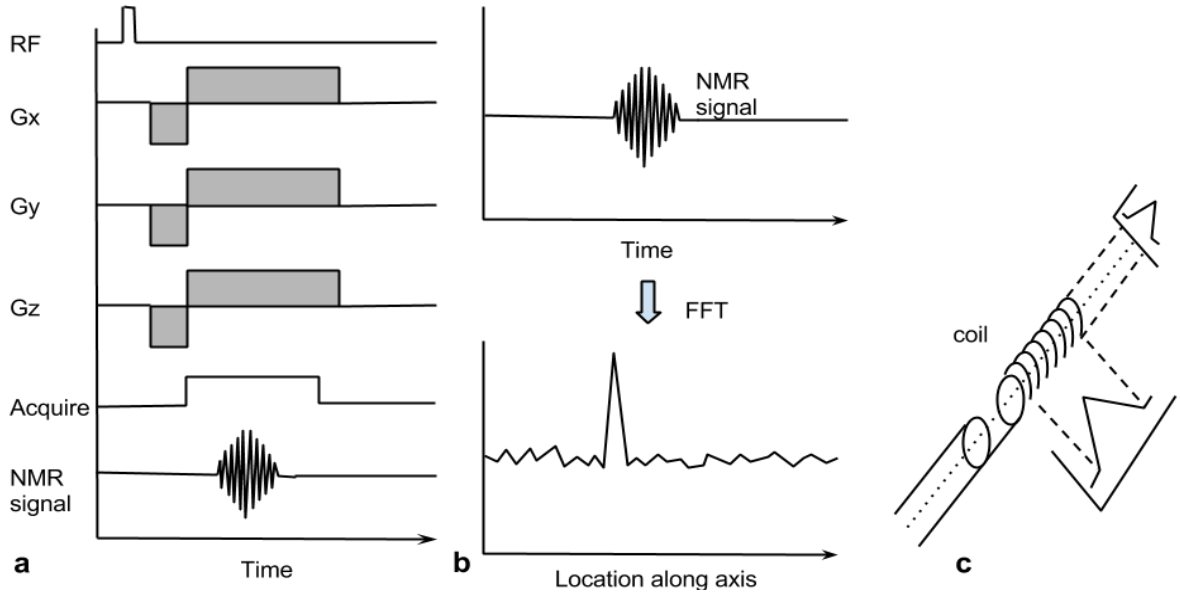

Figure 5.4 Basic pulse sequence diagram for real-time tracking of micro-coils with MR as previously proposed (Dumoulin et al., 2010). Note, phase-field dithering is not shown for simplicity. (a) The pulse sequence employs a non-selective radiofrequency pulse that excites all spins within the active volume of the excitation coil. MR data are acquired in the presence of a frequency-encoding gradient; (b) The position of a signal source (micro-coil) with respect to an applied magnetic field gradient is determined by Fourier transformation of the NMR data; (c) Diagram of NMR signal peaks of the micro-coil

Since only four repetitions (Figure 5.5a) are needed to determine the three dimensional locations of the micro-coils, the tracking duration is 4×TR (Repetition Time = 5ms) which is faster than passive tracking (Dumoulin et al., 1993) that is based on image post-processing. To improve SNR, six phase-field dithering directions are applied for

every repetition (Dumoulin et al., 2010) which increases the tracking duration to 6×4×TR (120ms).

The tracking sequence was implemented in the research real-time MRI software frame work RTHawk (0.9.28, HeartVista, Inc, Palo Alto, CA, USA). With a workstation (Quad-Core Intel Xeon, 32G RAM), the tracking rate can achieve as high as 8.3 frames per second. The geometrical centre of the four micro-coils is used as the position of the application part of the robotic arm, the normal vector of the plane is then constructed from the four micro-coils and represents the orientation of the application module of the robot (Figure 5.5b), which coincidences with the axis of medical devices, e.g. biopsy needle or FUS transducer. The position of the robotic arm is marked in a reconstructed 3D MR space (Figure 5.5c), from which the relative relationship between the robotic arm and the target phantom or tissue can be obtained.

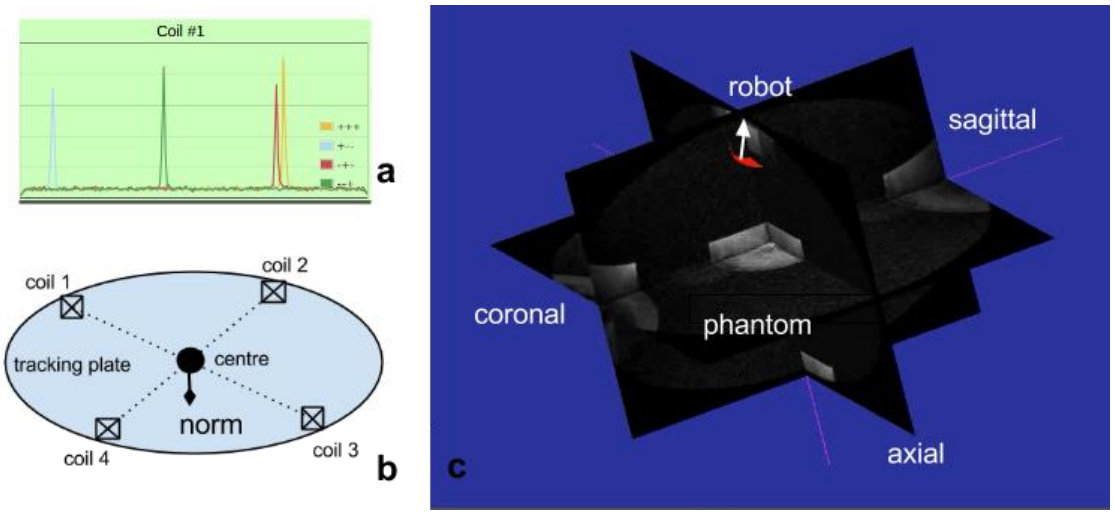

Figure 5.5 (a) Exemplarily tracking plot for one micro-coil (No.1). The four peaks represent the result of the Fourier transform of the NMR data. Note that the four colours and peaks represent the data that are acquired with the four Hadamard encoded readouts; (b) Structure of the four micro-coils, the four coils are distributed evenly on the round plate; (c) Reconstructed position of the application module of the robotic arm in a 3D MR space. Three orthogonal MR planes are rendered in 3D MR space, the position and orientation information is also demonstrated.

5.2.3 Calibration

Before applying the active tracking technique to a FUS treatment guided with the robotic arm, a calibration experiment was required to evaluate the tracking accuracy in a specific range (Figure 5.6, not in scale). A dark green area means the maximum reachable range of the robotic arm. After a rough measurement, it was determined that the application module of the robot can move within a range of -170mm to +170mm in the sagittal, -80mm~100mm in the coronal and -70~70mm in the axial direction at flexible gestures. Active tracking was tested in an area of 160×160×140mm (sagittal, coronal and axial directions respectively. This is indicated as light green area in Figure 5.6.

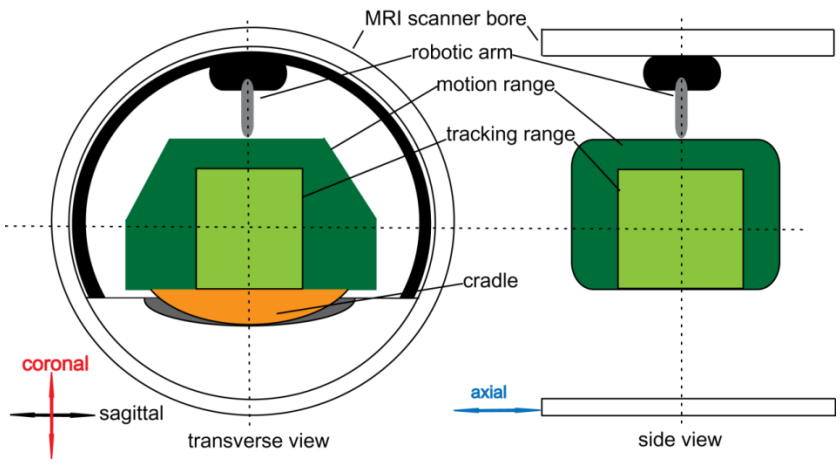

Figure 5.6 Diagram of MR scanner, robotic arm and its motion range (dark green), the tracking experiments were carried out in the light green area.

A 3D reference model (Figure 5.7) was designed to provide reference points for the test. Reference points were distributed on a phantom made of 5% proportion agar with the size of 140×140×140mm. The 35 reference holes are located uniformly on seven different layers, the height distance between two adjacent layers is 20mm and the lateral distance between two adjacent holes is 30mm.

A plastic box was prototyped to allow manufacturing the actual agar phantom as impression. The phantom was positioned in the scan room for over 48 hours before

calibration experiments. It was found that the 5% proportion agar was stiff enough that the overall dimension change was negligible for the accuracy study.

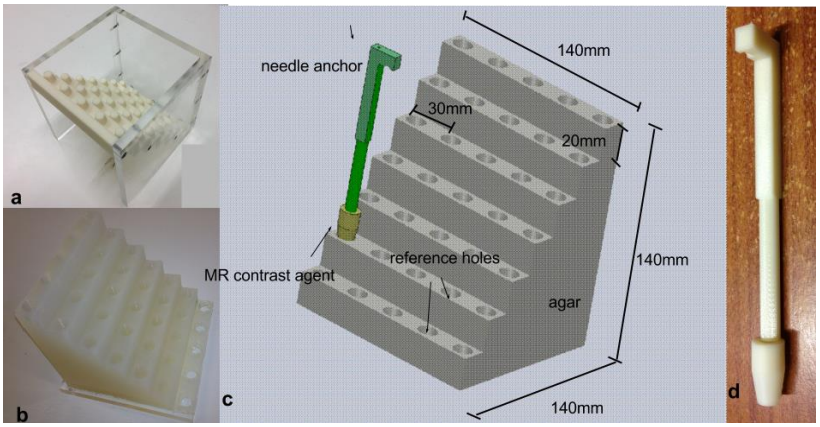

Figure 5.7 (a) Phantom box; (b) 3D reference phantom extracted from the box; (c) Diagram of how the needle anchor located at the reference points of the agar phantom; (d) Needle anchor that fits into the reference holes of the phantom, the upper connector was fixed at the applicator module of the robotic arm

To confirm the robotic arm reaching the reference points, a straight needle anchor (Figure 5.7d) was rigidly fixed at the centre of the tracking device. The end of the needle anchor was filled with Gadolinium doped gelatine. The described active tracking implementation was used to monitor the robotic arm while guiding the needle anchor to reach all reference points of the phantom on a point-by-point basis. The tip of the needle anchor appeared brighter than the agar phantom. This enabled the user to confirm its position in MR images (Figure 5.8a, b) that were obtained with an interventional coil (DuoFlex, MR Instruments, Hopkins, MN, USA). The MR images (Gradient echo, TR/TE=100/30ms, flip angle=60 °, bandwidth=31.2kHz, FOV=15×15cm, matrix=512×512, slice thickness=2mm) served for the confirmation of whether the needle anchor was at the correct location or not. Additionally, a wireless surveillance web camera (M1011w, Axis, Lund, Sweden) (Figure 5.8c, d) with 10x zoom lens was used to confirm the position of the robotic arm.

Figure 5.8 (a) 3D model of the phantom and needle anchor. MR scans (b) to confirm the needle is at the correct position. (c, d) The web camera was used to monitor the needle anchor while it was positioned into the reference holes of the agar phantom as well.

At every reference point, the robotic arm position could be computed from the coordinate readout of the four micro-coils. Comparing the calculated coordinates with the theoretical positions, the tracking reliability of the micro-coils could be concluded.

Besides the tracking position errors, the orientation errors could be computed by comparing the norm of the plane formed by every group of four active trackers with the coronal direction in MR bore.

5.2.4 Phantom sonication

A phantom sonication experiment was designed to apply the tracking technique for robotic arm guided FUS based on the previous calibration. All the sonications were conducted in a 1.5T whole body MR scanner (Signa HDxT, GE Healthcare, United States) with a breast coil (InSightec, Ltd., Tirat Carmel, Israel).

The tracking plate is an exchangeable device, which has a clip for fastening a US transducer (Figure 5.9). The single-element US transducer was fabricated according to MRI compatible requirement. (working frequency: 1MHz, focal length: 70 mm, aperture: 60 mm; elliptical -3dB focus size: ø = 1.8mm; length = 10mm, weight: 180g). The bowl shaped transducer can provide a maximum acoustic power of 60W. No acoustic output measurements have been made for this transducer since this experiment is only for preliminary (nonqualntitative) study (ter Haar et al., 2011).

A target egg-white gel phantom (Gao et al., 2012) with size of 100×50×50mm was used for several different patterns sonication. The egg-white percentage was to 25% in order to make it more transparent for lesions visibility.

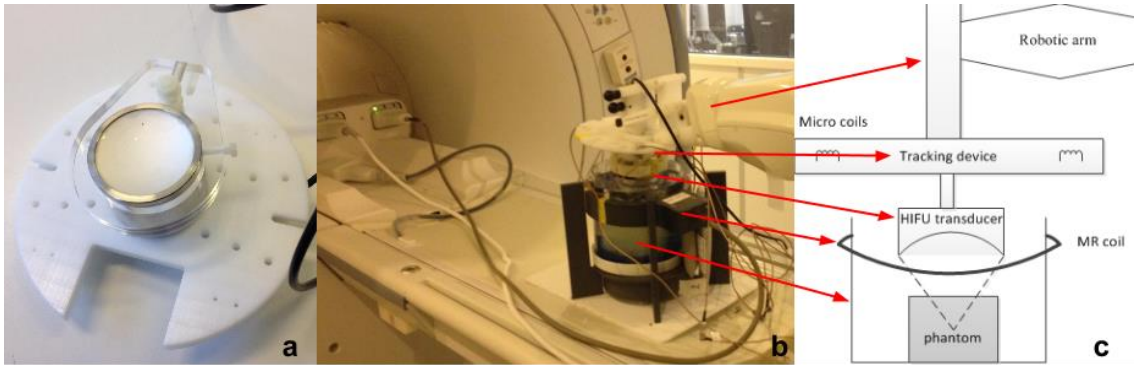

Figure 5.9 (a) FUS transducer fixed to the tracking plate (b, c) Schematic diagram and photo of the robotic arm used to guide the FUS transducer for sonications. From top to bottom is the robotic arm, the tracking plate, the FUS transducer, the breast coil, and the egg-white gel phantom. The FUS transducer was placed into degassed water for coupling with the target phantom.

The US transducer replaced the needle anchor, so geometrically the registration of the transducer in the MR reference frame could be done similarly. A breast coil with radius of 100mm was setup as metacoil and used for simultaneous tracking and MRI based thermometry (Rieke and Butts Pauly, 2008). Three phased MR image for thermometry are located near the focus according to the relative distance from the FUS transducer to the centre of the four micro-coils (Figure 5.10). Considering the restriction of the whole setup, the US transducer allows a maximum sonication volume of $5\times5\times4$ cm^3 to ablate.

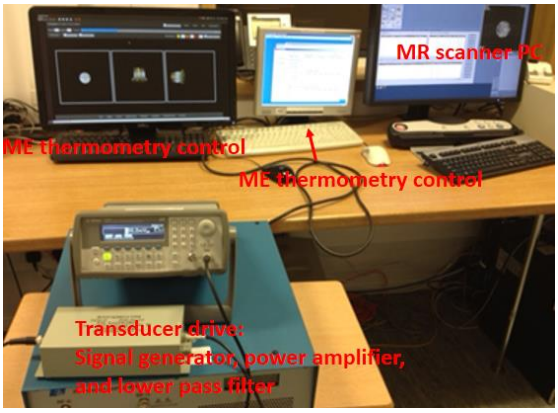

Figure 5.10 Setup of Focused ultrasound sonication on PAA phantom outside of MR room.

Two series of sonications were performed with this setup (Figure 5.11). Both of them were with three layers, and the distance between two layers was 10 mm. In the first series, 2 targets were sonicated at the first layer, four targets at the second and sixteen at the third. The second series was as an L-shaped structure with four targets at the first layer, 6 targets at the second and eight at the third. All the target points in a same layer were aligned as a letter 'L' from top-bottom view. For each layer, the leisions were parallel to the axial and sagittal direction, and the layered direction was the coronal axis of MRI bore.

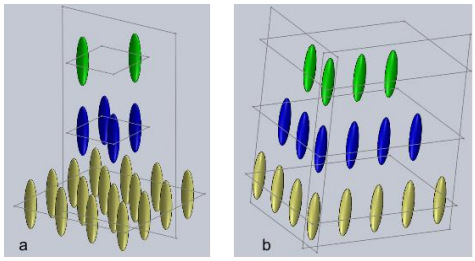

Figure 5.11 Two planned series of ablation. (a) The target points were distributed in square shape in every layer, the two targets at the top layer occupy the two corners of a square; (b) target points were distributed in an L-shaped structure, the number of target points was descending from top layer to bottom layer.

The post-FUS lesions were observed by both naked eyes and T2-weighted MR scans (FRFSE; TR/TE=3000/79 ms; FOV=10×10 cm; matrix: 256×256; slice thickness=5 mm; bandwidth=31.2 kHz). For each sonication pattern, the ablations area was scanned vertically and parallel to the axis of US beam (Figure 5.11). Then the centroid positions and the sizes of the lesions were calculated using a centre-of-mass algorithm (ImageJ) based on the MR images at a sub-pixel level to evaluate the positioning performance of the active tracking assisted FUS system.

5.3 Results

5.3.1 Calibration experiment

The geometrical centre of the four micro-coils is used as the position of the application part of the robotic arm, and the normal vector of the plane of the four micro-coils represents the orientation of the application module of the robot (Figure 5.5b).

The tracking accuracy at each measured point was determined by comparing the measured positions $\vec{r}_m$ with the theoretical positions $\vec{r}_r$ provided by the reference phantom on a point-by-point basis as $\vec{\epsilon}_i = \vec{r}_{r_i} - \vec{r}_{m_i}$ (Andrew et al., 2004). Note that all the errors are positive from the equation of $|\vec{\epsilon}_i| = |\vec{r}_{r_i} - \vec{r}_{m_i}|$. The distance error distribution for the centre of four micro-coils is plotted as a frequency histogram (Figure 5.12).

In the measurement range 160×160×140 mm (Figure 5.6), the overall RMS distance error is 0.43 mm (labelled B in Figure 5.12). Most of the errors lie within twice the actual RMS, with the maximum error (labelled D in Figure 5.12) being an order of magnitude greater than the RMS. Errors larger than 2.00 mm happened at the boundary of the measurement range, and were spotted twice in a total measuring number of 149. The mean error and standard deviation are computed as well (labelled A in Figure 5.12). However they are not preferable for the data interpretation since the distribution is clearly not normal which skewed heavily to higher errors.

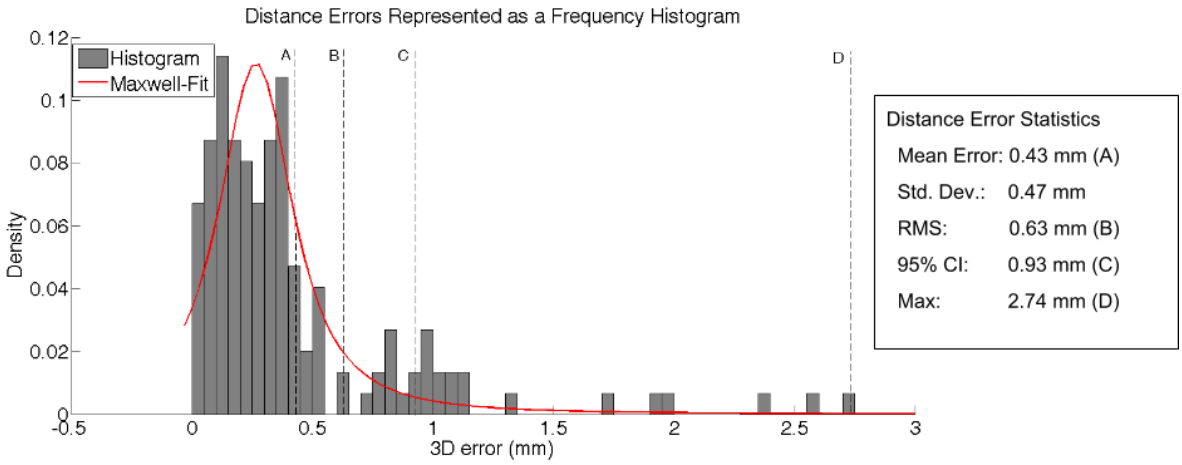

Figure 5.12 Frequency histogram of the distance errors for the centre of four micro-coils. The distribution is roughly estimated to a Maxwell probability distribution. A distance error statistical summary is listed including the RMS, the bias (mean error), its spread (standard deviation), maximum error and 95% confidence interval (CI), which are labelled in the histogram.

The Maxwell distribution curve does fit similarly but not completely to the data (Andrew et al., 2004). Figure 5.13 shows the errors in the coronal direction play a more important role than the other directions for the distance errors. This implies that the distance errors have a dependence of coronal direction, which is not completely in conformity with Maxwell probability distribution.

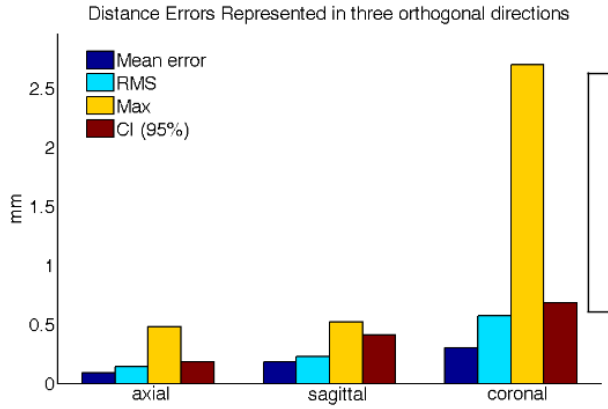

Distance Error along MR axis (mm)

	Mean	RMS	Max	CI(95%)
axial	0.09±0.11	0.14	0.48	0.18
sagittal	0.18±0.14	0.23	0.52	0.41
coronal	0.3±0.49	0.57	2.7	0.68

Figure 5.13 Distance error bars in three orthogonal directions for the centre of four micro-coils. The distance errors are positive. The statistical summary contains the bias and standard deviation, maximum error and 95% CI.

The gross systematic errors in the coronal direction are due to the shape changes of the gel phantom because of its elasticity and water loss. However the Maxwell fit could give us a brief idea of the errors distribution, the CI indicates that 95% errors are restricted smaller than 0.93 mm (labelled C in Figure 5.12).

The results of the distance errors for each micro-coil, as well as the average results are shown in Table 5-1. Compared to Figure 5.12, the distance errors for the application module of the robotic arm are slightly, but significantly, better than the single micro-

coil results, which is a consequence of the inherent averaging of the micro-coils errors during the calculation of the centres from the underlying micro-coils positions.

Since the four markers theoretically constructed a rigid-body, the orientation errors are calculated by comparing the norm of the tracking plate which fitted from the coordinates of four micro-coils with the coronal direction vector of the MRI bore. The bias of orientation errors is 0.31 °(mean) or 0.36 °(median) with a standard deviation of ±0.15 °. Ninety-five percent of orientation errors are smaller than 0.50 °.

Table 5-1 Accuracies for individual micro-coils, as well as their averaged results.

Marker	RMS (mm)	Mean (mm)	Std. Dev. (mm)	Max (mm)	95% CI (mm)
Micro-coil #1	0.80	0.54	0.60	3.24	1.15
Micro-coil #2	0.78	0.50	0.59	3.44	0.99
Micro-coil #3	0.68	0.50	0.47	2.79	0.96
Micro-coil #4	0.73	0.53	0.51	2.68	1.07
Average	0.75	0.52	0.54	3.04	1.04

To summarize, the active tracking was calibrated in the whole measurement area (140×160×180 cubic mm, Figure 5.6). The distance errors for the centres of four micro-coils are presented with RMS = 0.63 as well as the 95% CI with 0.93mm. The distance errors are greater in coronal direction than in the other directions. To some extent, the orientation errors of the setup show a bias and its spread as 0.31 ± 0.15 °.

5.3.2 Sonication result

During all ablations, the temperature at the foci was monitored by MR thermometry in real-time. With the same ultrasound protocol (sonication duration: 25s; acoustic power:

20W), an average temperature of 55 ℃ was reached at the ultrasound foci which was sufficient for causing protein denaturation in the egg-white gel phantom.

The photographs of the egg-white phantom corresponding to the MR images were taken after the ablation (Figure 5.14). Since the two sonication patterns were both with 3-layers structure, some of the photographs were taken after the phantom had been sliced in order to observe the inner layout of the lesions (Figure 5.11). The lesions in the phantom were scanned in two directions, one perpendicular to the axis of the US beam and the other parallel to it.

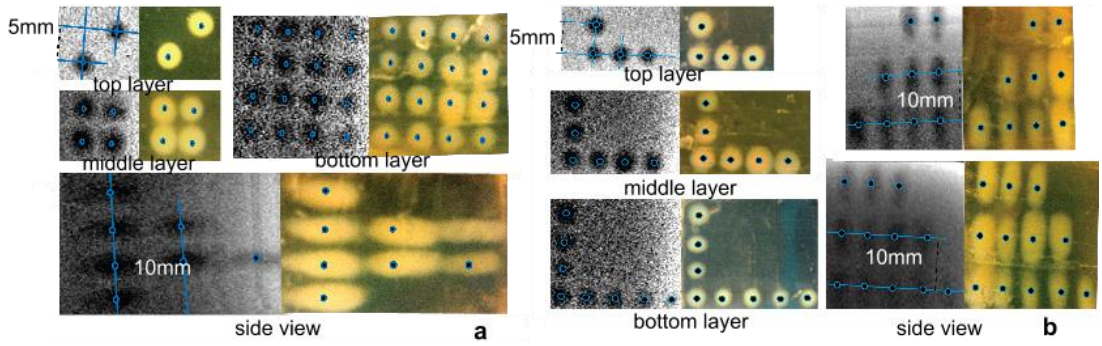

Figure 5.14 The photography of the lesions and corresponding enlarged section of post-FUS MR scans after image enhancement using ImageJ. Some of the lesions in the photograph did not match exactly to the MR images because the slicing position of the phantom did not coincide with the corresponding MR scan position. (a) The lesions were distributed in a 3-layers square pattern; (b) The lesions were distributed in a 3-layers L-shape pattern.

The results of the phantom ablation experiments are summarized (Table 5-2) to evaluate the applicability of the active tracking assisted robotic arm setup, in which the accuracy of the lesion positions as well as the lesion dimensions are demonstrated. The distance errors between the calculated centre of the lesion and the theoretical position recorded from the micro-coils were Δx=0.3±0.27mm, Δy=0.3±0.26mm and Δz=0.8±0.74mm respectively in the coordinate system of the application module on the robot, where the *x*, *y* directions were vertical to the axis of the US beam; z directions was along the US beam. The z direction was along the layered direction parallel to the coronal direction of the MRI bore (Figure 5.11). We found that the distance errors of the lesions in *z*

direction were greater than in the other two directions, which might because that the length of the lesions varied more when the MR scan plane was mal-positioned from the axis of the lesions.

Table 5-2 Results of the phantom ablation experiments for the setup. (Δz means the distance error in the US beam axis direction, approximately parallel to the coronal direction of MR scanner; Δx and Δy are the distance errors in the direction perpendicular to the US beam axis; d_{rad} and d_{axial} are the minor and major diameter of the elliptic lesions in the side view.)

Ablation series	Δx (mm)	Δy (mm)	Δz (mm)	d_{rad} (mm)	L (mm)
L-shaped distribution	0.4±0.27	0.3±0.26	0.8±0.74	3.0±0.23	5.8±0.30
Square-shaped distribution	0.4±0.37	0.4±0.28	0.7±0.66	3.0±0.18	6.0±0.36
All	0.4±0.27	0.4±0.23	0.8±0.64	3.0±0.20	5.8±0.36

The error for the active tracking was not considered because the readout from the micro-coils was taken as the theoretical positions of the robotic arm. The deviation of active tracking was 0.01mm which means there was a small fluctuation during the monitoring process of the robotic arm. The deviation value was calculated by repeating twenty measurements for every ablation position. It was supposed to increase if the focal scanning volume became large.

5.4 Summary and discussions

In this work, a combination of a commercial available robotic arm, a bowl shaped fixed single focus FUS transducer and a customized active tracking device was proposed for MRgFUS therapy. The active tracking implementation was calibrated and a series of phantom ablation experiments was conducted, from which the localization accuracy and applicability for MRgFUS of this combined setup were assessed.

An application based on RTHawk communicated with the GE MR scanner in real-time and the coordinates of the robotic arm were monitored and recorded. Furthermore, the position and gesture of the robotic arm were reconstructed in a virtual 3D space where the phantom/tissue position also was included. With the in-house developed software, the active tracking obtained the device position within 120 milliseconds. By employing three phased dithering direction rather than six, the tracking time could be reduced to 60 milliseconds, which satisfies tracking applications in a smaller volume. The tracking was repeated for over 20 times at each reference position, and the deviation was around 0.07 mm in the whole calibration area, which indicated a high robustness of this method.

The robotic arm was remotely controlled by a service software extension provided by the manufacturer. This allowed for stepwise relative mechanical movements of the distal application module only. The system internal optical encoders of the robotic arm measured the movement steps at the pneumatic actuators for corresponding DOFs, but the minor transformation caused by the loads was not included in the measurement. Therefore we used a rigid reference phantom rather than the system optical sensors to provide reference points for assessing the active tracking technique in the calibration experiment.

As afore mentioned, the tracking distance errors in the coronal direction were generally greater than the errors in the other two directions. The systematic error might come from two reasons. Firstly, when needle anchor touched the bottom of the reference holes, the elastic phantom might deform a little in the coronal direction. Secondly, because the position of the needle anchor had to be confirmed using MR images, which made the calibration a time consuming process, the agar reference phantom deformed more in the coronal direction than in the other directions because of self-weight. To evaluate the active tracking more precisely, a more rigid gel reference phantom or mechanical reference component should be designed in the future. Besides the orientation dependence, the distance errors were found to increase when the micro-coils were far from the iso-centre because of magnetic gradient inhomogeneities (Kuhl et al., 2007). So the design of using multiple coils to construct a rigid-body is preferable rather than using single marker since the distance errors were eliminated to a certain extent among multiple markers.

The application module of the robotic arm could reach a FOV of about 50 cm×50 cm, yet the active tracking was not calibrated in the whole spatial range. Partly because the receive coil has a size of 10 cm×10 cm. Furthermore the robotic arm has to reach some limited positions of the FOV in an extremely oblique gesture. This made it difficult to insert the needle anchor into the reference holes of the gel phantom because the trajectory of the insertion operation is unpredictable at these limited positions. Considering the above restrictions, the calibration experiment had only evaluated the active tracking techniques in an acceptable spatial range of 160 mm×160 mm×140 mm (sagittal, axial and coronal directions respectively) for future uses. A similar active tracking had been done in axial direction with a range of -150 mm ~150 mm which did not exceed 3 mm (Zimmermann et al., 2006). By employing larger receive coil, a larger range could be calibrated similarly.

Passive marker is characterized by various imaging or post-processing methods (de Oliveira et al., 2008, Flask et al., 2001, Thormer et al., 2012, Rea et al., 2009), our presented active tracking is competitive to passive marker. Most of errors are distributed smaller than 1 mm for both of these two methods. But the advantage of active tracking method in this study is that it provides a much faster speed for device localization.

In this study, for the positive distance errors, which in theory are not normal distribution, we prefer to use RMS and CI such as 90% or 95% to describe the result. RMS error has the advantage of incorporating both the trueness and precision in a single value as$RMS \approx \sqrt{\mu^2 + \sigma^2}$. CI indicates the results more clear when there are larger errors in the distribution tails which could be easily omitted if using deviation to describe.

Based on the active tracking guidance, the robotic arm moved a MR compatible single-element HIFU transducer to finish two ablation patterns in egg-white gel phantoms. By investigating the two post-FUS ablation patterns based on T2-weighted MR scan using ImageJ, the focal scanning accuracy was calculated. Calculation had not been done according to the photography since the slicing cannot be guaranteed through the centres of all the lesions and the camera had not been calibrated properly. Compared to the errors of using passive tracking for the same robotic arm to guide sonication in phantom (Krafft et al., 2010), which is 0.5±0.4 mm and 0.9±0.6 mm vertical and parallel to the

coronal direction in the MRI bore, the final lesion location distance errors using active tracking had similar performance.

The lesion location distance errors are larger than the tracking distance results in the relative direction. Firstly because the FUS transducer was heavier than the needle anchor, the connection between the FUS transducer and the robotic arm was not kept in a perfectly rigid relation during focal scanning. Another reason for the deviation is the inhomogeneities of the egg-white gel phantom. By investigating the MR scans and photographs of the post-FUS phantoms, the sizes of the lesions varied a lot, which demonstrates the influence of the different US absorptions in different areas of the phantom. The shapes of the lesions were also different from the theoretic shape of the acoustic focus of the characterized US transducer. The inhomogeneity is supposed to behave more obviously *in vivo* if animal or human tissues are to be used for the ablation experiments. Considering that the lesions were with diameters of around 3 mm and lengths of about 6 mm, the precision of focal relocation was sufficient for focal scanning large tumours.

The ablation experiments mainly focused on evaluating the active techniques for robotic arm assisted MRgFUS, only degassed water was used for coupling the US transducer with the phantom. However, a new treatment unit should be developed which allows for the transducer to cling on the skin surface, if the setup need to be tested on human or animal tissues, The US transducer should be embedded in a water-filled bellow, which could be fixed on to the skin via stretchable straps (Krafft et al., 2010). For example, the ExAblate 2100 system (InSightec, Ltd., Tirat Carmel, Israel) uses a strong membrane to restrict degassed water within the treatment range which is used for coupling the ultrasound with tissue. By designing a new treatment unit with water-bellow, the setup could be applied for animal or human tissue ablations.

The active tracking sequence and thermometry sequence could alternate each other to enable real-time localization of the device and treatment monitoring (Andrew B. Holbrook, 01/2012). This implementation allows the combined robotic system to fast adjust the US focus even during sonication because both the active tracking and MR thermometry scans are not very time consuming.

The combination of this active tracking assisted robotic system and the ExAblate 2100 system is fascinating. This might make the utmost of large operational range of the robotic arm with active tracking and flexible treatment access of the portable US transducer. Furthermore, after combining relatively slow focal scanning of the robotic arm and the fast beam-steering of the phased-array US transducer, the problems caused by patient involuntary motion are possible to be solved. The robotic arm will relocate the US transducer if the patient motion exceeds a certain range, and the phased-array US transducer will steer the focus electronically if the movements are too fast for mechanical relocation.

5.5 Conclusion

To conclude, active tracking was developed to monitor the position of a robotic arm with an acceptable accuracy at a sub-second update rates. The integration of active tracking technique and robotic arm has the potential to guide a FUS transducer to deliver ablations in a wide range quickly. With the in-house developed software, the US focus repositioning can be controlled with an accuracy of less than 1mm. The calibration of active tracking and phantom ablation experiments assessed the feasibility of this combined system for MRgFUS which made this setup competitive with beam-steering technique of phased-array FUS.

Furthermore, the integration of fast localization method and the MR robotic arm plays an important role in the next chapter, which mainly focus on target motion tracking realized by a multi-phased FUS transducer. The robotic arm is a key setup for providing target motion, which mimics the liver motion caused by human breath.

Chapter 6 Motion tracking in MRgFUS

6.1 Introduction

In this chapter, the issues of human liver motion tracking in MRgFUS are investigated. First of all, by analyzing the MRI image stream obtained from volunteers, the basic properties of the human livers motion when they are breathing freely are summarized. Based on these properties, a tissue mimicking phantom was fabricated in order to produce similar graphic situations in the MRI scans. Using the robotic arm mentioned in chapter 5, a moving phantom is built to investigate MRgFUS for motion tracking. Moreover, an MR video processing method is developed to track a moving target area in the MRI stream. A phased-array HIFU transducer is used to realize beam-steering in this chapter. With all mentioned above, the idea of MRgFUS for moving target is going to be examined.

6.2 Motion simulator fabrication and tracking algorithm

6.2.1 Liver motion parameters

Healthy volunteers were recruited in a research study which was fully approved by East of Scotland Research Ethics Committee and sponsored by the University of Dundee. Two healthy volunteers were scanned via MR scanner (Signa HDxt, GE Medical Systems, Waukesha, WI, USA) to estimate the liver motion parameters. Fast spin echo images (TE/TR=1.2/3.8 ms, flip angle=60°, thickness=5.0 mm, FOV=22cm×22cm) were acquired every 200 milliseconds in the sagittal direction while the volunteers laid supine and breathed ordinarily. The features in the image are different from what they look like in ultrasound scans (Figure 3.1). In the ultrasound B-mode scans, the cross-section view of the tumour area has a clear difference from its surrounding healthy tissues, which is usually with round shape and it is selected as the target area to be tracked in image processing algorithm. However, in MR scans, the cross-section view of blood vessels appears to be brighter than surrounding area. These vessels can be selected as landmarks to be tracked over the scan series, as shown in Figure 6.1. Motions were analysed in AP and SI directions, while the motion along LR direction

was ignored since they are not as serious as in the other two directions (Park et al., 2012).

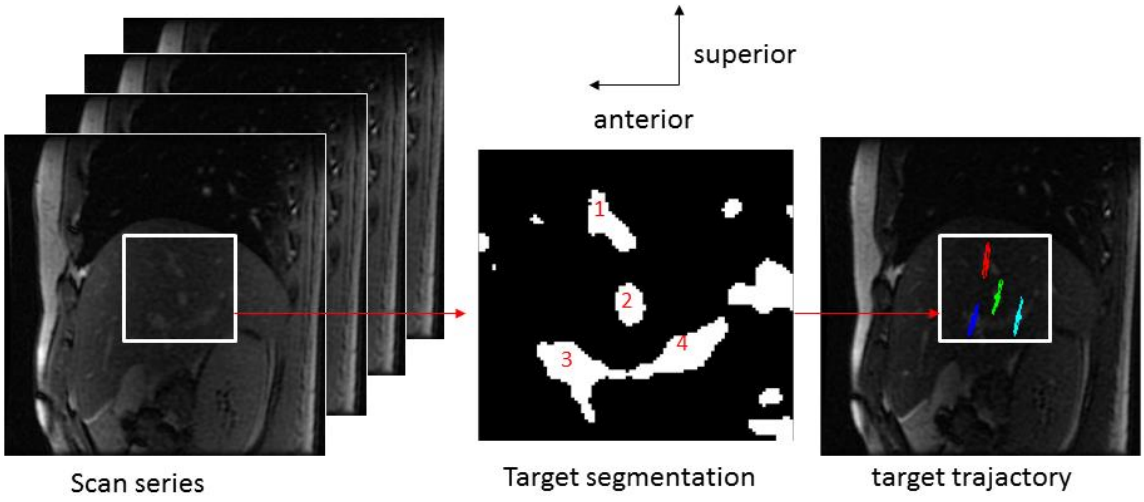

Figure 6.1 MR scans of a volunteer liver in free breathing state. The interested area was cropped and segmented for all the frames via ImageJ. Several vessels were selected as the targets to track (for this volunteer, they were listed from number 1~4). The right overlayed imaged was the motion range of the four vessels.

A segmentation algorithm (ImageJ) was implemented for all the frames. After thresholding and particle tracking, the positions of the vessels (markers) over time were tracked from the MR scan series (Figure 6.1). As shown in Figure 6.2, by averaging the tracking results of all the vessels in one volunteer's liver, the displacement of the liver along the SI and AP directions over time was displayed as a near sine wave trajectory. The average of maximum displacement was 28.25 mm and 8.0 mm respectively in the two directions.

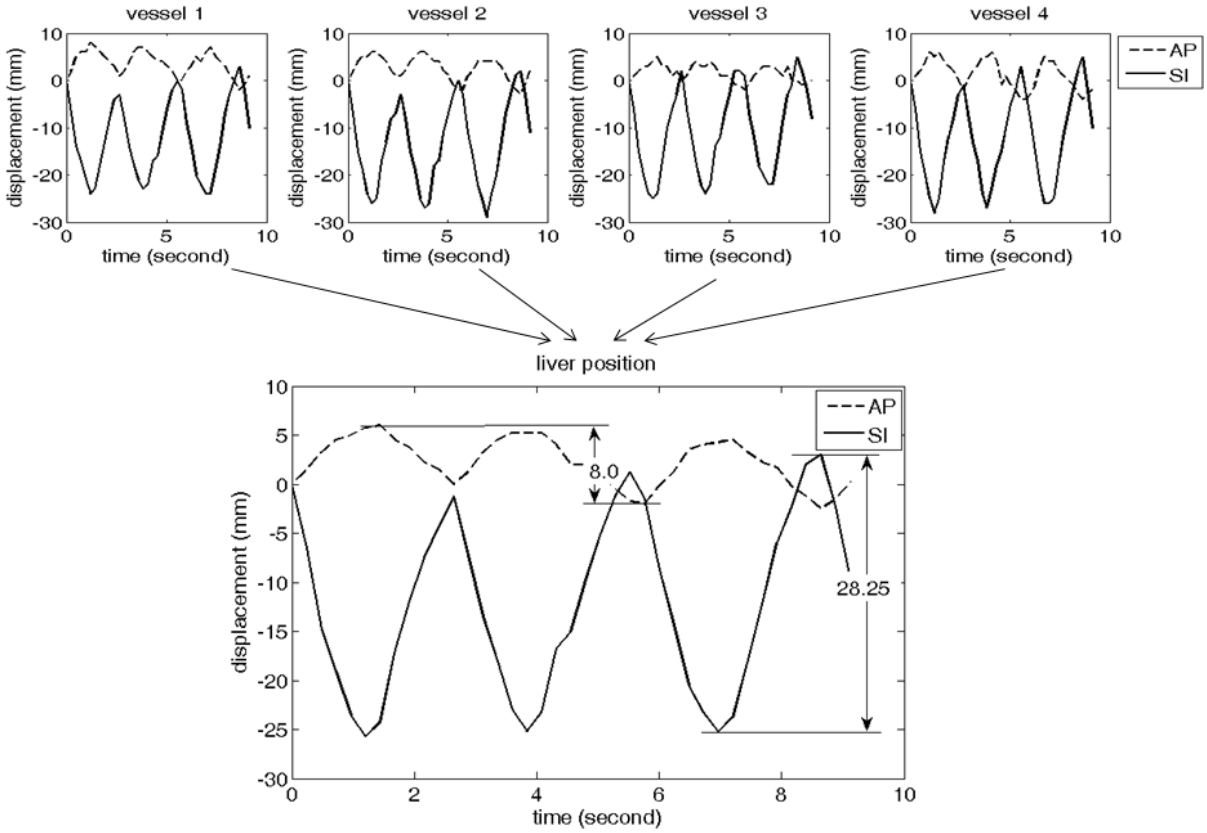

Figure 6.2 Liver displacement in superior/inferior and anterior/posterior directions of one volunteer. The bottom graph was an averaged result from the four tracked vessels (markers).

For scans of the two volunteers, the averaged displacement ranges were 19.9 mm (12.0~27.0 mm) and 7.88 mm (6.30~8.86 mm) along SI and AP directions respectively. The respiratory frequency range was from 0.26~0.40 Hz.

Although an overview of how free breathing influence the position of the human liver could be obtained from the volunteer data, the data is patient specific and is not repeatable. An experimental motion setup was needed to reproduce movements for testing motion tracking algorithm and furthermore to test focused ultrasound ablation during target motion..

6.2.2 Phantom fabrication mimicking human liver

An agar (2.5% g/ml) phantom was fabricated to mimic the human liver in the free breath state. It should produce similar structure features in a fast MR scans. The phantom has a two layers structure, with the inner part winded by a plastic tube. The two ends of the tube were left out of the phantom, which connected to a pump. In order to make use of the imaging property of vessels, EPI (TE/TR=10.3/100ms, flip angle=60 °, FOV=22cm×22cm) was chosen to scan the phantom (DeLaPaz, 1994). With a steady flow of 400 mL/min, the transverse section of the tubes appeared to be brighter than the other part of the phantom in the MR images (Figure 6.3). These mimicking structures of bright vessel were used as markers for motion tracking. The EPI scan is also less susceptible by the tissue motion than other sequences because of its fast scanning property. In Figure 6.3, the EPI scan can achieve a frame rate faster than 2.3 frames per second. If the image quality can be satisfied more or the FOV can be decreased, the scanning speed can achieve ten frames per second or even more.

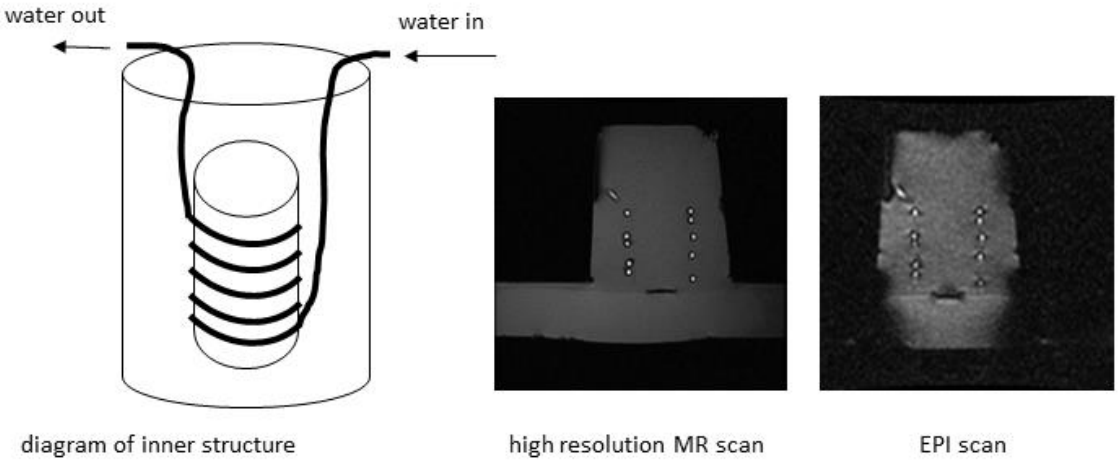

Figure 6.3 Liver mimicking phantom structure (left). Inner part was winded with a tube with water flow to simulate blood flow (400 mL/min). FSPGR scan (TE/TR=6.9ms/200ms, flip angle=60 °, FOV=22cm×22cm) as a calibration view (Middle). Fast EPI (TE/TR= 10.3/100 ms, flip angle=60 °, FOV=22cm×22cm) were to be used to track the phantom position (Right). The vessels mimicking structure appeared brighter than the background.

The INNOMOTION robotic arm provided phantom motion, as shown in Figure 6.4. The MR compatible robotic arm guided the phantom to move back and forth along the axial direction of the MR scanner. In order to simplify this setup, only the respiratory motion in superior-inferior direction was taken account, the motion in LR and AP was ignored. The precision of the localization of the robot was guaranteed higher than 1.0 mm. So the phantom movement was highly reproducible for testing tracking algorithms.

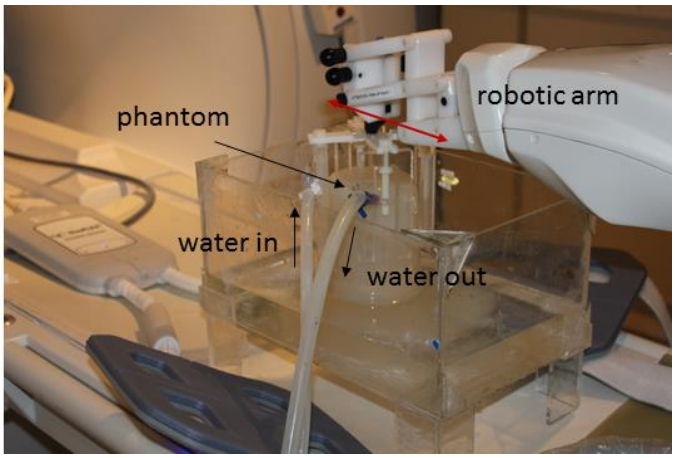

Figure 6.4 Liver phantom was moved back and forth by a MR compatible robot along axial direction. The phantom was with 400 mL/min water perfusion to mimic blood flow in human livers and increase image contrast in MR EPI scans.

6.2.3 Tracking algorithm

The tracking progress is based on image processing from the MR scan results (Figure 6.3). Because the transverse section of the vessels appears to be bright, they are selected as the markers to demonstrate the movement of the whole liver. The locations of these landmarks are calculated continuously to determine 2D position of the liver. Figure 6.5 shows a typical set of MR EPI scan of the moving target phantom. In this series, the target phantom was moved 40mm along axial direction in the MR coordinate system.

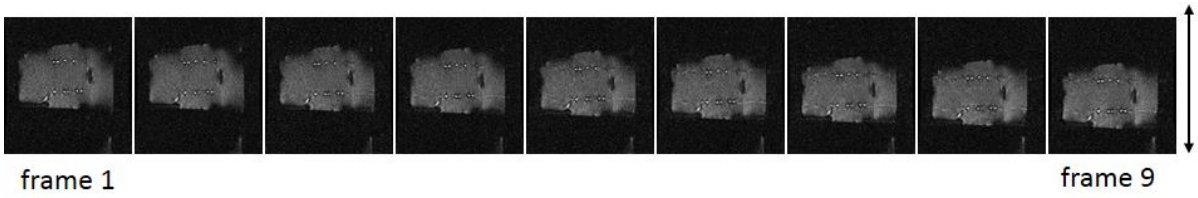

Figure 6.5 A series of MR EPI scan of a specially designed phantom. The phantom was moved by a distance of 40mm along axial direction (double arrow line).

The first step is to select the markers from the brightest areas, as shown in Figure 6.6. During the motion, the target to be tracked is highly to have out-of-plane motion even in a controlled movement. Therefore, the long shaped marker which represents a segment of the vessel is easy to be lost in other image frames because it might be only visible in the current MR scan plane. As shown in Figure 6.6, the elliptical bright areas are defined for tracking purpose, since they represent a transverse section of a segment of the vessel and are not susceptible to the out-of-plane motion. Areas which look similar to the vessel but without high enough intensity are also given up since they might represent vessel tips which might also disappear in other frames.

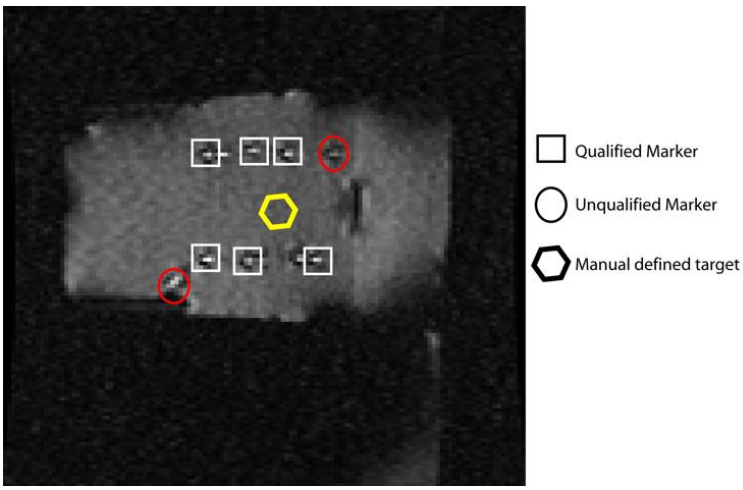

Figure 6.6 A sampled phantom MR scanning result. The brightest areas were selected as the markers to be tracked. Areas in rectangles are the defined markers, areas in circles are the unqualified markers because of the shape or the pixel intensity. Area in a hexagon represents the manual defined target area to be tracked. The elliptical shaped markers are selected as landmarks for tracking because they normally can keep their relative position relationship to the whole liver when out-of-plane motion happens.

All the landmark positions in one frame would be calculated first. Based on all the landmark positions, the defined target area (Figure 6.6) could be obtained by calculating the vectors between the defined target area and the landmark positions in the first frame.

First of all, the method for calculating the position for individual landmark position is by analyzing the cross correlation map (CCM) between the current image and the landmark image to be tracked. The 2D cross correlation of an image matrix L (size: P, Q) and an image matrix F (size: M, N) is an image matrix C (size: M+P-1, N+Q-1), which is given by

$$C(k,l) = \sum_{m=0}^{M-1}\sum_{n=0}^{N-1} F(m,n)\cdot L(m-k,n-l), \begin{matrix} -(P-1) \le k \le M-1 \\ -(Q-1) \le l \le N-1 \end{matrix} \quad 6.1$$

Suppose the first input matrix (current frame) represents an image and is defined as *I1*, the values represent the pixel intensity in *I1*. The second input matrix represents the landmark image. They are defined as in Figure 6.7

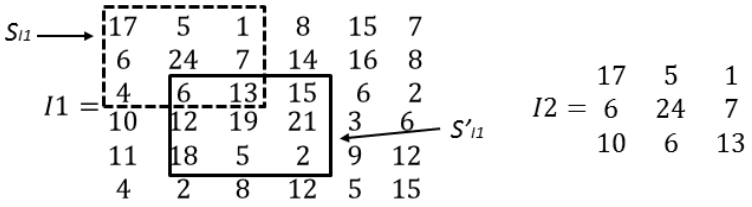

Figure 6.7 CCM algorithm principle. *I1* represents current frame, *I2* represents the landmark image, the algorithm is to find where the *I2* happens in *I1*.

In CCM, the value of the output element is computed as a weighted sum of neighboring elements. For example, the (1, 1) output element from the cross correlation is the dot product of *I2* with S_{I1}, which is

$$dot(S_{I1}, I2) = 17\cdot 17 + 5\cdot 5 + 1\cdot 1 + 6\cdot 6 + 24\cdot 24$$
$$+7\cdot 7 + 10\cdot 10 + 6\cdot 6 + 13\cdot 13 = 1281$$

The normalized cross correlation of the output element is

$$1281/(\sum \|S_{I1}\|^2 * \sum \|I2\|^2) = 1.0$$

Similarly, when we compute the (3, 2) output element of the CCM, the normalized cross correlation is

$$dot(S'_{I1}, I2)/(\sum \|S'_{I1}\|^2 * \sum \|I2\|^2) = 0.73$$

Where S'_{I1} is labelled in Figure 6.7.

The above case confirms that when a small matrix image is identical to a section in the area in another matrix image, the cross correlation achieves its maximum value 1.0. The more similar are the matrix to another section, the higher the cross correlation value is. Here because 1>0.73, means that the possibility of landmark *I2* happens at the position of (1, 1) in current image *I1* is higher than at the position of (3, 2) in *I1*.

The theory is clear in Figure 6.8. The CCM of a 4-by-4 matrix (landmark image) and current 68-by-41 frame matrix is an image matrix of size 71-by-44. The peak intensity is found at position (10, 50) in the CCM, after deducting it by the size of the 4-by-4 landmark matrix, the result (6, 46) is where the position of the landmark is in the current frame matrix. The generalized formula is

$$Position\ of\ Landmark = Position\ of\ peak\ in\ correlation\ map - Size\ of\ landmark$$

During tracking, a CCM is calculated over a search patch around each landmark between the frame k and its previous frame k-1. The average shift of all the landmarks is taken as the displacement of the whole phantom. In this way, the target phantom is tracked continuously for each slice.

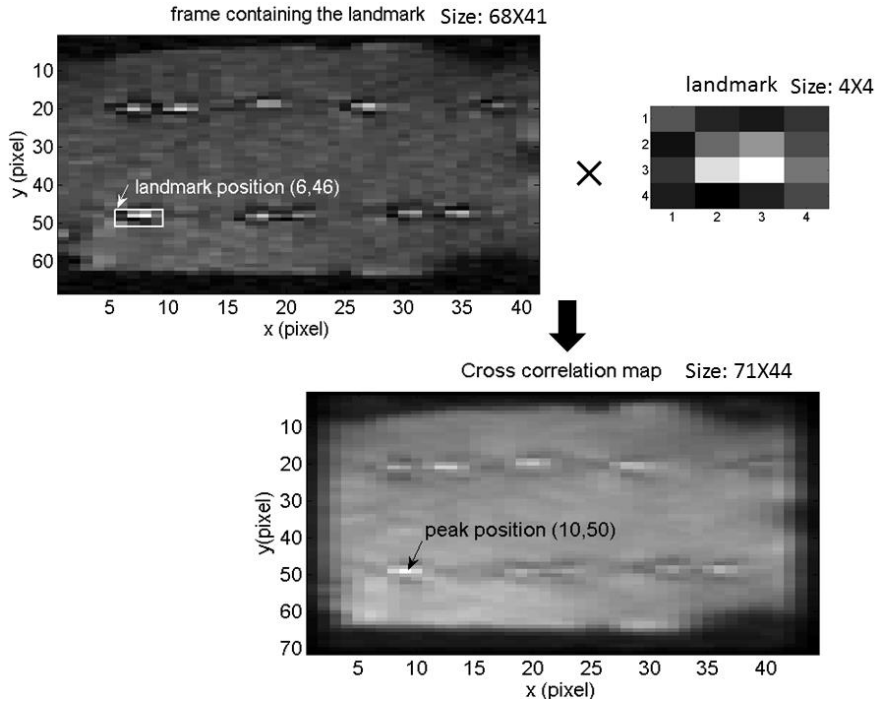

Figure 6.8 Diagram of locating each landmark in a frame. In the CCM of one frame and the cropped landmark area, the position of the peak pixel corresponds to the 2D coordinates of the landmark in this frame.

The tracking method was tested based on the setup shown in Figure 6.9. The target phantom was moved back and forth via INNOMOTION robot arm (Figure 6.4). Its position could be monitored by the optical sensor system of the robotic arm. These monitoring records were used to evaluate the performance of the tracking algorithm including its precision and speed.

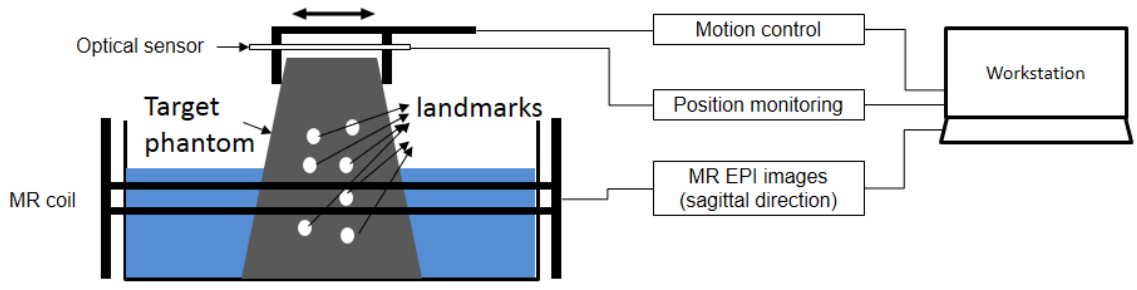

Figure 6.9 Diagram of setup for testing motion tracking algorithm. The robot position could be controlled to move and its position could be monitored by its built-in optical encoder system. This monitoring result will be used to evaluate the performance of the tracking algorithm.

Series of movement distances with different speeds were carefully controlled via the robotic arm. As shown in Figure 6.10, the movement ranges of the target phantom include 10mm, 20mm, 30mm, and 40mm, their speeds were also different from each other (from 2mm/s to 6 mm/s). The position of the robotic arm could be monitored with an accuracy of 1.0mm and an update speed of 100 frames per second. Therefore, it is fast enough for evaluating the tracking algorithm since the updated rate of the MR EPI images is only 2.3 frames per second in the experiment. For each motion range, the tracking was repeated three times.

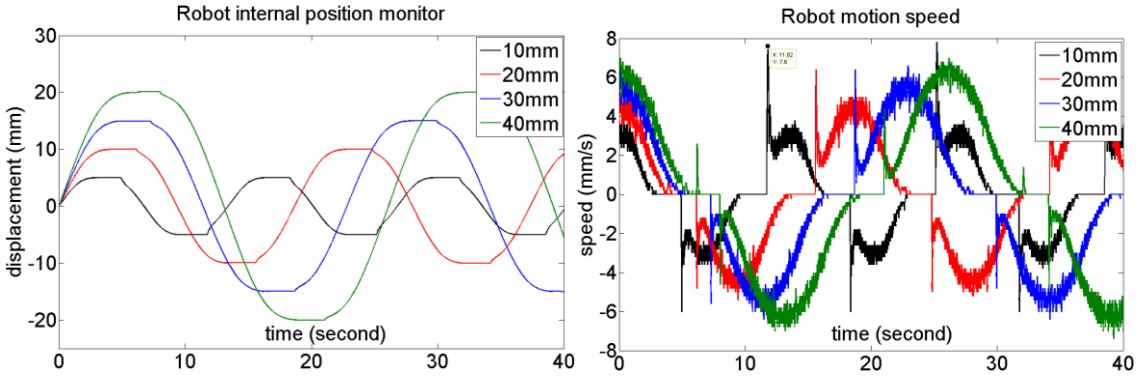

Figure 6.10 System internal optical sensor system monitored the robot position (left). Their relevant motion speeds were also calculated accordingly (right). These data were used to evaluate the tracking performance of the algorithm.

6.3 Synchronization between target motion and beam-steering

6.3.1 Phased-array transducer for beam-steering

The fast focus repositioning was implemented by using ExAblate 2100 conformal bone system (CBS) (Insightec Ltd., Tirat, Isreal), which is designed for MR guided treatment of bone metastasis. More than 1000 transducer elements were distributed in a square shape in the ExAblate 2100 system, as shown in Figure 6.11, which allows flexible focus repositioning during the FUS procedure. Good acoustic coupling is provided with the water-permeable membrane and inner water cycling is embedded to the system to accelerate the skin cooling during focused ultrasound ablation.

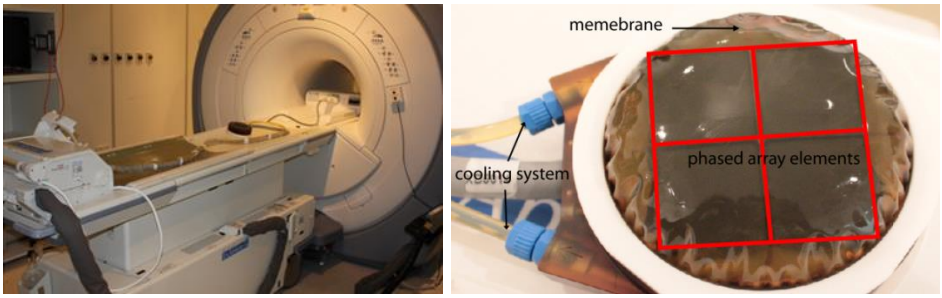

Figure 6.11 Exablate 2100 system: patient table (left), multi-elements distributed in a square shape (right).

The hardware restriction which has to be taken account for the fast beam-steering is that the CBS transducer is performing a step-by-step sonication to approximate a continuous beam-steering. For example, in Figure 6.12, if a target is moving in a linear range of 10 mm, the whole range is distributed averagely into five local sonications, one local sonication covers a range of 2 mm. The focus of the ultrasound beam stays still at the same position if the target moves within the range of 2 mm. However, the focus will shift to another position when the target moves into the next range, say 2 mm~4 mm. This restriction will approximate the theoretical continuously beam-steering to a step-by-step beam-steering. The influence of this restriction will be discussed in the result section.

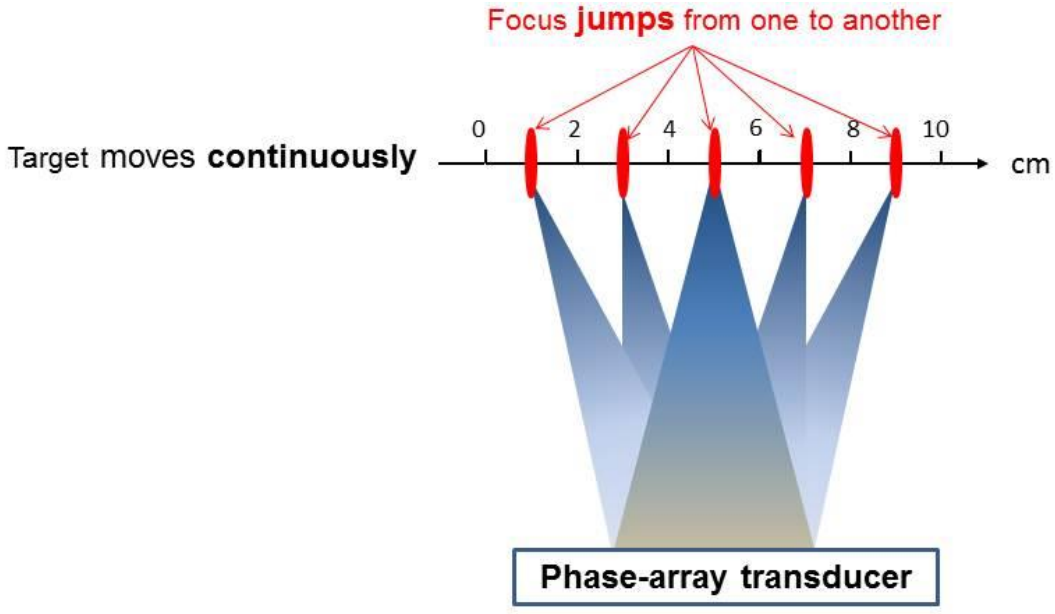

Figure 6.12 Local sonication principle. The focus of ultrasound beam is jumping from one position to another to approximate continuous beam-steering. The distance between two local sonications is predefined. The focus of ultrasound stays still at the first position (from left to right) if the target only moves in the range 0-2 mm. The shorter the distance between local sonications, the more similar this method is to continuous beam-steering.

6.3.2 Phantom fabrication with thermometer embedded

In order to precisely monitor the temperature rise at the target area, an optical thermometer (FOTEMP 4, OPTOcon-AG, Germany) was embedded into the phantom. The thermometer was used to monitor the temperature rise with a frame rate of two frames per second in this work. The probes used were total non-metallic material to meet the MR compatibility and safety requirements. The diameter of the tip is 1.3 mm, a small tube containing MR contrast agents (Gadolinium doped in water with 1:100 mL/mL) was attached with the thermometer head end to improve its visibility in the MR images (Figure 6.13). In the T1-weighted fast Gradient echo image, the tip of the thermometer could be clearly selected from background signal. This area close to the tip was selected as the target for the focused ultrasound ablation.

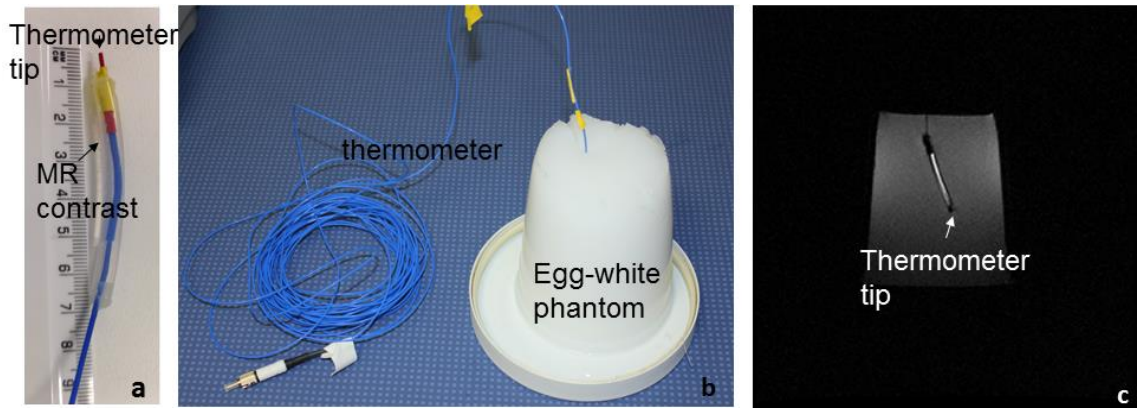

Figure 6.13 PAA egg-white phantom with merged thermometer. MR contrast agents are used to optimize the visibility of the tip of the thermometer. a) thermometer with MR contrast agent; b) thermometer is merged in phantom; c) how the thermometer and the phantom looks like in MR scans

6.3.3 Synchronization setup and algorithm

The beam-steering sonication system was setup including the INNOMOTION robotic arm system, the MR scanner, an optical thermometer, and the ExAblate 2100 system. The INNOMOTION robotic arm was used to guide the PAA phantom in a back and forth movement pattern along z-axis (axial direction in MR frame). The coordinates of the robotic arm were obtained via the active tracking method, which was detailed in chapter 5. The optical thermometer was used to monitor the temperature rise of which the tip is taken as the ablation target area. The ExAblate 2100 system was used to produce the ablation, with advanced beam-steering function. The connection between these devices is shown in Figure 6.14. All these systems are integrated via an MATLAB programme.

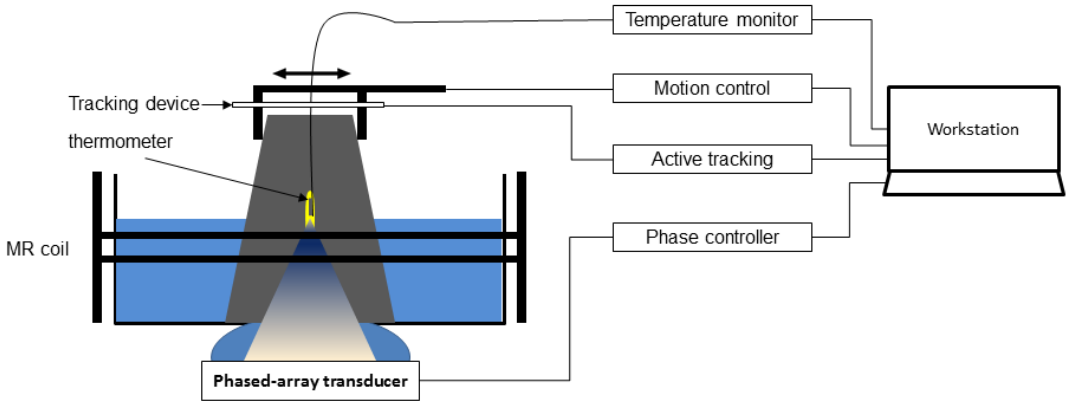

Figure 6.14 Diagram of the beam-steering sonication setup

As shown in Figure 6.15, the fluid container was fabricated to provide a space to realize beam-steering and phantom motion. There is a membrane window at the bottom of the container to allow focused ultrasound beam to penetrate. If necessary, the phantom can be moved along the axial direction in a range of 200 mm. An interventional coil (8channel, 24 cm, Duoflex, USA) was wrapped around the container that can cover the motion range of the PAA phantom. The phantom was then positioned in the container filled with a tissue equivalent gel (water, 1.23g/L NaCl, 10g/L polyacrylic acid partial sodium salt (Sigma-Aldrich Corp., Saint Louis, Missouri, USA)) (ASTM, 2010) which mimicked the viscous atmosphere in the abdomen.

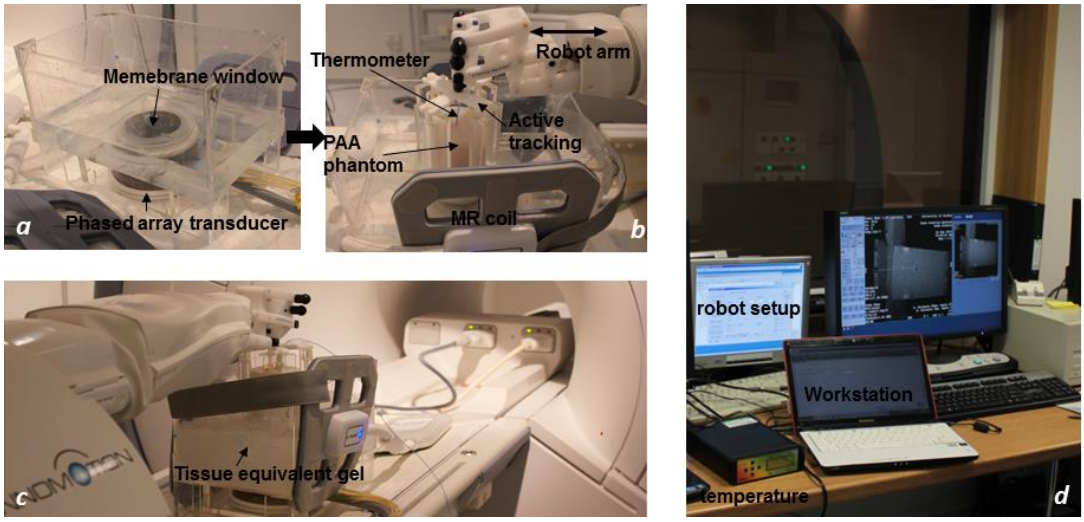

Figure 6.15 Photo of synchronization experiment setup in the MR suite. a-c) indicate the process of the experiment setup; d) is the software system including detection of robot position, beam-steering control and temperature monitor.

The coordinates of the target in the MR frame should be translated to a position in the HIFU transducer frame. For example, if the movement range of the phantom is L mm, 3 series of high resolution MR scan were performed when the target phantom was at the position of $-L/2$, 0, $L/2$ mm in via the robotic arm. The coordinates of the target area were measured in the coordinate system of MR scanner (Figure 6.16). They were expressed as $(x_{MR}, y_{MR}, z_{MR})_i$, where $i = 1, 2, 3$, represents the position –L/2, 0, L/2 respectively.

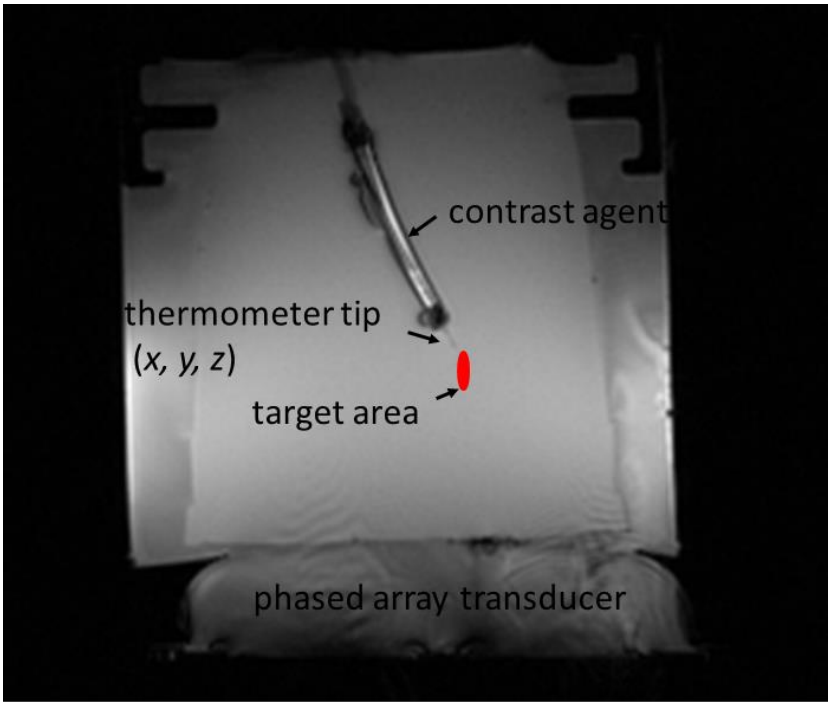

Figure 6.16 Phantom, thermometer tip and HIFU transducer in MR scan (Fast GRE, TE/TR=6.9/100 millisecond, FOV=21×21, thickness=5 mm, Resolution=256×256). The focus was a bit lower than the tip of the thermometer. The target area position in the MR coordinate system was measured.

And then their locations in the coordinate system of the HIFU transducer were calculated according to 3D transformation equation.

$$\begin{bmatrix} x_{FUS} \\ y_{FUS} \\ z_{FUS} \end{bmatrix} = R \cdot \begin{bmatrix} x_{MR} \\ y_{MR} \\ z_{MR} \end{bmatrix} + T \qquad 6.2$$

R is a rotation matrix and T is a translation vector between the MR coordinate system and the HIFU transducer coordinate system. They are calculated before the experiment. With this, a look-up table between three key positions (maximum, minimum and zero) of target phantom and the positions to be ablated in the transducer coordinates system was built (Table 6-1).

Assuming that the robotic arm displacement would linearly correlate with the target phantom displacement, a 2D trajectory interpolation was performed to reduce the total

number of measurements. Thus, the more discrete look-up table was built to produce the series of step local sonication to approximate a continuous beam-steering (Figure 6.12).

Table 6-1 Look-up table between the target phantom positions and the focus to be created by the HIFU transducer, *L* is the phantom movement range, phantom was moved to –*L*/2, 0, *L*/2 via the robotic arm and these 3 key positions were translated to the HIFU transducer coordinate system. *n* is the interpolation number.

Target phantom positions	Positions to be ablated (HIFU transducer)		
(robotic arm)	x	y	z
$-L/2$	$x_{-L/2}$	$y_{-L/2}$	$z_{-L/2}$
$L(-1/2+1/n)$	$x_{L(-1/2+1/n)}$	$y_{L(-1/2+1/n)}$	$z_{L(-1/2+1/n)}$
⋮	⋮	⋮	⋮
0	x_0	y_0	z_0
⋮	⋮	⋮	⋮
$L(-1/2+(n-1)/n)$	$x_{L(-1/2+(n-1)/n)}$	$y_{L(-1/2+(n-1)/n)}$	$z_{(-1/2+(n-1)/n)}$
$L/2$	$x_{L/2}$	$y_{L/2}$	$z_{L/2}$

As shown in Figure 6.12, the phased-array transducer used a step local sonication to mimic continuous beam-steering. When the robotic arm had a deviation E from its '0' position, assuming it is at $L/2-L/n<E<L/2$ (n is the interpolation number), the deviation E was approximated to its closest value in the left column, say $L/2-L/n$ or $L/2$, and its corresponding coordinates in the HIFU transducer frame was found accordingly. Then the focus position was switched in real-time by the phased-array transducer. As the robotic arm was moving continuously back and forth, the FUS transducer would perform a continuous sonication along with this movement.

As shown in Figure 6.17, three conditions were tested to investigate the differences in temperature rises among when 1) no motion target and no tracking, 2) motion target but without tracking, and 3) motion target with tracking. The aimed target area was the same for all the situations, which was 1-2 mm lower than the tip of the thermometer but as close to it as possible. In all the situations, the same protocol of 20W (electrical power) for 40 seconds was used to ablate the target area. It was at a continuous mode with central frequency of 0.55MHz. This HIFU transducer is with no acoustic output measurements since it is not possible to merge the transducer into water. However, the power used in this study stayed the same, so this study could be taken as a preliminary (nonquantitative) study.

Between successive sonications, a time delay of at least five minutes was necessary for the target area to cool down to normal temperature (about 20 ℃ in this experiment) to prevent the phased-array transducer from overheat. For the motion with beam-steering situation, the robot motion range was set to be 10 mm and 20 mm (L= 10 mm, and 20 mm) to evaluate whether different motion ranges influence the tracking performance or not. The number of local sonications for 10mm range and 20mm range was to be 6, and 11, respectively, which means, a local sonication covered a target motion range of 2mm.

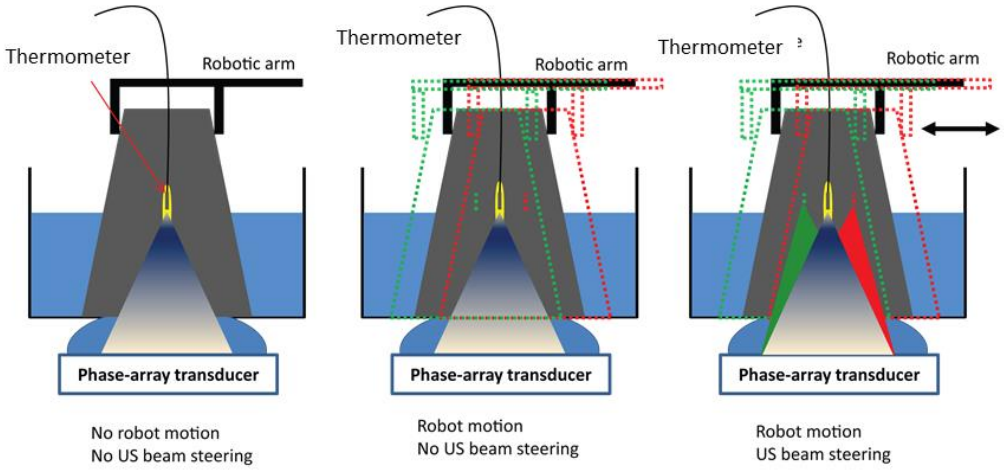

Figure 6.17 Phantom sonication, thermometer is used to monitor the temperature. left is a static sonication as a reference; middle is static sonication when the robot moves the phantom back and forth; right one is beam following the target motion.

6.4 Results

6.4.1 Tracking precision

As shown in Figure 6.18, the tracked coordinate and the position recorded by the system internal monitor are depicted in the same diagram. From these example diagrams, it seems that the tracking results fit well to the recorded positions of the target phantom. The time for calculating the shift between two frames was less than 10ms, which could be ignored comparing to the image acquisition time for one frame of MR EPI scan with its maximum achievable speed (100ms/frame) in this situation. Continuous position information could be calculated from the landmark positions via 2D interpolation.

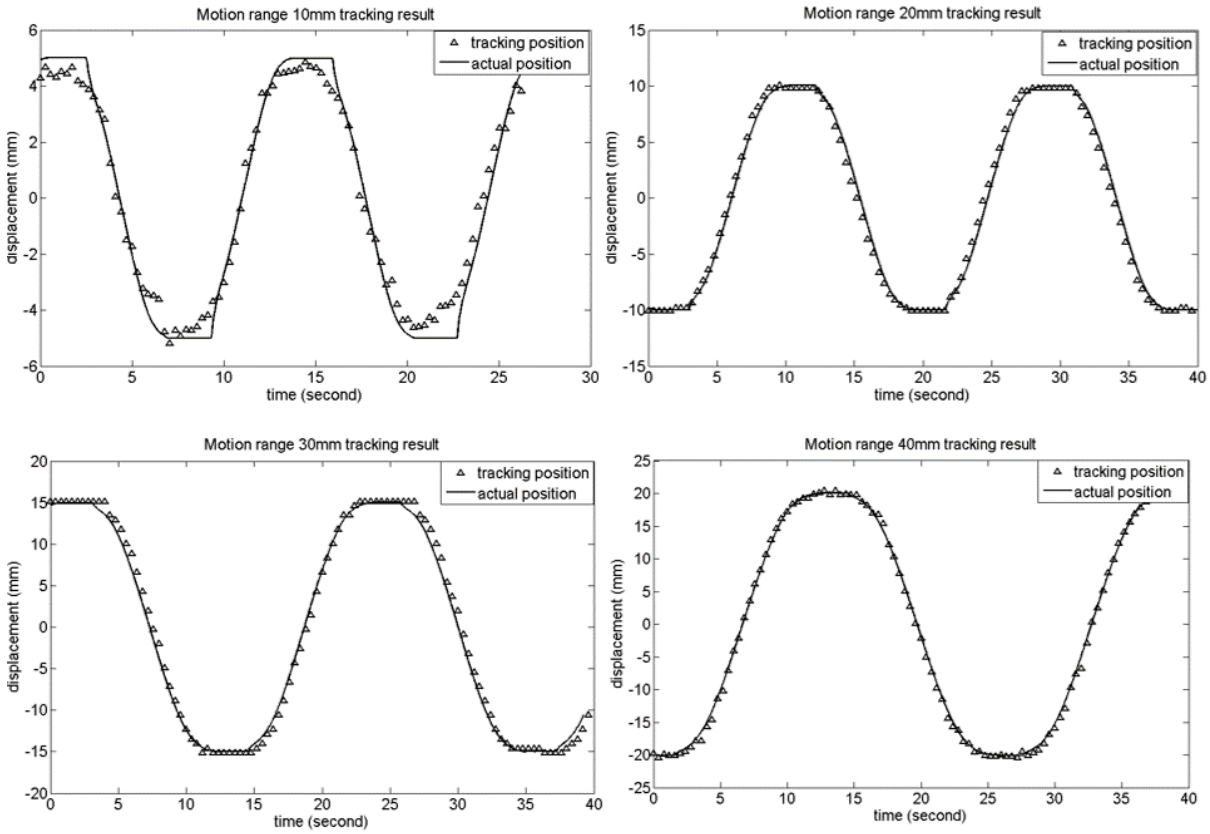

Figure 6.18 Comparison between the tracking result from the algorithm and the actual position (robot optical sensor monitoring record).

The tracking accuracy at each measured point is determined by comparing the calculated positions $\vec{r}_{tracking}$ with the theoretical positions $\vec{r}_{robot}$ provided by the robotic arm on a point-by-point basis as $\vec{\epsilon}_i = \vec{r}_{tracking_i} - \vec{r}_{robot_i}$ (Andrew et al., 2004).

Note that all the errors are positive from the equation of $|\vec{\epsilon}_i| = |\vec{r}_{tracking_i} - \vec{r}_{robot_i}|$. In this work, since the motion only happens in one direction *x*, the errors are calculated as $|\vec{\epsilon}_i| = |x_{tracking_i} - x_{robot_i}|$. The distance error distribution for tracking algorithm is plotted as a frequency histogram (Figure 6.19). The RMS is 0.66 mm (labelled B), and 95% of the distance errors are smaller than 0.87 mm (labelled C). Considering the resolution of MR EPI scan of about 1.7mm (FOV=22cm×22 cm, Frequency×Phase=128×128), the precision of this tracking algorithm is in the magnitude of sub-pixel (half pixel).

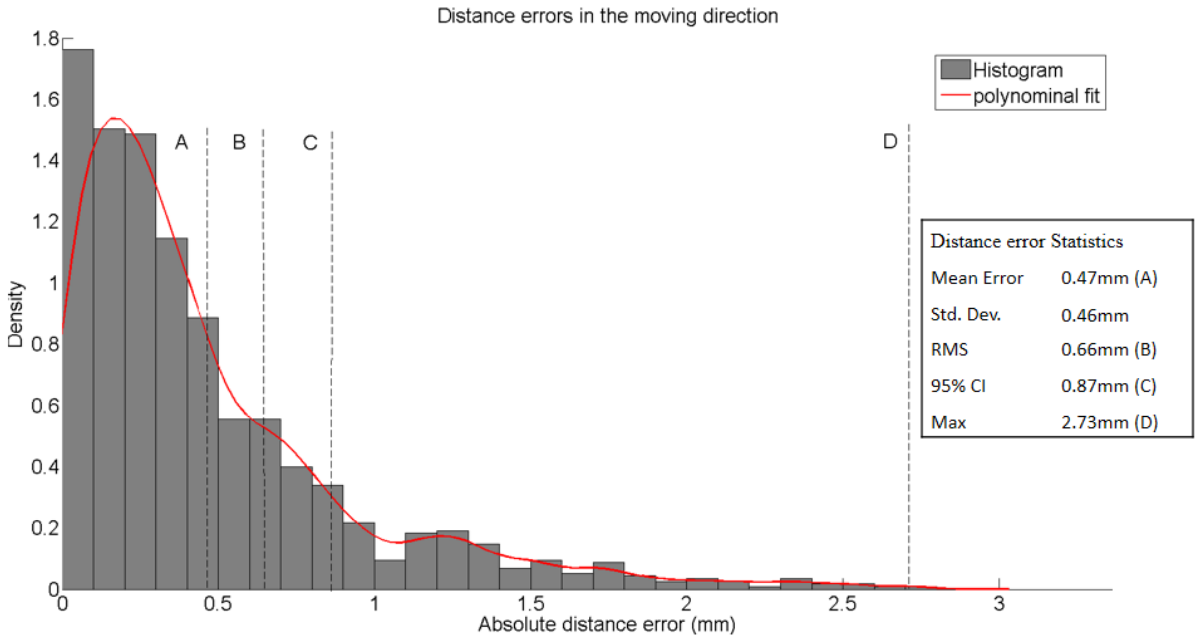

Figure 6.19 Summarize of all the distance errors along the axial direction in the MR coordinate system.

6.4.2 Motion synchronization experiment

The temperature rise was recorded via optical thermometer for all the sonication and cooling periods. The environmental temperature was normal temperature.

First of all, the reference temperature increase was obtained by sonicating a target area where was about 200 mm from the phased-array transducer, with an electrical power of 20W for 40 seconds. As shown in Figure 6.20, in the situation that the target was not

moving, the temperature increased fast at the first several seconds after HIFU beam was turned on, then increased slowly for a period. When the HIFU beam was turned off, the temperature dropped quickly to normal temperature. The maximum temperature was 52~58 ℃ in repetition test.

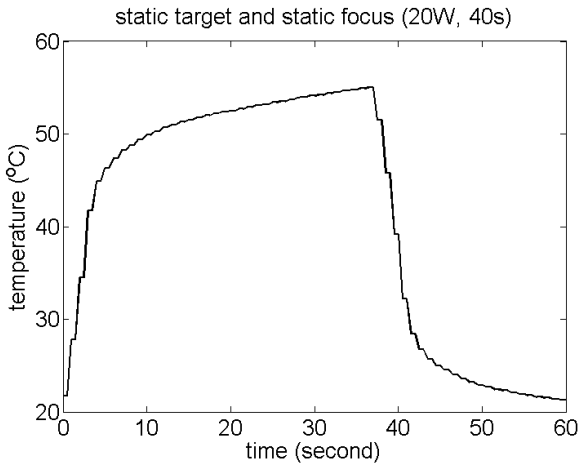

Figure 6.20 Temperature rise when the target and focus of ultrasound keep still，the target area was exposed to HIFU with electrical power of 20W for 40 seconds.

The temperature increases when the target was moving with a range of 10mm were shown

Figure 6.21a. The solid line represented when the HIFU tracking was turned on, that the HIFU beam was following the motion of the target area. With the electrical power of 20W for 40 seconds, the maximum temperature of the target areas achieved 51~59 ℃, which was not much different from the situation when the target was not moving. The dashed line represents when the tracking was turned off, which means, the target area kept moving, but the HIFU beam was not following it. The maximum temperature was 37.5~46.5 ℃, about 10 ℃ lower than when the HIFU tracking was on.

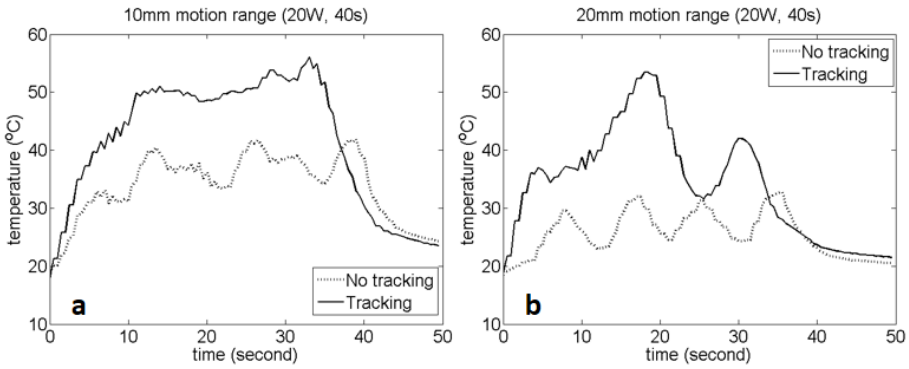

Figure 6.21 Temperature increase difference between situations when target was moving in the range of 10mm and 20mm. Solid line represents the HIFU tracking was turned on, dashed line represents the HIFU tracking was turned off.

Similar temperature difference was observed when the target was moving in the range of 20mm (Figure 6.21b). The temperature increased more when the HIFU tracking was turned on than when the HIFU tracking was turned off. The temperature increase difference was about 20℃. In the larger motion range situation, the temperature increased with greater fluctuation. However the maximum temperature was similar to the maximum temperature in the smaller motion range situation.

For the HIFU tracking (beam-steering) situations, the temperature was increasing with fluctuations. The fluctuation was similar to the situation when beam-steering was off. A reason for the fluctuation is that the beam-steering trajectory and the target area motion trajectory were not exactly overlapped (Figure 6.22). Since the robotic arm moved the target phantom along one axis, under this assumption, the ultrasound beam was moving along a linear pattern. However when the phantom moved, it is hard to avoid motion in other directions or deformation because the phantom is elastic rather than complete rigid. When the US focus shifted too much from the target area, the temperature would rise slowly or even drop down a bit. Only when they are close enough to each other, the temperature will increase rapidly.

The systematic error for the non-overlapping is coming from the coordinates measuring of the target in the MR images. Because the MR scan plane thickness was 5mm, the measuring precision could only achieve 2.5 mm in the direction perpendicular to the image plane.

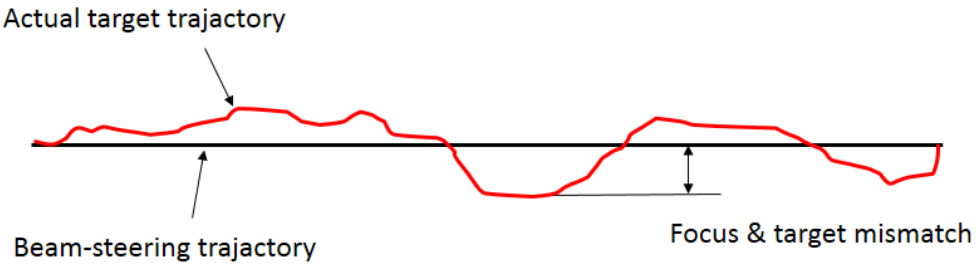

Figure 6.22 Mismatch between focus and target position. Black line is the US focus route, Red line represents actual target trajectory. When they are far from each other, the temperature would increase slowly or even drop. When they are close enough to each other, the temperature would increase rapidly.

There are also small fluctuations when the temperature was increasing. It was because that the beam-steering is not completely continuous, it was using a set of step-by-step local sonications to approximate the beam-steering (Figure 6.12). Because the shift of the focus from the target was smaller than the out-of-plane mismatching between the two trajectories, the temperature fluctuations were not obvious.

Below (Table 6-2) is a brief summary of all of the sonication results from this series of experiments. All the other situations were repeated for 3 times.

Table 6-2 Summary of ablation results

Type	Static	No tracking		Beam tracking	
Acoustic power (W)	20	20		20	
Duration (seconds)	40	40		40	
Motion range (mm)	0	10	20	10	20
Peak temperature (°C)	52~58	37.5~46.5	27.5~36.5	51~59	49.5~56.5
Repeated times	3	3	3	3	3

6.5 Summary and discussions

In this chapter, the issues of human liver motion tracking in MRgFUS are studied.

Firstly, the target position tracking algorithm was developed. According to volunteer scan results, the tissue mimicking structure was fabricated to simulate how a human liver appeared in the MR EPI scans. Based on the image properties, an MATLAB programme was developed to track the target movement in a plane. The performance of the tracking programme was tested via an experimental setup in which the motion was carefully controlled by a robotic arm. The off-line image processing results showed that the algorithm based on cross correlation of images could achieve a sub-millimetre tracking accuracy.

Secondly, a synchronization system between the target motion and beam-steering was setup. Based on this system, several key problems for motion tracking were studied, including how to realize beam-steering with a phased-array transducer, how to map target position in the MR frame to the focus position in the HIFU transducer frame, and how to use step-by-step local sonication to approximate continuous beam-steering. The system performance was tested with a series of sonications, in which temperature rises were compared between when the target was moving with and without beam-steering. A primary conclusion can be made that beam-steering could decrease the impact of target movement in focused ultrasound ablation.

To conclude, the two issues in MRgFUS for motion tracking, target tracking algorithm and HIFU beam-steering, are investigated separately in this thesis. The tracking algorithm is developed as an off-line processing programme. Moreover, the result of HIFU beam-steering is tested in a phantom with highly controlled motion.

The challenging but fascinating future work is to integrate the target motion tracking algorithm with the beam-steering system. With this achieved, the target position in the MR EPI scan results will be mapped to the focus position in real-time, then the phased-array transducer will steer the beam to focus at the desired target area accordingly.

Chapter 7 Conclusion and future work

The thesis concentrates on primary problems caused by liver motion in image guided FUS, including motion tracking and treatment assessment. These challenges were investigated in two main situations: USgFUS and MRgFUS. In each situation, programmes were developed to track the motion target in a stream of images based on different graphical image landmarks. Active focus of high intensity ultrasound beam could follow the motion target via a phased array HIFU transducer. Sonoelastography has proved to be useful to evaluate the FUS lesions in phantom and fresh animal tissues.

7.1 Conclusions

7.1.1 Motion tracking regarding to USgFUS

For USgFUS, this study focused on realizing real-time target motion tracking with B-mode sonography and assessment of FUS lesion formation via strain sonoelastography. However, some problems associated with these two issues were also analyzed and investigated. For example, to test the motion tracking algorithm, experimental setups were built which could produce a simulated motion to the human freely breathing pattern, as well as could produce a similar graphical view to tumours in human organs. Regarding strain sonoelastography on assessing FUS lesions, to create a precision criterion of elastography, a 3D volume construction method was developed to calculate the volume of lesions from 2D elastography scan.

Image processing method for motion target tracking

Based on general graphic view of tumours in human liver, an active snake contour tracking method was realized to segment the target in ultrasound B-mode image series. This method can cope with various target shapes. The tracking algorithms could process images with a frame rate higher than five frames per second. A two-layered tissue mimicking phantom produced a similar graphic view of tumours in human liver. With this phantom, it is possible to test the repeatability of the tracking algorithm.

Three experimental setups were built to test the tracking accuracy and computation robustness of the active snake contour tracking methods in 1D and 2D. The first two setups can move the target phantom in highly controlled modes. The first setup provides a 1D reciprocal movement and the second provides a 2D cycling movement. The third setup is a breath simulation device which mimics the motion pattern of human liver when the patient is in respiration. The motion range and speed in 2D were found to be comparable to the motion of human liver in SI and LR directions. The active snake tracking algorithms will then extract the coordinates of the target phantom. This tracking algorithm was proved to have an accuracy of higher than one millimetre in a motion range similar to human liver.

Assessment of lesion formation using ultrasound strain elastography

For ultrasound image guided FUS for motion tracking with the exception of moving target tracking algorithms, the lesions assessment is another issue to be considered.

Through comparisons of the elastograms between pre- and post-FUS around the focal zone both in PAA phantoms and fresh animal tissues, ultrasound strain elastography has been proven to be useful in assessing lesion regions during FUS sonication. Strain sonoelastography presents a potential tool for real-time ultrasound image guided FUS.

In this study, a method using strain ultrasound elastography was developed that can identify FUS-induced lesions in PAA egg-white phantom and ex vivo fresh sheep livers. Moreover, the method to differentiate FUS-induced lesions in different samples was characterized under different FUS doses, with different power and duration of FUS sonication under ultrasound strain elastography.

A bowl shaped HIFU transducer was used to generate lesions and strain sonoelastography was used to evaluate FUS lesions. The axis of the HIFU ultrasound transducer is kept within the ultrasound imaging plane in all tests so the transverse view of the lesion area will be observed in diagnostic ultrasound images.

The accuracy of the lesion detection via strain sonoelastography was tested, by comparing the volumes of pre-heated lesions with the volumes of 3D-reconstruction from 2D elastography scans. Results show that the precision image processing method was in an acceptable level. In this study, pre-compressive axial strain was chosen to be 10% after analysing the influence of different pre-compressive strains on the 3D reconstruction accuracy.

FUS-induced lesions and its characteristics with respect to ultrasound power and duration in egg-white PAA phantom. The threshold level of electrical power of focused ultrasound for the ultrasound strain elastography to detect was found to be around 80W. The findings in ex vivo fresh sheep liver regarding FUS-induced lesions draw to a conclusion that either higher ultrasound electrical power or longer ultrasound duration would result in larger and clearer lesions in ultrasound strain elastography.

Strain ultrasound elastography has been proven to be useful in assessing the protein-denatured regions of FUS sonication in egg-white PAA phantom and fresh sheep liver in this study. In both PAA phantoms and fresh sheep livers, the FUS lesions are more easily to visualize using strain sonoelastography than using B-mode ultrasound scan. In PAA egg-white phantoms, strain sonoelastographpy could visualize FUS lesions more easily than naked eyes.

To conclude, for USgFUS, the problem of target motion tracking in two dimensions was deeply studied. The method proposed in this thesis could track a motion target in breath pattern with a relatively fast speed. An attempt of using strain sonoelastography to assess FUS lesions was conducted. This process proved to be an applicable complementary approach to identify FUS lesion using B-mode ultrasound.

7.1.2 Motion tracking regarding to MRgFUS

In this thesis, the issues of MRgFUS in motion tracking include a new localization method for an MR compatible robotic arm and the synchronization of motion target and focus of ultrasound.

MR compatible robotic arm and its new localization method

A combination of a commercial MR compatible robotic arm, a bowl shaped fixed single focus FUS transducer and a customized active tracking device were combined for MRgFUS therapy.

The active tracking was implemented using a customized device with four micro-coils in a rectangular pattern. The centre of the four micro-coils was defined as the position of the robotic arm. This method was calibrated using a tissue mimicking agar phantom, which could provide reference points for the tracking characterization. Active tracking realized position tracking of a robotic arm with an acceptable accuracy at a sub-second update rate. A series of phantom ablation experiments were conducted, in which the robotic arm guided a HIFU transducer to sonicate on phantoms, and its location was monitored via active tracking. The localization accuracy and applicability for MRgFUS of this combined setup were evaluated. This system proved the feasibility of using a mechanical device to guide the FUS transducer to ablate targets in MRI scanner.

Besides that, the integration of fast localization and the MR robotic arm plays an important role in the following work. This robot could provide a reciprocal motion in the MRI scanner. In the meantime, the fast localization method could monitor this movement in real-time accurately. Therefor the robotic arm becomes the key setup for providing target motion, which mimics the liver motion caused by human breath.

Synchronization of motion target and focus of ultrasound

After that, the synchronization of a motion target and focus of ultrasound issue has been investigated.

The target position tracking algorithm was studied first. A tissue mimicking structure was fabricated to simulate how a human liver appeared in the MR EPI scans. In the MRI scans, the phantom structure produced similar graphical features to volunteers' livers. The phantom structure was guided to move reciprocally by the robotic arm, with a similar pattern to the respiratory motion of volunteers' livers. A programme based on landmarks segmentation and cross correlation was developed to track the target motion. Results showed that the tracking programme could achieve an accuracy of sub-

millimetre with a speed of 10 milliseconds per frame, which is precise and fast enough considering the pixel size (3 mm×3 mm) of standard MR scans.

The synchronization system between the target motion and beam-steering was set up. In this setup, the phantom structure was moved back and forth in a linear trajectory, and active focus of ultrasound was following this motion to guarantee enough FUS dose on the target area. The temperature rises within the target area was monitored via optical temperature measurement. From results, the primary conclusion could be drawn that beam-steering could decrease the impact of target movement in focused ultrasound ablation. Motion tracking in MRgFUS has the potential to be realized, which has the potential to be a complementary method to conventional solutions regarding respiratory motion problems. Several key problems for motion tracking were investigated and solved including how to realize beam-steering with a phased-array transducer, how to map target location in the MR frame to the focus position in the transducer frame, and how to use step-by-step local sonications to approximate continuous beam-steering.

For MRgFUS, this study mainly focused on target motion tracking and dynamic FUS sonication. Fast MRI EPI scan proved useful for motion tracking. Moreover, Beam-steering of FUS on target could complement problems caused by the motion effect.

7.2 Future work

7.2.1 Integration of target tracking and treatment monitoring in USgFUS

Although the motion target tracking problem and lesion formation assessment methods have been investigated in this thesis, a complete realization for ultrasound image guided focused ultrasound sonication has yet been achieved.

Applying the ultrasound strain elastography into the ultrasound image guided motion target tracking is challenging but fascinating. Since the ultrasound will be used both for target tracking and real-time lesion formation monitoring, the signal coupling issue between high power focused ultrasound from HIFU transducer and the ultrasound imaging probe has to be considered. As shown in Figure 7.1, the target area is hardly to be recognized in the diagnostic ultrasound image (1MH) when HIFU (550kHz, 5W) is

switched on. A probable solution for that is to apply pulsed high power focused ultrasound. The diagnostic ultrasound image acquisition and image processing for target tracking should be conducted only between the pulses of high power focused ultrasound.

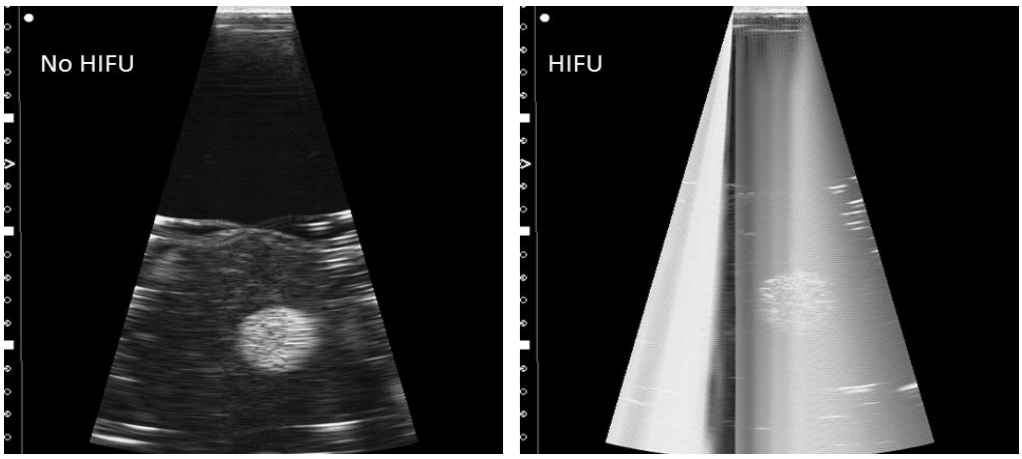

Figure 7.1 Diagnostic ultrasound image quality changes a lot with and without HIFU interference. The target area (round white area) cannot be recognized when HIFU is switched on.

Another restriction of USgFUS is that the diagnostic ultrasound image could only monitor target motion in two dimensions. This problem could be solved by careful treatment plan if the target stays in the same plane. However when it comes to motion situation, the target area is easily to move out of the image plane. Therefore, applying 3D diagnostic ultrasound is a potential solution for this problem.

Besides above, strain elastography still lack the technology to transform it into real-time imaging for clinical FUS guidance. They require controlled compression and demand a much shorter FUS duty cycle. Due to this limitation, the possibility of using shear wave elastography with similar approaches to assessing FUS-induced lesions could become a substitute.

7.2.2 Integration of MR thermometry into motion tracking for MRgFUS

The first challenge thing for MRgFUS for a motion target is the system complexity. The integration of real-time motion target tracking, the beam-steering, and treatment

monitoring need a cross-platform to manage. A promising tool is the RTHawk (0.9.28, HeartVista, Inc, Palo Alto, CA, USA), which can control the MR scanner and read image stream from it. Meanwhile, the image processing programme can be integrated into the RTHawk. Then the software could guide the phased-array HIFU transducer to steer the ultrasound beam to lock on to expected motion target.

Besides above, realizing MR thermometry is of more importance than using thermometer to monitor the temperature rise. Conventional MR thermometry was based on reference base-line processing. Because of the scanning speed restriction, it was susceptible to motion target. A proper thermometry method needs to be developed to sustain temperature monitoring when samples are moving. So the MR thermometry scan will interleave with fast MR EPI scan for motion tracking.

7.2.3 Applicability on *ex vivo* animal tissues, Thiel-emblamed cadaver and *in vivo*

Most of the samples used in this study are phantoms or ex vivo animal tissues. The performance of the methods for motion tracking in image guided focused ultrasound should also be tested on other materials. For example, the strain elastography assessment on FUS lesion formation could be considered to be used on Thiel-embalmed cadavers. The image guided FUS methods was to be tested on Thiel-embalmed cadavers if the cadaver could produce a respiratory motion using ventilation (Eisma et al., 2013). The target motion tracking algorithms was to be evaluated on more volunteer image scans.

References

"World Cancer Report". International Agency for Research on Cancer 2008.

AHMED, H. U., ZACHARAKIS, E., DUDDERIDGE, T., ARMITAGE, J. N., SCOTT, R., CALLEARY, J., ILLING, R., KIRKHAM, A., FREEMAN, A., OGDEN, C., ALLEN, C. & EMBERTON, M. 2009. High-intensity-focused ultrasound in the treatment of primary prostate cancer: the first UK series. *Br J Cancer,* 101**,** 19-26.

AL-BATAINEH, O., JENNE, J. & HUBER, P. 2012. Clinical and future applications of high intensity focused ultrasound in cancer. *Cancer Treat Rev,* 38**,** 346-53.

ALEXANDROV, A. V., MOLINA, C. A., GROTTA, J. C., GARAMI, Z., FORD, S. R., ALVAREZ-SABIN, J., MONTANER, J., SAQQUR, M., DEMCHUK, A. M., MOYÉ, L. A., HILL, M. D. & WOJNER, A. W. 2004a. Ultrasound-Enhanced Systemic Thrombolysis for Acute Ischemic Stroke. *New England Journal of Medicine,* 351**,** 2170-2178.

ALEXANDROV, A. V., WOJNER, A. W. & GROTTA, J. C. 2004b. CLOTBUST: design of a randomized trial of ultrasound-enhanced thrombolysis for acute ischemic stroke. *Journal of Neuroimaging,* 14**,** 108-12.

ANDREW, DAVID & DONALD. Year. Accuracy assessment and interpretation for optical tracking systems. *In:* L., R., ed. Medical Imaging 2004: Visualization, Image-Guided Procedures, and Display, 2004. 421-432.

ANDREW B. HOLBROOK, M. A. R., ANDREAS MELZER, KIM BUTTS PAUDY. Year. Interventional MRI from the Internet Browser. *In:* 9th Interventional MRI Symposium, 01/2012 Boston, MA.

ASTM, I. 2010. F2182-09: Standard Test Method for Measurement of Radio Frequency Induced Heating Near Passive Implants During Magnetic Resonance Imaging.

AUBOIROUX, V., DUMONT, E., PETRUSCA, L., VIALLON, M. & SALOMIR, R. 2011. An MR-compliant phased-array HIFU transducer with augmented steering range, dedicated to abdominal thermotherapy. *Physics in Medicine and Biology,* 56**,** 3563-82.

AUBOIROUX, V., PETRUSCA, L., VIALLON, M., GOGET, T., BECKER, C. D. & SALOMIR, R. 2012. Ultrasonography-based 2D motion-compensated HIFU sonication integrated with reference-free MR temperature monitoring: a feasibility study ex vivo. *Physics in Medicine and Biology,* 57**,** N159-71.

AZZOUZ, H. & DE LA ROSETTE, J. J. M. C. H. 2006. HIFU: Local Treatment of Prostate Cancer. *EAU-EBU Update Series,* 4**,** 62-70.

BEERLAGE, H. P., THÜROFF, S., DEBRUYNE, F. M. J., CHAUSSY, C. & DE LA ROSETTE, J. J. M. C. H. 1999. Transrectal high-intensity focused ultrasound using the Ablatherm device in the treatment of localized prostate carcinoma. *Urology,* 54**,** 273-277.

BERCOFF, J., TANTER, M. & FINK, M. 2004. Supersonic shear imaging: a new technique for soft tissue elasticity mapping. *IEEE Trans Ultrason Ferroelectr Freq Control,* 51**,** 396-409.

BLANA, A., ROGENHOFER, S., GANZER, R., LUNZ, J.-C., SCHOSTAK, M., WIELAND, W. F. & WALTER, B. 2008. Eight Years' Experience With High-Intensity Focused Ultrasonography for Treatment of Localized Prostate Cancer. *Urology,* 72**,** 1329-1333.

BLANA, A., WALTER, B., ROGENHOFER, S. & WIELAND, W. F. 2004. High-intensity focused ultrasound for the treatment of localized prostate cancer: 5-year experience. *Urology,* 63**,** 297-300.

BOTROS, Y. Y., VOLAKIS, J. L., VANBAREN, P. & EBBINI, E. S. 1997. A hybrid computational model for ultrasound phased-array heating in presence of strongly scattering obstacles. *IEEE Trans Biomed Eng,* 44**,** 1039-50.

BRYAN, P. J., CUSTAR, S., HAAGA, J. R. & BALSARA, V. 1984. Respiratory movement of the pancreas: an ultrasonic study. *J Ultrasound Med,* 3**,** 317-20.

CHMARRA, M. K., HANSEN, R., MARVIK, R. & LANGO, T. 2013. Multimodal phantom of liver tissue. *Plos One,* 8**,** e64180.

CHOI, J. J., PERNOT, M., SMALL, S. A. & KONOFAGOU, E. E. 2007. Noninvasive, transcranial and localized opening of the blood-brain barrier using focused ultrasound in mice. *Ultrasound in Medicine and Biology,* 33**,** 95-104.

CHUANG, B., MYRONENKO, A., ENGLISH, R. & NOBLE, A. Year. Interpreting ultrasound elastography: Image registration of breast cancer ultrasound elastography to histopathology images. *In:* Biomedical Imaging: From Nano to Macro, 2010 IEEE International Symposium on, 14-17 April 2010 2010. 181-184.

CIVALE, J., CLARKE, R., RIVENS, I. & TER HAAR, G. 2006. The use of a segmented transducer for rib sparing in HIFU treatments. *Ultrasound in Medicine and Biology,* 32**,** 1753-61.

CLEARY, K., MELZER, A., WATSON, V., KRONREIF, G. & STOIANOVICI, D. 2006. Interventional robotic systems: applications and technology state-of-the-art. *Minim Invasive Ther Allied Technol,* 15**,** 101-13.

CLINE, H. E., SCHENCK, J. F., HYNYNEN, K., WATKINS, R. D., SOUZA, S. P. & JOLESZ, F. A. 1992. MR-guided focused ultrasound surgery. *J Comput Assist Tomogr,* 16**,** 956-65.

CLINE, H. E., SCHENCK, J. F., WATKINS, R. D., HYNYNEN, K. & JOLESZ, F. A. 1993. Magnetic resonance-guided thermal surgery. *Magn Reson Med,* 30**,** 98-106.

COCHARD, E., PRADA, C., AUBRY, J. F. & FINK, M. 2009. Ultrasonic focusing through the ribs using the DORT method. *Med Phys,* 36**,** 3495-503.

COLEMAN, R. E. 2006. Clinical Features of Metastatic Bone Disease and Risk of Skeletal Morbidity. *Clinical Cancer Research,* 12**,** 6243s-6249s.

COOK, J. R., BOUCHARD, R. R. & EMELIANOV, S. Y. 2011. Tissue-mimicking phantoms for photoacoustic and ultrasonic imaging. *Biomed Opt Express,* 2**,** 3193-206.

CURIEL, L. & HYNYNEN, K. 2011. Localized Harmonic Motion Imaging for Focused Ultrasound Surgery Targeting. *Ultrasound in Medicine & Biology,* 37**,** 1230-1239.

CURIEL, L., SOUCHON, R., ROUVIÈRE, O., GELET, A. & CHAPELON, J. Y. 2005. Elastography for the follow-up of high-intensity focused ultrasound prostate cancer treatment: Initial comparison with MRI. *Ultrasound in Medicine & Biology,* 31**,** 1461-1468.

CURRIE J, C. P. 1880. Contractions et dilatations produites par des tensions dans les cristaux hémièdres à faces inclinées. *Comptes Rendus Hebdomadaires Des Seances De L Academie Des Sciences Serie B,* 90**,** 1506-1510.

DAFFERTSHOFER, M. & HENNERICI, M. 2003. Ultrasound in the treatment of ischaemic stroke. *The Lancet Neurology,* 2**,** 283-290.

DAMADIAN, R., GOLDSMITH, M. & MINKOFF, L. 1977. NMR in cancer: XVI. FONAR image of the live human body. *Physiol Chem Phys,* 9**,** 97-100, 108.

DAMIANOU, C. & HYNYNEN, K. 1994. The effect of various physical parameters on the size and shape of necrosed tissue volume during ultrasound surgery. *Journal of the Acoustical Society of America,* 95**,** 1641-9.

DAVIES, S. C., HILL, A. L., HOLMES, R. B., HALLIWELL, M. & JACKSON, P. C. 1994. Ultrasound quantitation of respiratory organ motion in the upper abdomen. *Br J Radiol,* 67**,** 1096-102.

DE OLIVEIRA, A., RAUSCHENBERG, J., BEYERSDORFF, D., SEMMLER, W. & BOCK, M. 2008. Automatic passive tracking of an endorectal prostate biopsy device using phase-only cross-correlation. *Magn Reson Med,* 59**,** 1043-50.

DE OLIVEIRA, P. L., DE SENNEVILLE, B. D., DRAGONU, I. & MOONEN, C. T. W. 2010. Rapid motion correction in MR-guided high-intensity focused ultrasound heating using real-time ultrasound echo information. *Nmr in Biomedicine,* 23**,** 1103-1108.

DE SENNEVILLE, B. D., MOUGENOT, C. & MOONEN, C. T. W. 2007. Real-time adaptive methods for treatment of mobile organs by MRI-controlled high-intensity focused ultrasound. *Magnetic Resonance in Medicine,* 57**,** 319-330.

DELAPAZ, R. L. 1994. Echo-planar imaging. *Radiographics,* 14**,** 1045-58.

DUMOULIN, C. L., MALLOZZI, R. P., DARROW, R. D. & SCHMIDT, E. J. 2010. Phase-field dithering for active catheter tracking. *Magn Reson Med,* 63**,** 1398-403.

DUMOULIN, C. L., SOUZA, S. P. & DARROW, R. D. 1993. Real-time position monitoring of invasive devices using magnetic resonance. *Magnetic Resonance in Medicine,* 29**,** 411-415.

FAHEY, B. J., NIGHTINGALE, K. R., MCALEAVEY, S. A., PALMERI, M. L., WOLF, P. D. & TRAHEY, G. E. 2005. Acoustic radiation force impulse imaging of myocardial radiofrequency ablation: initial in vivo results. *IEEE Trans Ultrason Ferroelectr Freq Control,* 52**,** 631-41.

FAHEY, B. J., NIGHTINGALE, K. R., STUTZ, D. L. & TRAHEY, G. E. 2004. Acoustic radiation force impulse imaging of thermally- and chemically-induced lesions in soft tissues: preliminary ex vivo results. *Ultrasound in Medicine & Biology,* 30**,** 321-328.

FEINBERG, D. A., GIESE, D., BONGERS, D. A., RAMANNA, S., ZAITSEV, M., MARKL, M. & GUNTHER, M. 2010. Hybrid ultrasound MRI for improved cardiac imaging and real-time respiration control. *Magn Reson Med,* 63**,** 290-6.

FLASK, C., ELGORT, D., WONG, E., SHANKARANARAYANAN, A., LEWIN, J., WENDT, M. & DUERK, J. L. 2001. A method for fast 3D tracking using tuned fiducial markers and a limited projection reconstruction FISP (LPR-FISP) sequence. *J Magn Reson Imaging,* 14**,** 617-27.

GAO, J. 2012. *Transcostal Focused Ultrasound Surgery: Treatment through the Ribcage.* PhD, University of Dundee.

GAO, J., YOU, J., HUANG, Z., COCHRAN, S. & CORNER, G. 2012. Simultaneous Measurement of Thermophysical Properties of Tissue-Mimicking Phantoms for High Intensity Focused Ultrasound (HIFU) Exposures. *International Journal of Thermophysics,* 33**,** 495-504.

GELAT, P., TER HAAR, G. & SAFFARI, N. 2011. Modelling of the acoustic field of a multi-element HIFU array scattered by human ribs. *Physics in Medicine and Biology,* 56**,** 5553-81.

GELET, A., CHAPELON, J. Y., BOUVIER, R., PANGAUD, C. & LASNE, Y. 1999. LOCAL CONTROL OF PROSTATE CANCER BY TRANSRECTAL HIGH INTENSITY FOCUSED ULTRASOUND THERAPY: PRELIMINARY RESULTS. *The Journal of Urology,* 161**,** 156-162.

GOLDBERG, S. N., GRASSI, C. J., CARDELLA, J. F., CHARBONEAU, J. W., DODD, G. D., 3RD, DUPUY, D. E., GERVAIS, D., GILLAMS, A. R., KANE, R. A., LEE, F. T., JR., LIVRAGHI, T., MCGAHAN, J., PHILLIPS, D. A., RHIM, H. & SILVERMAN, S. G. 2005. Image-guided tumor ablation: standardization of terminology and reporting criteria. *Radiology,* 235**,** 728-39.

GUISE, T. 2010. Examining the Metastatic Niche: Targeting the Microenvironment. *Seminars in Oncology,* 37, Supplement 2**,** S2-S14.

HAAR, G. T. & COUSSIOS, C. 2007. High intensity focused ultrasound: physical principles and devices. *Int J Hyperthermia,* 23**,** 89-104.

HAN, X., XU, C. & PRINCE, J. L. 2007. Fast numerical scheme for gradient vector flow computation using a multigrid method. *Image Processing, IET,* 1**,** 48-55.

HIRANO, Y., ODA, M., TSUNEZUKA, Y., ISHIKAWA, N. & WATANABE, G. 2005. Long-term survival cases of lung cancer presented as solitary bone metastasis. *Ann Thorac Cardiovasc Surg,* 11**,** 401-4.

HYNYNEN, K., MCDANNOLD, N., CLEMENT, G., JOLESZ, F. A., ZADICARIO, E., KILLIANY, R., MOORE, T. & ROSEN, D. 2006. Pre-clinical testing of a phased array ultrasound system for MRI-guided noninvasive surgery of the brain--a primate study. *European Journal of Radiology,* 59**,** 149-56.

HYNYNEN, K. H. 2007. *Fundamental Principles of Therapeutic Ultrasound,* New York, NY:Informa HealthCare USA.

ILLING, R. O., KENNEDY, J. E., WU, F., TER HAAR, G. R., PROTHEROE, A. S., FRIEND, P. J., GLEESON, F. V., CRANSTON, D. W., PHILLIPS, R. R. & MIDDLETON, M. R. 2005. The safety and feasibility of extracorporeal high-intensity focused ultrasound (HIFU) for the treatment of liver and kidney tumours in a Western population. *Br J Cancer,* 93**,** 890-5.

ISO 2007. Plastics. *Determination of thermal conductivity and thermal diffusivity*.

JENNE, J. W., PREUSSER, T. & GÜNTHER, M. 2012. High-intensity focused ultrasound: Principles, therapy guidance, simulations and applications. *Zeitschrift Fur Medizinische Physik,* 22**,** 311-322.

JIN, C., ZHU, H., WANG, Z., WU, F., CHEN, W., LI, K., SU, H., ZHOU, K. & GONG, W. 2011. High-intensity focused ultrasound combined with transarterial chemoembolization for unresectable hepatocellular carcinoma: long-term follow-up and clinical analysis. *European Journal of Radiology,* 80**,** 662-9.

JUNG, S. E., CHO, S. H., JANG, J. H. & HAN, J. Y. 2011. High-intensity focused ultrasound ablation in hepatic and pancreatic cancer: complications. *Abdominal Imaging,* 36**,** 185-95.

KALLEL, F., STAFFORD, R. J., PRICE, R. E., RIGHETTI, R., OPHIR, J. & HAZLE, J. D. 1999. The feasibility of elastographic visualization of HIFU-induced thermal lesions in soft tissues. *Ultrasound in Medicine & Biology,* 25**,** 641-647.

KARAKITSIOS, I., BOBEICA, M., SALIEV, T., RUBE, M. & MELZER, A. 2014. Thermometry during MR-guided focused ultrasound in a preclinical model based on Thiel embalmed tissue. *Minim Invasive Ther Allied Technol,* 23**,** 120-6.

KASS, M., WITKIN, A. & TERZOPOULOS, D. 1988. Snakes: Active contour models. *International Journal of Computer Vision,* 1**,** 321-331.

KENNEDY, J. E., TER HAAR, G. R. & CRANSTON, D. 2003. High intensity focused ultrasound: surgery of the future? *Br J Radiol,* 76**,** 590-9.

KHOKHLOVA, T. D., CANNEY, M. S., LEE, D., MARRO, K. I., CRUM, L. A., KHOKHLOVA, V. A. & BAILEY, M. R. 2009. Magnetic resonance imaging of boiling induced by high intensity focused ultrasound. *The Journal of the Acoustical Society of America,* 125**,** 2420-2431.

KLINGLER, H. C., SUSANI, M., SEIP, R., MAUERMANN, J., SANGHVI, N. & MARBERGER, M. J. 2008. A novel approach to energy ablative therapy of small renal tumours: laparoscopic high-intensity focused ultrasound. *European Urology,* 53**,** 810-6; discussion 817-8.

KOHRMANN, K. U., MICHEL, M. S., GAA, J., MARLINGHAUS, E. & ALKEN, P. 2002. High intensity focused ultrasound as noninvasive therapy for multilocal renal cell carcinoma: case study and review of the literature. *J Urol,* 167**,** 2397-403.

KONINGS, M. K., BARTELS, L. W., SMITS, H. F. & BAKKER, C. J. 2000. Heating around intravascular guidewires by resonating RF waves. *J Magn Reson Imaging,* 12**,** 79-85.

KOPELMAN, D., INBAR, Y., HANANNEL, A., FREUNDLICH, D., CASTEL, D., PEREL, A., GREENFELD, A., SALAMON, T., SARELI, M., VALEANU, A. & PAPA, M. 2006a. Magnetic resonance-guided focused ultrasound surgery (MRgFUS): ablation of liver tissue in a porcine model. *European Journal of Radiology,* 59**,** 157-62.

KOPELMAN, D., INBAR, Y., HANANNEL, A., FREUNDLICH, D., VITEK, S., SCHMIDT, R., SOKOLOV, A., HATOUM, O. A. & RABINOVICI, J. 2006b. Magnetic resonance-guided focused ultrasound surgery using an enhanced sonication technique in a pig muscle model. *European Journal of Radiology,* 59**,** 190-7.

KRAFFT, A. J., JENNE, J. W., MAIER, F., STAFFORD, R. J., HUBER, P. E., SEMMLER, W. & BOCK, M. 2010. A long arm for ultrasound: A combined robotic focused ultrasound setup for magnetic resonance-guided focused ultrasound surgery. *Medical Physics,* 37**,** 2380-2393.

KUHL, C. K., KOOIJMAN, H., GIESEKE, J. & SCHILD, H. H. 2007. Effect of B1 inhomogeneity on breast MR imaging at 3.0 T. *Radiology,* 244**,** 929-30.

LACROIX, M. 2006. Significance, detection and markers of disseminated breast cancer cells. *Endocr Relat Cancer,* 13**,** 1033-67.

LEPETIT, J. & CULIOLI, J. 1994. Mechanical properties of meat. *Meat Science,* 36**,** 203-237.

LESLIE, T. A., KENNEDY, J. E., ILLING, R. O., TER HAAR, G. R., WU, F., PHILLIPS, R. R., FRIEND, P. J., ROBERTS, I. S., CRANSTON, D. W. & MIDDLETON, M. R. 2008. High-intensity focused ultrasound ablation of liver tumours: can radiological assessment predict the histological response? *Br J Radiol,* 81**,** 564-71.

LI, J. J., GU, M. F., LUO, G. Y., LIU, L. Z., ZHANG, R. & XU, G. L. 2009. Complications of high intensity focused ultrasound for patients with hepatocellular carcinoma. *Technol Cancer Res Treat,* 8**,** 217-24.

LIBERMAN, B., GIANFELICE, D., INBAR, Y., BECK, A., RABIN, T., SHABSHIN, N., CHANDER, G., HENGST, S., PFEFFER, R., CHECHICK, A., HANANNEL, A., DOGADKIN, O. & CATANE, R. 2009. Pain palliation in patients with bone metastases using MR-guided focused ultrasound surgery: a multicenter study. *Annals of Surgical Oncology,* 16**,** 140-6.

LIU, W., ZAGZEBSKI, J. A., VARGHESE, T., DYER, C. R., TECHAVIPOO, U. & HALL, T. J. 2006. Segmentation of elastographic images using a coarse-to-fine active contour model. *Ultrasound in Medicine and Biology,* 32**,** 397-408.

M., D. C. E. 2006. *Design of ultrasound transducer arrays for medical imaging* PhD PhD thesis.

MANSFIELD, P., PYKETT, I. L. & MORRIS, P. G. 1978. Human whole body line-scan imaging by NMR. *Br J Radiol,* 51**,** 921-2.

MARKISZ, J. A. 2002. Medical imaging physics (fourth edition): William R. Hendee and E. Russell Ritenour. New York, NY, Wiley-Liss, 2002, 312 pages, 340 illustrations. *Clinical Imaging,* 26**,** 426.

MARTIN, E., JEANMONOD, D., MOREL, A., ZADICARIO, E. & WERNER, B. 2009. High-intensity focused ultrasound for noninvasive functional neurosurgery. *Annals of Neurology,* 66**,** 858-61.

MCDANNOLD, N., CLEMENT, G. T., BLACK, P., JOLESZ, F. & HYNYNEN, K. 2010. Transcranial magnetic resonance imaging- guided focused ultrasound surgery of brain tumors: initial findings in 3 patients. *Neurosurgery,* 66**,** 323-32; discussion 332.

MCDANNOLD, N., VYKHODTSEVA, N., RAYMOND, S., JOLESZ, F. A. & HYNYNEN, K. 2005. MRI-guided targeted blood-brain barrier disruption with focused ultrasound: histological findings in rabbits. *Ultrasound in Medicine and Biology,* 31**,** 1527-37.

MEDEL, R., MONTEITH, S. J., ELIAS, W. J., EAMES, M., SNELL, J., SHEEHAN, J. P., WINTERMARK, M., JOLESZ, F. A. & KASSELL, N. F. 2012. Magnetic resonance-guided focused ultrasound surgery: Part 2: A review of current and future applications. *Neurosurgery,* 71**,** 755-63.

MEERAN NAJI, M., MRCS, FRCR, RICHARD D. WHITE, MD 2013. Incidental finding of a hepatic angiomyolipoma. *Radiology Case Reports,* 8.

MEIJERING, B. D., JUFFERMANS, L. J., VAN WAMEL, A., HENNING, R. H., ZUHORN, I. S., EMMER, M., VERSTEILEN, A. M., PAULUS, W. J., VAN GILST, W. H., KOOIMAN, K., DE JONG, N., MUSTERS, R. J., DEELMAN, L. E. & KAMP, O. 2009. Ultrasound and microbubble-targeted delivery of macromolecules is regulated by induction of endocytosis and pore formation. *Circulation Research,* 104**,** 679-87.

MELZER, A., GUTMANN, B., REMMELE, T., WOLF, R., LUKOSCHECK, A., BOCK, M., BARDENHEUER, H. & FISCHER, H. 2008. INNOMOTION for Percutaneous Image-Guided Interventions. *Ieee Engineering in Medicine and Biology Magazine,* 27**,** 66-73.

MENG, X., HE, G., ZHANG, J., HAN, Z., YU, M., ZHANG, M., TANG, Y., FANG, L. & ZHOU, X. 2010. A comparative study of fibroid ablation rates using radio frequency or high-intensity focused ultrasound. *Cardiovasc Intervent Radiol,* 33**,** 794-9.

MESIWALA, A. H., FARRELL, L., WENZEL, H. J., SILBERGELD, D. L., CRUM, L. A., WINN, H. R. & MOURAD, P. D. 2002. High-intensity focused ultrasound selectively disrupts the blood-brain barrier in vivo. *Ultrasound in Medicine and Biology,* 28**,** 389-400.

O'SULLIVAN, A. K., THOMPSON, D., CHU, P., LEE, D. W., STEWART, E. A. & WEINSTEIN, M. C. 2009. Cost-effectiveness of magnetic resonance guided focused ultrasound for the treatment of uterine fibroids. *International Journal of Technology Assessment in Health Care,* 25**,** 14-25.

OKADA, A., MURAKAMI, T., MIKAMI, K., ONISHI, H., TANIGAWA, N., MARUKAWA, T. & NAKAMURA, H. 2006. A case of hepatocellular carcinoma treated by MR-guided focused ultrasound ablation with respiratory gating. *Magnetic Resonance in Medical Sciences,* 5**,** 167-71.

OPHIR, J., CESPEDES, I., PONNEKANTI, H., YAZDI, Y. & LI, X. 1991. Elastography: a quantitative method for imaging the elasticity of biological tissues. *Ultrason Imaging,* 13**,** 111-34.

ORDIDGE, R. J., COXON, R., HOWSEMAN, A., CHAPMAN, B., TURNER, R., STEHLING, M. & MANSFIELD, P. 1988. Snapshot head imaging at 0.5 T using the echo planar technique. *Magnetic Resonance in Medicine,* 8**,** 110-115.

ORDIDGE, R. J., HOWSEMAN, A., COXON, R., TURNER, R., CHAPMAN, B., GLOVER, P., STEHLING, M. & MANSFIELD, P. 1989. Snapshot imaging at 0.5 t using echo-planar techniques. *Magnetic Resonance in Medicine,* 10**,** 227-240.

PARK, J. C., PARK, S. H., KIM, J. H., YOON, S. M., SONG, S. Y., LIU, Z., SONG, B., KAUWELOA, K., WEBSTER, M. J., SANDHU, A., MELL, L. K., JIANG, S. B., MUNDT, A. J. & SONG, W. Y. 2012. Liver motion during cone beam computed tomography guided stereotactic body radiation therapy. *Med Phys,* 39**,** 6431-42.

PATIL, S., BIERI, O., JHOOTI, P. & SCHEFFLER, K. 2009. Automatic slice positioning (ASP) for passive real-time tracking of interventional devices using projection-reconstruction imaging with echo-dephasing (PRIDE). *Magn Reson Med,* 62**,** 935-42.

POISSONNIER, L., CHAPELON, J.-Y., ROUVIÈRE, O., CURIEL, L., BOUVIER, R., MARTIN, X., DUBERNARD, J. M. & GELET, A. 2007. Control of Prostate Cancer by Transrectal HIFU in 227 Patients. *European Urology,* 51**,** 381-387.

PYKETT, I. L. & MANSFIELD, P. 1978. A line scan image study of a tumorous rat leg by NMR. *Physics in Medicine and Biology,* 23**,** 961.

RAPOPORT, N., GAO, Z. & KENNEDY, A. 2007. Multifunctional nanoparticles for combining ultrasonic tumor imaging and targeted chemotherapy. *J Natl Cancer Inst,* 99**,** 1095-106.

REA, M., MCROBBIE, D., ELHAWARY, H., TSE, Z. T., LAMPERTH, M. & YOUNG, I. 2009. Sub-pixel localisation of passive micro-coil fiducial markers in interventional MRI. *MAGMA,* 22**,** 71-6.

RIEKE, V. & BUTTS PAULY, K. 2008. MR thermometry. *Journal of Magnetic Resonance Imaging,* 27**,** 376-390.

RIES, M., DE SENNEVILLE, B. D., ROUJOL, S., BERBER, Y., QUESSON, B. & MOONEN, C. 2010. Real-time 3D target tracking in MRI guided focused ultrasound ablations in moving tissues. *Magnetic Resonance in Medicine,* 64**,** 1704-1712.

RIGHETTI, R., KALLEL, F., STAFFORD, R. J., PRICE, R. E., KROUSKOP, T. A., HAZLE, J. D. & OPHIR, J. 1999. Elastographic characterization of HIFU-induced lesions in canine livers. *Ultrasound in Medicine & Biology,* 25**,** 1099-1113.

ROSS, C. S., HUSSEY, D. H., PENNINGTON, E. C., STANFORD, W. & FRED DOORNBOS, J. 1990. Analysis of movement of intrathoracic neoplasms using ultrafast computerized tomography. *International Journal of Radiation Oncology*Biology*Physics,* 18**,** 671-677.

SAPARETO, S. A. & DEWEY, W. C. 1984. Thermal dose determination in cancer therapy. *Int J Radiat Oncol Biol Phys,* 10**,** 787-800.

SCHROEDER, A., KOST, J. & BARENHOLZ, Y. 2009. Ultrasound, liposomes, and drug delivery: principles for using ultrasound to control the release of drugs from liposomes. *Chemistry and Physics of Lipids,* 162**,** 1-16.

SHEIKOV, N., MCDANNOLD, N., VYKHODTSEVA, N., JOLESZ, F. & HYNYNEN, K. 2004. Cellular mechanisms of the blood-brain barrier opening induced by ultrasound in presence of microbubbles. *Ultrasound in Medicine and Biology,* 30**,** 979-89.

SHIH, T. C., KOU, H. S., LIAUH, C. T. & LIN, W. L. 2005. The impact of thermal wave characteristics on thermal dose distribution during thermal therapy: a numerical study. *Med Phys,* 32**,** 3029-36.

SOUCHON, R., ROUVIÈRE, O., GELET, A., DETTI, V., SRINIVASAN, S., OPHIR, J. & CHAPELON, J.-Y. 2003. Visualisation of HIFU lesions using elastography of the human prostate in vivo: preliminary results. *Ultrasound in Medicine & Biology,* 29**,** 1007-1015.

SUN, J., ZHANG, A. & XU, L. X. 2008. Evaluation of alternate cooling and heating for tumor treatment. *International Journal of Heat and Mass Transfer,* 51**,** 5478-5485.

TAKEGAMI, K., KANEKO, Y., WATANABE, T., MARUYAMA, T., MATSUMOTO, Y. & NAGAWA, H. 2004. Polyacrylamide gel containing egg white as new model for irradiation experiments using focused ultrasound. *Ultrasound in Medicine and Biology,* 30**,** 1419-22.

TANG, A. M., KACHER, D. F., LAM, E. Y., WONG, K. K., JOLESZ, F. A. & YANG, E. S. 2008. Simultaneous ultrasound and MRI system for breast biopsy: compatibility assessment and demonstration in a dual modality phantom. *IEEE Trans Med Imaging,* 27**,** 247-54.

TER HAAR, G., SHAW, A., PYE, S., WARD, B., BOTTOMLEY, F., NOLAN, R. & COADY, A. M. 2011. Guidance on reporting ultrasound exposure conditions for bio-effects studies. *Ultrasound in Medicine and Biology,* 37**,** 177-83.

THIEL, W. 1992. [The preservation of the whole corpse with natural color]. *Annals of Anatomy-Anatomischer Anzeiger,* 174**,** 185-95.

THORMER, G., GARNOV, N., MOCHE, M., HAASE, J., KAHN, T. & BUSSE, H. 2012. Simultaneous 3D localization of multiple MR-visible markers in fully reconstructed MR images: proof-of-concept for subsecond position tracking. *Magnetic Resonance Imaging,* 30**,** 371-81.

UCHIDA, T., SANGHVI, N. T., GARDNER, T. A., KOCH, M. O., ISHII, D., MINEI, S., SATOH, T., HYODO, T., IRIE, A. & BABA, S. 2002. Transrectal high-intensity focused ultrasound for treatment of patients with stage T1b-2n0m0 localized prostate cancer: a preliminary report. *Urology,* 59**,** 394-398.

VIALLON, M., TERRAZ, S., ROLAND, J., DUMONT, E., BECKER, C. D. & SALOMIR, R. 2010. Observation and correction of transient cavitation-induced PRFS thermometry artifacts during radiofrequency ablation, using simultaneous ultrasound/MR imaging. *Med Phys,* 37**,** 1491-506.

VON SIEBENTHAL, M., SZEKELY, G., GAMPER, U., BOESIGER, P., LOMAX, A. & CATTIN, P. 2007. 4D MR imaging of respiratory organ motion and its variability. *Physics in Medicine and Biology,* 52**,** 1547-64.

WISE, L. A., PALMER, J. R., STEWART, E. A. & ROSENBERG, L. 2005. Age-specific incidence rates for self-reported uterine leiomyomata in the Black Women's Health Study. *Obstetrics and Gynecology,* 105**,** 563-8.

WU, F. 2006. Extracorporeal high intensity focused ultrasound in the treatment of patients with solid malignancy. *Minim Invasive Ther Allied Technol,* 15**,** 26-35.

WU, F., WANG, Z.-B., CHEN, W.-Z., ZOU, J.-Z., BAI, J., ZHU, H., LI, K.-Q., JIN, C.-B., XIE, F.-L. & SU, H.-B. 2005a. Advanced Hepatocellular Carcinoma: Treatment with High-Intensity Focused Ultrasound Ablation Combined with Transcatheter Arterial Embolization1. *Radiology,* 235**,** 659-667.

WU, F., WANG, Z.-B., ZHU, H., CHEN, W.-Z., ZOU, J.-Z., BAI, J., LI, K.-Q., JIN, C.-B., XIE, F.-L. & SU, H.-B. 2005b. Feasibility of US-guided High-Intensity Focused Ultrasound Treatment in Patients with Advanced Pancreatic Cancer: Initial Experience1. *Radiology,* 236**,** 1034-1040.

WU, F., WANG, Z. B., CAO, Y. D., CHEN, W. Z., BAI, J., ZOU, J. Z. & ZHU, H. 2003a. A randomised clinical trial of high-intensity focused ultrasound ablation for the treatment of patients with localised breast cancer. *Br J Cancer,* 89**,** 2227-33.

WU, F., WANG, Z. B., CAO, Y. D., ZHU, X. Q., ZHU, H., CHEN, W. Z. & ZOU, J. Z. 2007. "Wide local ablation" of localized breast cancer using high intensity focused ultrasound. *Journal of Surgical Oncology,* 96**,** 130-6.

WU, F., WANG, Z. B., CHEN, W. Z., BAI, J., ZHU, H. & QIAO, T. Y. 2003b. Preliminary experience using high intensity focused ultrasound for the treatment of patients with advanced stage renal malignancy. *J Urol,* 170**,** 2237-40.

WU, F., WANG, Z. B., CHEN, W. Z., ZHU, H., BAI, J., ZOU, J. Z., LI, K. Q., JIN, C. B., XIE, F. L. & SU, H. B. 2004a. Extracorporeal high intensity focused ultrasound ablation in the treatment of patients with large hepatocellular carcinoma. *Annals of Surgical Oncology,* 11**,** 1061-9.

WU, F., WANG, Z. B., CHEN, W. Z., ZOU, J. Z., BAI, J., ZHU, H., LI, K. Q., XIE, F. L., JIN, C. B., SU, H. B. & GAO, G. W. 2004b. Extracorporeal focused ultrasound surgery for treatment of human solid carcinomas: early Chinese clinical experience. *Ultrasound in Medicine and Biology,* 30**,** 245-60.

XIONG, L. L., HWANG, J. H., HUANG, X. B., YAO, S. S., HE, C. J., GE, X. H., GE, H. Y. & WANG, X. F. 2009. Early clinical experience using high intensity focused ultrasound for palliation of inoperable pancreatic cancer. *JOP,* 10**,** 123-9.

XU, C. & PRINCE, J. L. 1998. Generalized gradient vector flow external forces for active contours. *Signal Processing,* 71**,** 131-139.

ZHANG, L., CHEN, W. Z., LIU, Y. J., HU, X., ZHOU, K., CHEN, L., PENG, S., ZHU, H., ZOU, H. L., BAI, J. & WANG, Z. B. 2010. Feasibility of magnetic resonance imaging-guided high intensity focused ultrasound therapy for ablating uterine fibroids in patients with bowel lies anterior to uterus. *European Journal of Radiology,* 73**,** 396-403.

ZHANG, L., ZHU, H., JIN, C., ZHOU, K., LI, K., SU, H., CHEN, W., BAI, J. & WANG, Z. 2009. High-intensity focused ultrasound (HIFU): effective and safe therapy for hepatocellular carcinoma adjacent to major hepatic veins. *European Radiology,* 19**,** 437-45.

ZHOU, Y. F. 2011. High intensity focused ultrasound in clinical tumor ablation. *World J Clin Oncol,* 2**,** 8-27.

ZHU, H., ZHOU, K., ZHANG, L., JIN, C., PENG, S., YANG, W., LI, K., SU, H., CHEN, W., BAI, J., WU, F. & WANG, Z. 2009. High intensity focused ultrasound (HIFU) therapy for local treatment of hepatocellular carcinoma: Role of partial rib resection. *European Journal of Radiology,* 72**,** 160-166.

ZIMMERMANN, H., MULLER, S., GUTMANN, B., BARDENHEUER, H., MELZER, A., UMATHUM, R., NITZ, W., SEMMLER, W. & BOCK, M. 2006. Targeted-HASTE imaging with automated device tracking for MR-guided needle interventions in closed-bore MR systems. *Magn Reson Med,* 56**,** 481-8.